SAPIENZA
UNIVERSITÀ DI ROMA

Ph.D. Course in Electromagnetism and Mathematical Models for Engineering

Department of Information Engineering, Electronics and Telecommunications (DIET)

ANTENNAS EVERYWHERE

from space to undersea

DESIGN, OPTIMIZATIONS AND NEW TECHNIQUES FOR SPACEBORN, GROUND BASED AND MARINE ANTENNAS

DOCTORAL THESIS OF
FABIO PELOROSSI

TUTOR
PROF. FABRIZIO FREZZA

COURSE COORDINATOR
PROF. DANIELE ANDREUCCI

TABLE OF CONTENTS

FOREWORD I

PREFACE II

ACKNOWLEDGEMENTS IV

1. INTRODUCTION 1

1.1 ANTENNA BASICS 2

1.1.1 YAGI-UDA ANTENNAS 4

1.1.2 HORN ANTENNAS 5

1.1.3 REFLECTOR ANTENNAS 6

1.1.3.1 DUAL REFLECTOR ANTENNAS 6

1.1.3.2 BEAM WAVE GUIDE (BWG) ANTENNAS 9

1.2 ANTENNAS FIGURES OF MERIT 11

1.3 ANTENNAS FOR SPACE APPLICATIONS 13

1.3.1 COMMUNICATING WITH A SPACECRAFT 16

1.3.2 THE ESA TRACKING NETWORK 18

1.4 THE ELECTROMAGNETIC PROPAGATION THROUGH MATERIALS 19

2. SPACEBORNE ANTENNAS 22

2.1 SPACEBORNE ANTENNAS OPTIMIZATION 22

2.2 THE DRAGONIAN CONFIGURATION 22

2.3 IMAGING IN THE DRAGONIAN CONFIGURATION 23

2.4 PHASED ARRAYS 25

2.4.1 GRATING LOBES 26
2.5 A NUMERICAL METHOD FOR THE ANALYSIS OF THE DRAGONIAN CONFIGURATION 27
2.5.1 THE TEST CONFIGURATION 29
2.6 BEAM SCANNING 30
2.6.1 THE BEAM TRACKING ALGORITHM (BTA) 32
2.6.2 DETERMINATION OF THE ERRORS ON THE PREDICTED DIRECTIONS 34
2.6.3 DEPENDENCE ON M AND f/d 39
2.7 CONCLUSION 41

3. GROUND-BASED ANTENNAS FOR SPACE COMMUNICATIONS 43
3.1 THE ELECTROMAGNETIC EYES TO SPACE 43
3.2 TRACKINNG A LAUNCHER 43
3.3 ESA TT&C 15-m ANTENNAS 49
3.4 BEAM WAVE GUIDE SYSTEMS FOR THE DEEP SPACE 51
3.5 QUASI-OPTICAL DESIGN: THE GAUSSIAN BEAM APPROACH 51
3.6 OTHER OPTIMIZATION ELEMENTS 53
3.7 THE UPGRADE OF A BWG RADIO TELESCOPE IINTO A TTT&C DEEP SPACE ANTENNA 56
3.7.1 THE SARDINIA RADIO TELESCOPE 56
3.7.2 THE UPGRADE TO TT&C CAPABILITIES 58
3.7.3 SRT TT&C PROPOSED LAYOUT 59
3.7.4 THE BEAM SQUINT 61
3.7.5 BEAM SQUINT COMPENSATION 62
3.7.6 EMC, EMI AND HAZARDS 64
3.7.6.1 EMC RESULTS 67
3.7.6.2 EMI RESULTS FOR THE ELECTRONIC EQUIPMENT 71
3.7.6.3 EMI RESULTS FOR THE AIRCRAFTS AND THE BIOLOGICAL HAZARD 73

3.8 FURTHER ANALYSES TO ASSESS THE ELECTROMAGNETIC SUSTAINABILITY OF THE SITES 76
3.9 RFI 78
3.10 CONCLUSION 79

APPENDIX A: THE GAUSSIAN BEAMS 80

4. MEDIA PENETRATING ANTENNAS 87
4.1 INTRODUCTION 87
4.2 THEORETICAL BACKGROUND 87
4.3 CONDITIONS FOR THE DEEP WAVE PENETRATION 91
4.4 GENERATING INHOMOGENEOUS WAVES 95
4.5 ELECTROMAGNETIC ANALYSIS WITH THE THEORETICAL MODEL 99
4.6 THE ELECTROMAGNETIC MODEL 108
4.7 NUMERICAL PRACTICAL CASES FOR THE DEEP PENETRATION 111
4.7.1 THE ICE CAP 112
4.7.2 THE FRESH WATER 114
4.7.3 THE SEA WATER 114
4.8 CONCLUSION 117

5. CONCLUSIONS 120

PERSONAL BIBLIOGRAPHY 122

FOREWORD

Dear Reader,

This dissertation covers the most relevant and interesting topics I worked on since I joined the Doctoral School in Electromagnetics at the Department of Information Engineering, Electronics and Telecommunications (DIET) of the University La Sapienza of Rome, in 2012. In writing this thesis, I aimed at combining mathematical and theoretical formulations with more practical considerations, not omitting a philosophical point of view on the subject. I firmly believe that such three aspects shall always be present on every mankind's work. Only a good combination of them allows the author to exert positive leverage on the users.

This dissertation is intended to provide some guidelines and references to whoever wants to approach the world of the antennas and their applications. A world which is, nowadays, more and more a stronghold of our daily life and subsistence. Affirming that the humanity, at today, would be hardly able to survive one single day without using any antenna rather than, for instance, using any tongue, sounds quite strong. Nevertheless, I would bet on it.

Yours Sincerely,

Fabio Pelorossi

PREFACE

The present dissertation gathers the most significant researches and achievements of its author in the antenna domain. The text is organised in three main parts that are intended to guide the reader through a theoretical and technological excursus on antennas solutions, from space to undersea.

Each part aims at showing the answer to each of the following questions, respectively:

How a spaceborne antenna shall be?

How a ground-based antenna shall be?

How a media penetrating antenna shall be?

In the frame of a collaboration with the European Space Research and Technology Centre (ESTEC) of the European Space Agency (ESA), the author has been involved, after completing on site (in The Netherlands) his M.Sc. degree in 2011, in a research on the optimisation of the scanning properties of confocal dual reflector **antenna systems for spaceborne applications**.

As part of his permanent assignment, since 2012, as consultant at the ESA's European Space Operations Centre (ESOC), Germany, the author is responsible of different sustaining and investment projects on existing and new **ground antenna terminals for space missions**. Some of the projects are presented in this work.

Together with the group of electromagnetism of the University *La Sapienza* of Rome, the author has treated problems related to the electromagnetic deep penetration of lossy media using **deep penetrating new antenna solutions**.

The text is organized into five chapters. Chapter 1 is an introduction and deals with the historical background of modern antennas technologies and layouts and with the fundamental parameters for the analysis of antenna systems related to space and terrestrial contexts. Chapter 2 presents the major achievements of a study on a dual confocal offset antenna configuration for space applications. In particular the optical aberrations caused by the offset arrangement are analysed in order to validate the system introduced as an interesting solution for compact, light and simple payload antennas. Chapter 3 introduces to the world of ground based antennas and provides some interesting hints on a wide range of ground antenna types. Several designing solutions are proposed with the aim of optimizing the desired available gain for the various applications, from the tracking of a space launcher to the communication with spacecraft at the edge of the solar system. An in-depth study is presented on the upgrade of a radio

telescope into a ground terminal for the support of deep space missions, addressing to the required versatility of the antenna layouts and to the sustainability of the ground station environment. In Chapter 4, the possibility of achieving the electromagnetic deep penetration of lossy media is analysed. A new design solution, able to generate inhomogeneous waves, similarly to what performed by leaky wave antennas, is introduced. This layout is of extreme interest for its flexibility and for its potentiality of application, as for instance the deep penetration of seawater. Chapter 5 recaps the conclusions of the entire dissertation showing that the world of antennas is much wider than one may think at first sight and innovative solutions are always behind the corner.

All the main achievements reported in the present work have been the object of scientific publications reported in the Personal Bibliography section at the end of this volume.

ACKNOWLEDGEMNTS

I would like to thank at first my tutor, Professor Fabrizio Frezza for his guidance, support and tuition during my entire Ph.D course. A very special thank goes also to Dr. Piermario Besso of ESA/ESOC, my present boss and professional main reference. I wish to thank the colleague Vincenzo Pascale from the department DIET of La Sapienza for the work we have done together concerning the electromagnetic deep penetration and for undertaking with me so many phone conferences at challenging hours.

Since the end of 2011, all the people I met and I confronted myself with at technical and personal level, contributed to the development of the ideas reported in the present dissertation and in the achievement of its objectives. It is not necessary to list them all, but this work is dedicated to my friends, to my family and to all the people I worked and I am working with. All of them inspired me in different ways during this journey and will continue during the ones to come. I wish to thank them all for sharing knowledge, empathy, support, love.

Chapter 1

INTRODUCTION

The antenna is the last and the first part of a wireless communication system which adopts electromagnetic waves. The electromagnetic waves are, nowadays, the most common mean to make communicate two separated entities.

In 1888, Heinrich Rudolf Hertz set up standing electromagnetic waves using an oscillator, simple dipoles or loop antennas and a spark detector of his own design and made independent measurements of their wavelength and frequency. He found that their product was indeed the speed of light. He also verified that these waves behaved according to all the laws of reflection, refraction, and polarization that applied to visible light, thus demonstrating that they differ from light only in wavelength and frequency. "Certainly it is a fascinating idea," Hertz wrote, "that the processes in air that we have been investigating represent to us on a million-fold larger scale the same processes which go on in the neighbourhood of a Fresnel mirror or between the glass plates used in exhibiting Newton's rings" [1-1].

An antenna is an electric component, which allows, due to the Biot-Savart law, to irradiate or to receive electromagnetic energy, hence information, through electromagnetic waves. The Biot-Savart law is one of the most simple but fascinating phenomenon of the nature. To a variable electric current in a conductor material, corresponds an electric field which generates a magnetic field. Similarly, if a conductor material is immersed in an electro-magnetic field, a time variable electric current is induced. Therefore, an antenna offers a reciprocal behaviour as far as the transduction of an electric current to an electromagnetic field and vice versa is concerned. In general terms, any conducting material, either if immersed in an electromagnetic field or in which there is an electric current flow, can be considered as an antenna.

It was not long until the discovery of electromagnetic waves was transformed from pure physics to engineering. After learning of Hertz's experiments through a magazine article, the young Italian engineer Guglielmo Marconi constructed the first transmitter for wireless telegraphy in 1895. Within two years he used this new invention to communicate with ships at sea. By 1901, Marconi was sending information across the Atlantic. For a transmit antenna, he used several vertical metallic wires attached to the ground. Across the Atlantic Ocean, the receive antenna was a 200 meter wire held up by a kite. On the early morning of April 15, 1912, a 21-year old young telegrapher in New York City named David Sarnoff received a wireless message from the Marconi station in Newfoundland, which had picked up faint SOS distress signals from the steamship Titanic. Sarnoff relayed the report of the ship's sinking to the world. This singular event dramatized the importance of the new mean of communication. Initially, wireless communication was synonymous with telegraphy. For communication over long distances the wavelengths were greater than 200 meters. The antennas were typically dipoles formed by long wires cut to a submultiple of the wavelength. Commercial radio emerged during the 1920s and 1930s. The American Marconi Company evolved into the Radio Corporation of America (RCA) with David Sarnoff as its director. Technical developments included the invention of the triode for amplification by Lee de Forest and the perfection of AM and FM receivers through the work of Edwin Howard Armstrong and others. In his book *Empire of the Air: The Men Who Made Radio*, Tom Lewis credits de Forest, Armstrong, and Sarnoff as the three visionary pioneers most responsible for the birth of the modern communications age.

Figure 1-1: A Marconi station - credits to gettyimages

Stimulated by the invention of radar during World War II, considerable research and development in radio communication at centimetre wavelengths was conducted in the decade of the 1940s. The basic formulation of the radio transmission formula was developed by Harald T. Friis at the Bell Telephone Laboratories and published in 1946. This equation is the foundation of any Radio Frequency (RF) link. The Friis formula is very immediate and handy in dealing with any calculation related to the remote transfer of electromagnetic energy, hence information, through the use of antennas:

$$\frac{W_r}{W_t} = G_t G_r \left(\frac{\lambda}{4\pi R} \right)^2 \tag{1.1}$$

where W_r is the received power, W_t is the transmitted power, R is the distance of the radio link, λ the wavelength of the electromagnetic signal and G_r, G_t the antenna gains, in reception and transmission, respectively, which will be introduced in the next paragraph.

Let us consider (1.1) as a starting milestone for the present work.

1.1 Antenna basics

In the previous paragraph, a simple definition has been given as far as an antenna is concerned. A large variety of antenna types has been introduced during the years with the goal of optimising its function: the transduction of an electric signal to a defined electromagnetic field and vice versa. In this

paragraph some basic layouts and definition will be introduced as a basis and reference for the entire volume of the present thesis and with the aim of extending gradually the definition of what is really an antenna.

The fundamental characteristics of an antenna are its gain and its half power beam width. The gain is the measure of how much of the input electrical power is transduced into an electromagnetic field on a defined spatial direction. It is expressed with respect to a hypothetical isotropic antenna, which radiates equally in all directions. Hence, in the direction (θ,φ):

$$G(\theta,\varphi)=\frac{P_{\infty}(r,\theta,\varphi)}{W_I/4\pi r^2}=\eta_r D(\theta,\varphi) \tag{1.2}$$

where $P_{\infty}(r,\theta,\varphi)$ is the power density radiated, W_I is the power available at the input/output port of the antenna and r the distance of the observation point. η_r is defined as radiation efficiency and corresponds to the ratio of the power effectively radiated by the antenna and the power available at the input/output port of the antenna, W_I. $D(\theta,\varphi)$ is termed as directivity and describes only the directional radiative capability of an antenna with respect to an isotropic antenna, which radiates the same power in all spatial directions.

$$D(\theta,\varphi)=\frac{P_{\infty}(r,\theta,\varphi)}{P_{\infty ISO}} \tag{1.3}$$

Since electromagnetic energy propagates in the form of waves, it spreads out through space due to the phenomenon of diffraction. Individual waves combine both constructively and destructively to form a diffraction pattern that manifests itself in the main lobe and side lobes of the antenna. The antenna pattern is analogous to the "Airy rings" produced by visible light when passing through a circular aperture. These diffraction patterns, studied by Sir George Biddell Airy, consists of a central bright spot surrounded by concentric bright rings with decreasing intensity [1-2].

The Half Power Beamwidth (HPBW) is the angular separation between the points on the antenna radiation pattern, where the gain is one half of its maximum value (see Figure 1-2).

The definitions just introduced allow to conclude that, in general, the higher is the gain, i.e. the directivity, of an antenna, the smaller is the angular extension of the main lobe of its radiation pattern and consequently its HPBW.

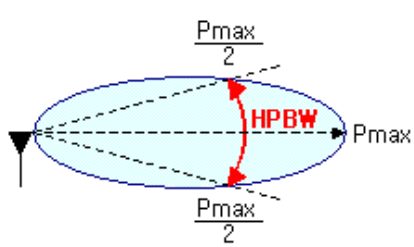

Figure 1-2: Definition of HPBW in the antenna pattern

1.1.1 Yagi-Uda antennas (1920's)

The Yagi-Uda antenna [1-3][1-4] (see Figure 1-4) consists of a distribution of metallic elements where a single element, typically a dipole, acts as a 'feed' of the structure. A dipole consists of two identical conductive elements such as metal wires or rods, which are usually bilaterally symmetrical (see Figure 1-3). A dipole is a linear antenna. It is the only element of the Yagi-Uda structure that is actually excited (a source voltage or current is applied from a transmission line). The rest of the elements are parasitic. They reflect or help to transmit (directors) the energy in a particular direction. All the elements distributed over the Yagi-Uda antenna form a linear array, although only one element is active. In fact, in general, an array is a set of two or more active antennas, distributed over a linear, 2D (see Figure 1-5) or even 3D distribution. In an array, the signals from the antennas are combined or processed in order to achieve improved performance over that of a single antenna (of any kind).

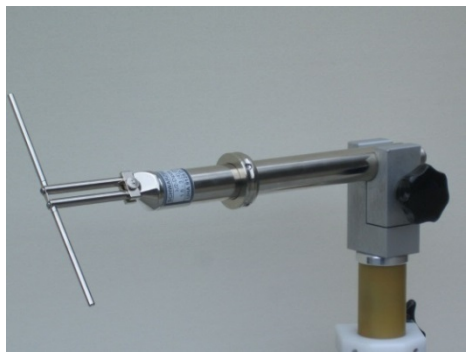

Figure 1-3: A simple dipole antenna – credits to Wikipedia

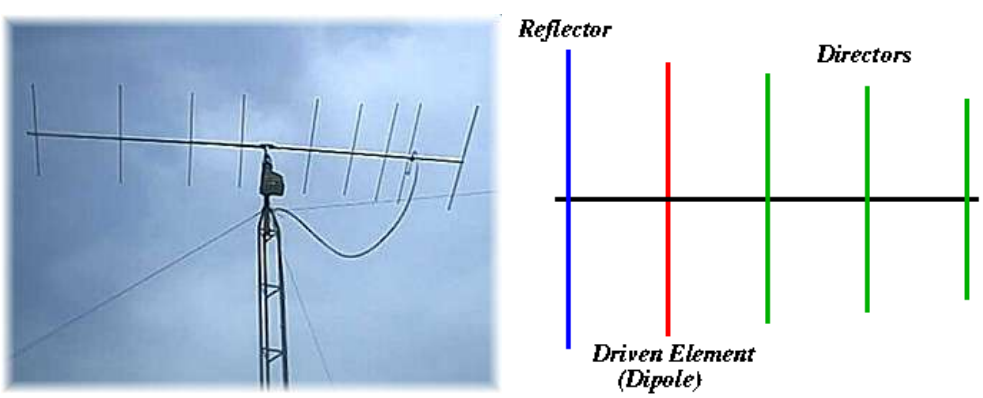

Figure 1-4: Photo (left) and schematic (right) of a Yagi-Uda antenna – credits to www.antenna-theory.com

Figure 1-5: A 2D array distribution of antenna elements: the SKA (Square Kilometre Array) – credit to SKA telescope

1.1.2 Horn antennas (late 1930's)

A horn antenna is an aperture antenna. A horn antenna is a flaring metal waveguide shaped like a horn to direct radio waves in a reduced spatial region (see Figure 1-6). Therefore, a horn antenna presents, in general, higher directivity, i.e. higher gain, compared to a linear antenna. The aperture's shape determines its antenna pattern. The waveguide itself can be fed with a short dipole. A waveguide is simply a hollow, metal cavity.

Waveguides are used to guide electromagnetic energy from one place to another and are preferred to RF coaxial cables if the handling of high power is desired. This is because the inner portion in the waveguide is filled with air as dielectric and the air has a breakdown voltage of 30 KV/cm, much higher than the dielectrics which fill the coaxial cables. Furthermore, since a waveguide is air filled, it presents less losses compared to a coaxial line. In a waveguide, no power is lost through radiation and even the dielectric loss is negligible. On the other hand, as the outer wall of the waveguide is metallic, it is bulky, heavy and expensive also, while coaxial lines are smaller in size and lighter. Hence coaxial is in use for many other relatively low power microwave applications.

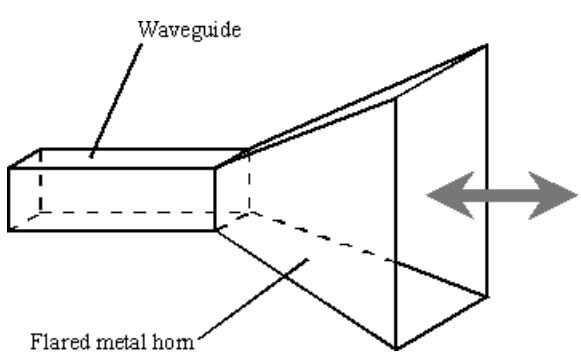

Figure 1-6: Schematic of a horn antenna

1.1.3 Reflector antennas (late 1940's)

Reflector antennas are typically used when a very high gain (e.g. satellite transmission or reception) or a very narrow main beam (e.g. secure communications) are required. Gain is improved and the main beam narrowed with the increase in the reflector size. A reflector employs a curved surface, usually with the cross-sectional shape of a paraboloid of revolution, to direct the radio waves. Horn antennas are usually used to feed the reflector antennas. One or multiple reflectors can be used. The gain of a reflector antenna and therefore the pattern are defined primarily by the size of the last reflector, i.e. the reflector which radiates in the free space, also referred to as main reflector. Secondarily, the pattern is determined by the reflectors layout (if many reflectors are present) and by the electromagnetic field distribution on the reflectors. The variation of the electromagnetic field distributed all-over a reflector rim is called taper.

1.1.3.1 Dual reflector antennas

The most widely used multiple reflector antennas are characterized by a paraboloidal main dish and a smaller secondary reflector, which can be either convex or concave, respectively in the so-called *Cassegrain* and *Gregorian* configurations. The secondary reflector is known as sub-reflector and it manages to turn the relatively narrow-angle electromagnetic beam of the feed into a much larger angle subtended by the paraboloidal reflector. The feed is positioned in the focal point of the sub reflector, whose second focus is coincident with the one of the main dish: this is made to ensure that the radiation previously generated by the feed and then reflected by the sub-reflector is focused to infinity as if it would be originated from the focal point of the main reflector.

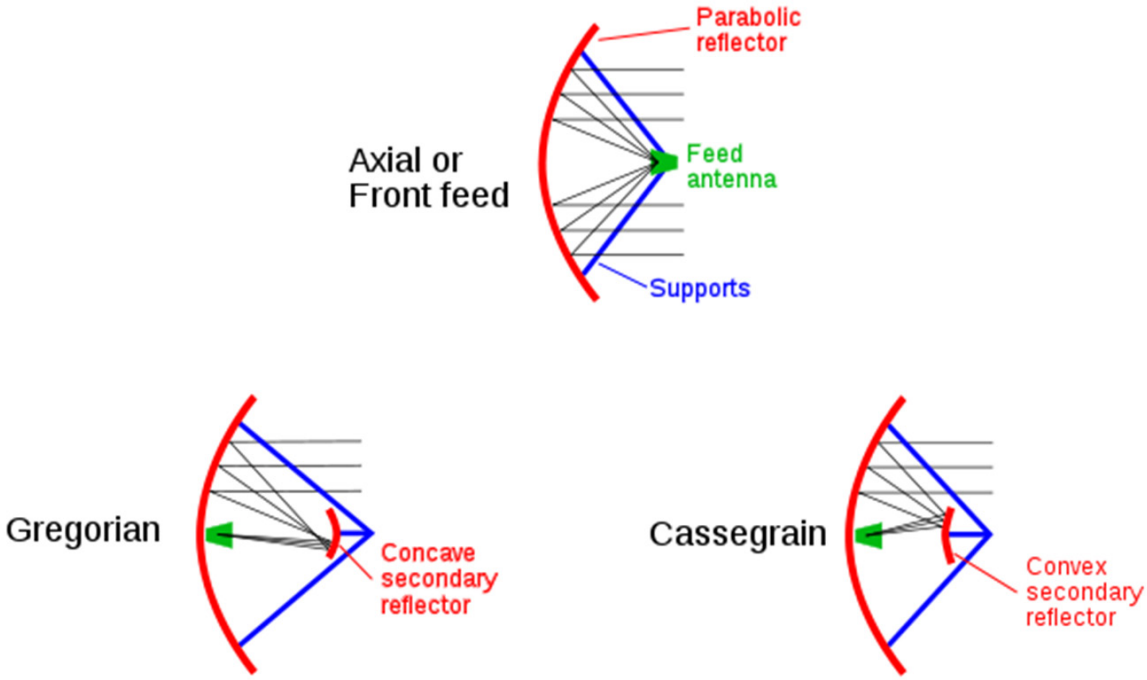

Figure 1-7: Single reflector antenna (top) vs. dual reflector Cassegrain and Gregorian (bottom) configurations – credits to Wikipedia

Figure 1-7 shows the optical layout of classical Cassegrain and Gregorian antennas (at the bottom) compared to a single reflector antenna (at the top), where the feed is placed in the focus of the parabolic reflector. In the Cassegrain and Gregorian configurations [1-5], all reflectors are conic sections, but, whereas the main reflector presents an eccentricity equal to one in both cases (i.e. it is a paraboloid), the sub-reflector has, respectively, an eccentricity greater than one (hyperboloid) in the Cassegrain configuration, and smaller than one (ellipsoid) in the Gregorian configuration. In both cases, one of the sub-reflector foci is placed at the main reflector focal point, and the feed is placed in the second sub-reflector focal point. The images represent the electromagnetic radiation through rays using the so-called Geometrical Optics (GO) approximation. Before considering more esoteric multiple-reflector antennas, the advantages and disadvantages of dual reflectors over single reflector antennas are shown. So that any advantage provided by other types of multiple reflector antennas will be result more straightforward.

The advantages include:

- The possibility of reshaping the feed pattern by means of the sub-reflector in addition to the main reflector;
- A more convenient feed location with shorter feed line;
- Having a larger depth of the focus, which improves the optical performances;
- The fact that most of the electromagnetic noise is coming from the cold sky rather than from ground;
- A more compact structure.

The disadvantages include:

- A greater blockage, caused by the sub-reflector, which produces higher side-lobes;
- A need for the feed to be more directive, since it has to illuminate a smaller angular portion, corresponding to the sub-reflector;
- Less stable performances over a broad band;
- Tighter reflectors accuracy requirements are needed not to spoil the performances.

In classical dual reflectors antennas, the sub-reflector has, in fact, the effect of magnifying the feed radiation pattern and the dual reflector system is, as a first approximation, equivalent to a single reflector paraboloidal antenna with a greater focal length, f_{eq}. f_{eq} is related to the focal length of the dual reflector main dish, f, by the magnification factor, M, defined, referring to Figure 1-8, as:

$$M = \frac{f_{eq}}{f} = \frac{\tan(\vartheta')}{\tan(\vartheta)} = \left|\frac{e+1}{e-1}\right| \tag{1.4}$$

where e is the eccentricity of the sub-reflector. In other words, an ideal (not shaped) sub-reflector in classical dual reflector system does not modify the shape of the feed radiation pattern, but it just scales it. Typical values of M are from 4 to 10 for antennas with focal length to diameter ratio (f/d) in the range of 0.25-0.50. The resulting illumination function of the main reflector is therefore (as a first approximation) exactly the same as that of the equivalent paraboloid illuminated by the same feed. An optimal balance between the antithetic reflectors illumination and spill-over efficiencies may be achieved by properly modifying the feed radiation pattern. This may be reached either by increasing the degree of complexity of the feed system, or by shaping the dual reflector system.

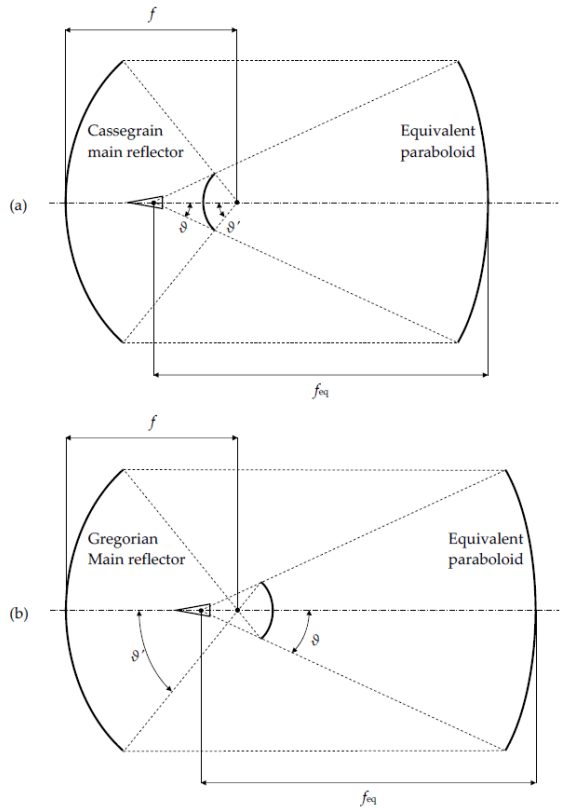

Figure 1-8: Equivalent paraboloid of a Cassegrain (a) and Gregorian (b) dual reflector system

Since the first solution is in most cases unpractical or unfeasible, the second one is commonly adopted and it has become over the years the preferred approach for designing dual reflector antennas, when high performance is needed. Furthermore, a tighter accuracy requirement is needed to keep all path lengths equal. In fact, considering a pure Geometrical Optics approximation, any geometrical imperfection of the system is translated into a non-ideal electromagnetic behaviour. Geometrical Optics, or ray optics, describes the electromagnetic propagation in a homogeneous medium in terms of rectilinear rays, which bend at the interface of dissimilar media, are absorbed and reflected according to the laws of optics and do not take into account effects such the diffraction and the interference. This simplification is useful in practice and results as an excellent approximation when the wavelength is much smaller compared to the size of the structure with which the electromagnetic radiation interacts. With the GO approximation in mind, it is useful to recall the fundamental properties of the conic sections used in the Cassegrain and Gregorian configurations:

- In a parabola, all rays which run parallel to the parabola's axis and hit the parabola will be reflected directly to the unique focus;
- In an ellipse, a ray originating from one focus always reflects off the ellipse's and passes through the other focus;
- In a hyperbole, if a ray emerges from one focus and is reflected from either branch of the hyperbola, the ray appears to have come from the other focus.

Paramount is the property of the parabola (for this reason used always as a main reflector): the parabola is able to convert a plane wave into a spherical wave centred in one point (the focus) and vice versa.
The GO technique is particularly useful in describing geometrical aspects of imaging, including aberrations, as it will be discussed in Chapter 2. Aberrations are generated in case of geometrical

imperfections or of asymmetric configurations. Considering a pure Cassegrain or Gregorian configuration, which are both symmetrical, aberrations can be caused only by a wrong optical arrangement (refer to Figure 1-8) or by a poor polishing of the antenna reflectors. The accuracy required for the reflector surface of a prime focus single reflector antenna is a small fraction of a wavelength, typically 1/10λ or 1/16λ. Jensen shows in [1-6] a curve with 1 dB loss for an Root Mean Square (RMS) tolerance of 1/25λ, or just over 1 mm at 10 GHz. The defined accuracy shall be not exceeded otherwise the pattern generated by the feed would be distorted (or aberrated) in the magnification by the antenna reflectors.

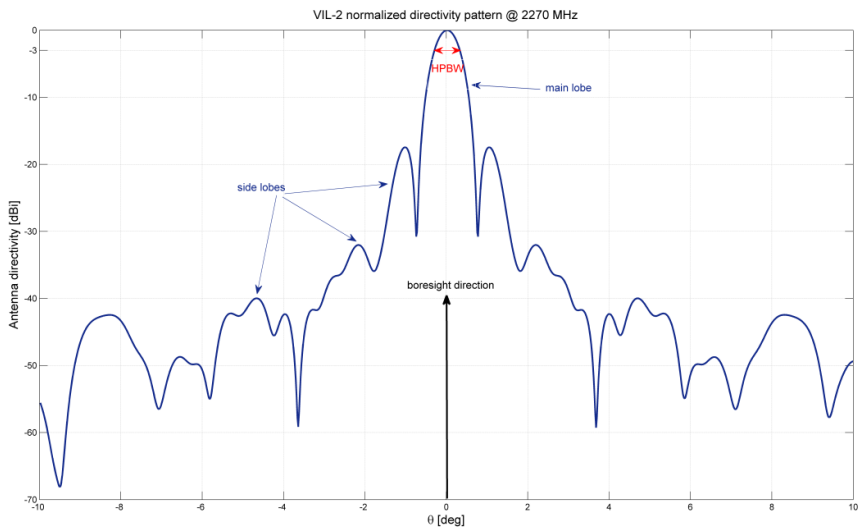

Figure 1-9 Simulated pattern of an ESA 15-m ground station antenna in a Cassegrain configuration

An interesting dissertation on the historical background of dual reflector antennas may be found also in [1-7] [1-8] [1-9].
Figure 1-9 shows the simulation of a typical Cassegrain antenna pattern considering main reflector's shaping, together with blockage and spill-over effects.
It is defined as spill-over the portion of electromagnetic energy which is lost in the reflection(s) with the reflector(s) system.

1.1.3.2 Beam Wave Guide (BWG) antennas

A Beam Waveguide (BWG) system [1-11] is a combination of reflectors used to move the focal position of a dual reflector antenna from the center of the main reflector to a different, more suitable location, preferably closer to the ground. Furthermore, with a BWG system, it is possible to increase the number of focal positions and to create multiple paths by means of rotating and/or dichroic mirrors. BWG are composed of a number of flat and curved relatively small reflectors, which convey microwave beams from the large dual reflector system to the feeds and vice versa. This permits to the feeds to be mounted at the most convenient locations and positions. The BWG also allows for decoupling the feeds from the movements of the antenna, and for easing their maintenance and operation. The degradation of the overall antenna efficiency caused by the BWG system can be deemed in general negligible if one considers that the several mirrors in a

BWG system gives more degrees of freedom in the optical design in order to achieve a minimization of the degradation of the illumination efficiency and of the spill-over losses. Figure 1-10 depicts an example of BWG basic layout. A Cassegrain configuration can be noted, where in the Cassegranian focus, in place of the feed, the *pseudo*-focus of a flat mirror is located. Two feeding capabilities can be made available in such example configuration by the use of a dichroic mirror (M4). More capabilities can be added extending the BWG downwards by means of further mirrors and Frequency Selective Surfaces (FSS). BWG configurations will be further explored in Chapter 3.

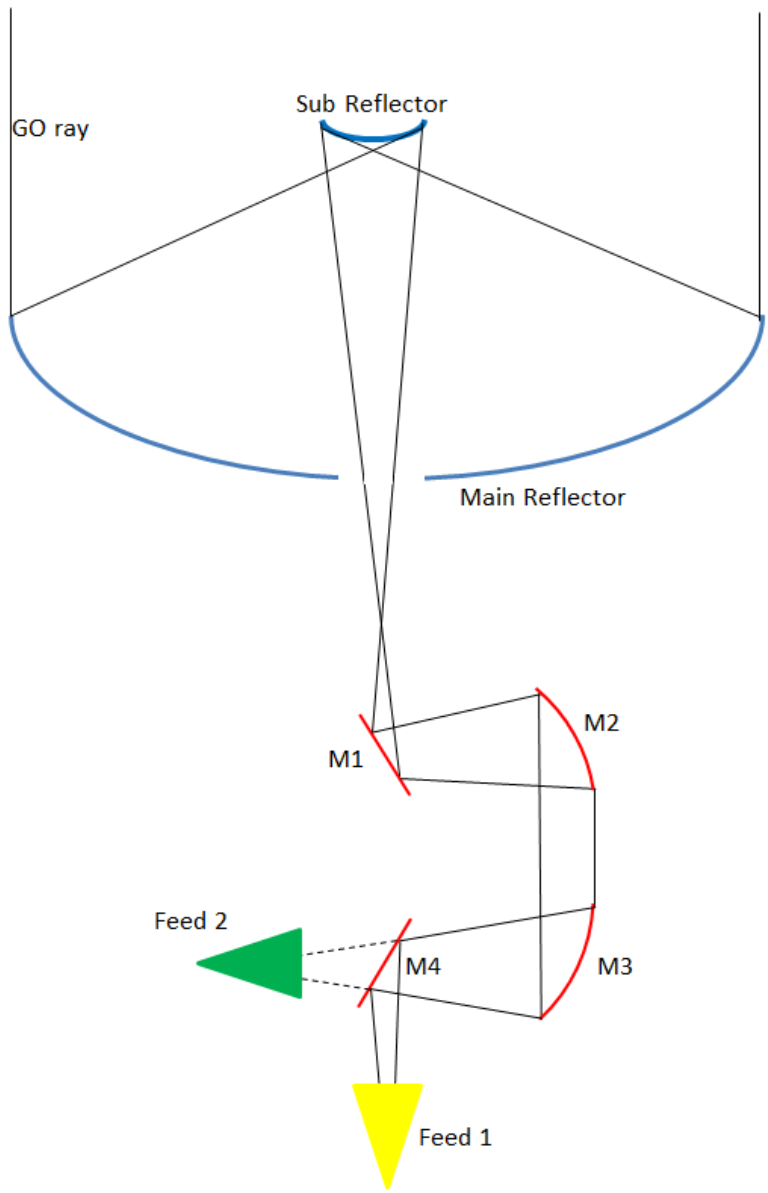

Figure 1-10: A typical BWG basic layout

1.2 Antennas figures of merit

In evaluating the quality of the performance of an antenna purely from a RF point of view, the two crucial parameters which have to be considered are the ratio of the antenna gain to its noise system temperature (G/T_{sys}) and the Equivalent Isotropic Radiated Power (EIRP), which is given by the product of the antenna gain by its transmitted power. Both factors may be improved by increasing the gain of the antenna, which is proportional to size and frequency. They represent the markers of the antenna quality in reception and transmission, respectively.

The system temperature is a measure of the total noise power and includes contributions from the environment, the antenna itself and the receiver system. The first two contributes are accounted in the antenna noise temperature (measured in Kelvin) defined at first instance as:

$$T_A = \frac{1}{4\pi}\int_0^{2\pi}\int_0^{\pi} T_B(\theta,\varphi)D(\theta,\varphi)\sin\theta d\theta d\varphi \tag{1.5}$$

where T_B is the brightness temperature (in Kelvin).

For an antenna with radiation efficiency η_r (see 1.2), the antenna noise temperature has to be corrected to:

$T'_A = \eta_r T_A + T_0(1-\eta_r)$ with T_0 290 K.

It is important to calculate the system temperature at the same reference point. Based on this, the losses introduced by the transmission line (e.g. waveguide, coaxial cable) shall be accounted in determining the final expression of the antenna noise temperature:

$$T''_A = T'_A e^{-2\alpha_L L} + T_0(1-e^{-2\alpha_L L}) \tag{1.6}$$

The third contribute, the receiver noise temperature is evaluated as follows:

$$T_{REC} = (F-1)T_0 \tag{1.7}$$

where F is the system noise figure equal to:

$$F = F_1 + (F_2-1)A_1 + \frac{(F_3-1)}{A_1 A_2} + \ldots + \frac{(F_N-1)}{A_1 A_2 \ldots A_{N-1}} \tag{1.8}$$

and A_n represents the gain (negative if a loss) of the n-th component of the receiver chain starting from the reference point, which is, as by definition, in front of the low noise amplifier (LNA).

T_{sys} is obtained as:

$$T_{sys} = T''_A + T_{REC} \tag{1.9}$$

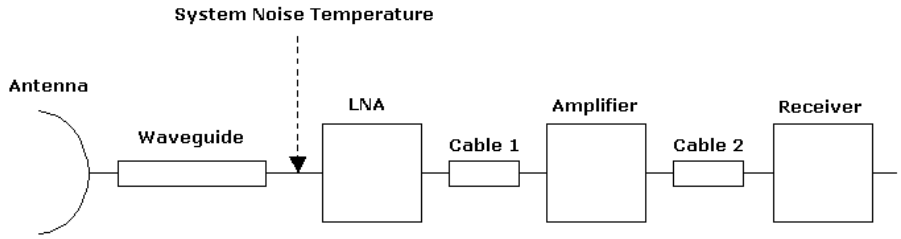

Figure 1-11: Scheme for the calculation of the system noise temperature in a receiving system

The gain, expressed in (1.2) can be also determined in the boresight direction for an axis symmetric reflector antenna by:

$$G = \eta(\frac{4\pi}{\lambda^2})A \tag{1.10}$$

where A is the main aperture's area.

This equation determines the required antenna area for the specified gain at a given wavelength.
The net efficiency η is the product of the aperture taper efficiency η_a, which depends on the electric field distribution over the antenna aperture, and the total radiation efficiency η_r associated with various losses. These losses include for a reflector antenna spill-over, ohmic losses, heating losses, phase non-uniformity, blockage, surface roughness losses (see aberrations) and cross polarization. For a typical antenna, η = 0.55. Within the main lobe of an axis symmetric antenna the gain in a direction θ with respect to the boresight direction may be approximated (in dB) by:

$$G(\theta) = G(0) - 12(\frac{\theta}{HPBW})^2 \tag{1.11}$$

Where G(0) is the boresight gain. This formula makes explicit once again that the main radiative characteristics of the antenna are mainly defined by the HPBW, hence by its physical dimension. Furthermore, the gain of the side-lobes can be approximated by an envelope. For instance, for big ground stations antennas (D/λ>100) the side-lobes must fall within the envelope 29-25logθ, defined by the International Telecommunication Union (ITU). This envelope being determined by the requirement of minimizing interference between neighbouring satellites.

The equivalent isotropic radiated power (EIRP) is the power radiated equally in all directions that would produce a power flux density equivalent to the power flux density of the actual antenna. Therefore, one obtains that the EIRP is the product of the antenna gain and the power applied to the input terminals of the antenna. The efficiency is absorbed here in the definition of the gain.

1.3 Antennas for space applications

While radar applications have been the main driver for innovation and new developments in the field of antennas in the post-war decennia, space communications, navigation and remote sensing requirements, have stimulated many significant advances in several areas of modern antenna theory and implementation. Technologies have to be developed to cope with every day more demanding requirements. Beyond the technological solutions devoted to the particular application, common and paramount drivers of a space system design are the facts that the spacecraft has to communicate with Earth and:

- The spacecraft shall consume less power as permissible
- The spacecraft shall be as light, small and simple as permissible

These constraints apply to any spacecraft sub-system, constituting its payload. In spacecraft terminology, any sub-system able at accomplishing a functional task which allows the mission to retrieve measurements from any external target or related to the spacecraft itself is considered a payload. In this context, the antenna sub-system is one of the essential spacecraft's payload.

The extremely finite resources available in space limit considerably the power usable by a spacecraft. Furthermore, the difficulties and consequent high costs related to the launch of a spacecraft, require for very limited weight and encumbrance. Besides, the spacecraft shall be as simple as possible to increase its reliability. All these aspects are addressed on Chapter 2 of the present dissertation.

On the other hand, the communication from and to very far deep space probes, may require for an extremely high available gain. In fact, according to the Friis formula (1.1), the attenuation of a space link is directly proportional to the square of the distance of the two antennas. Extremely high losses (up to 300 dB for missions exploring the outer solar system) have to be compensated by the gain provided by the antennas. The on-board antenna is very limited in power; only a very low power signal (generally some Watts) can be transmitted. Similarly, the on-board antenna, the so-called payload antenna, is limited in size. Consequently, most of the gain available for the space link shall be given by the ground antenna terminal and this is accomplished with very large dishes (up to 70-m of diameter). Referring to the figures of merit introduced previously, the achievement of high EIRP and G/T is a requirement entirely to be reached by the ground terminal (also referred as ground station), alike any data processing capability required by the mission. The required EIRP is achieved both by exploiting large dishes and by the use of very high power amplifiers (HPAs). The requirement on the G/T is fulfilled by using very large dishes and by the employment of very low noise cryo-cooled amplifier (LNAs), while the amplifiers mounted on the spacecraft remain non-cooled, simple devices. Typical numbers of the dimensioning of a space link are reported in Table 1-1 as far as both the space side and the ground side are concerned.

Table 1-1: Space and ground – two totally different environments

PROPERTY	SPACECRAFT	GROUND STATION
Transmit power	A few Watts to tens of Watts	Up to hundreds of kilowatts
Antenna diameter	A few cm to 3 meters	Up to 70- meters
Processing power	50-200 MIPS	Practically unlimited
Receiver temperature	290 K	Tens of K

Once again, from the Friis equation, we can notice that the Free Space Loss, quantified as $\left(\frac{4\pi R}{\lambda}\right)^2$ and identified as FSL, is proportional to the frequency of operation (the wavelength λ is inversely proportional to the frequency). Similarly the power spreads according to the square of the distance. At the same time, from equation 1.10, the antenna gain results proportional to the square of the frequency.
The frequency chosen for the radio-link and the distance of the spacecraft from Earth are therefore the main driving parameters in the determination of the dimensioning of the antennas (both on board and at ground).
The frequencies allocated to space missions are decided by the International Telecommunications Union (ITU), which is the global body that assigns any radio frequency allocation.

Not all of the electromagnetic spectrum can pass through the Earth's atmosphere. There are in fact only two main windows of the electromagnetic spectrum that are open to space. One is the visible spectrum and the other is the radio spectrum. However, not all of the radio spectrum is useable for space communication. As suggested by Figure 1-12 the radio spectrum free from atmospheric attenuation lies between 30 MHz and 10 GHz (from 10 m to 3 cm of corresponding wavelength). Figure 1-12 reports the atmospheric opacity, which translates directly to attenuation of the signal. At around 30 GHz (1 cm of wavelength) a peak of the attenuation is given by the waters molecules. For slightly shorter wavelengths, the attenuation decreases rapidly before encountering the attenuation peak given by the oxygen (0.5 cm of wavelength). This band, corresponding to the category Ka-band of the IEEE standard is currently used for communicating form Earth with some deep space missions, where “deep space” defines the regions beyond the gravitational influence of the Earth encompassing interplanetary, interstellar and galactic space. Together with the Ka-band, the most common bands used nowadays for space communications are the S-band and X-band. Table 1-2 summarises the IEEE standard for the radio frequency spectrum allocation up to millimetre wavelengths. For smaller wavelengths (higher frequencies) the atmosphere shall be considered completely opaque until reaching optical frequencies. From the ITU website, an interesting historical excursus can be found as far as the frequency usage in space is concerned.

The optical space communications will be the new frontier of research in space technologies, already started in 2014, when the north American National Aeronautics and Space Administration (NASA) flew the Lunar Laser Communication demonstration (LLCD) on the Lunar Atmosphere and Dust Environment Explorer (LADEE) spacecraft. This was the first practical demonstration of optical communication from deep space. It achieved up to 622 Mbps downlink data rate over 400000 km [1-10], resulting on an improvement of a factor of 100 with respect to the modern systems (considered to work in X-band).

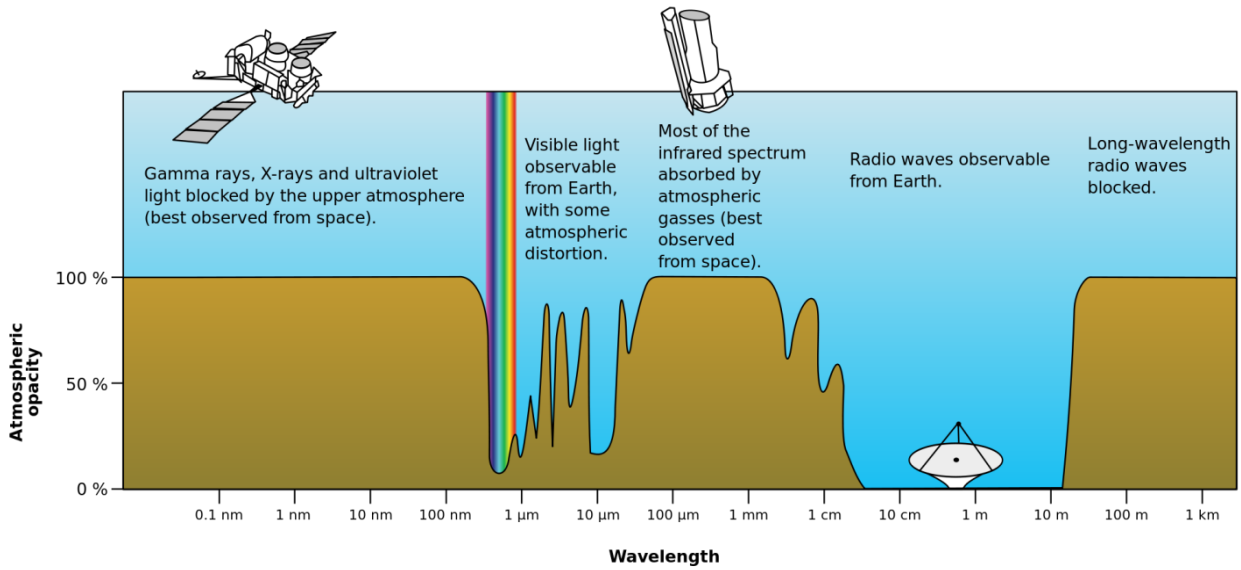

Figure 1-12 – Atmospheric opacity of the radio spectrum - credits to Wikipedia

Table 1-2: Microwave spectrum band IEEE standard definitions

500-1000 MHz	**P**
1-2 GHz	**L**
2-3 GHz	**S**
3-4 GHz	**S**
4-6 GHz	**C**
6-8 GHz	**C**
8-10 GHz	**X**
10-12.4 GHz	**X**
12.4-18 GHz	**Ku**
18-20 GHz	**K**
20-26.5 GHz	**K**
26.5-40 GHz	**Ka**
40-90 GHz	**W**

Figure 1-13: The Pioneer Deep Space Station erection at Goldstone (1958) - credits to NASA JPL

The first ever built ground terminal was a 26-m L-band (960 MHz) antenna, erected by the Jet Propulsion Laboratory (JPL) in 1958 to communicate with the spacecraft Pioneers 3 and 4. The antenna site was subsequently named the Pioneer Deep Space Station DSN-11 in Goldstone [1-11]. It began operation with a focal-point feed system but was quickly converted to a Cassegrain configuration, which remained until the antenna was decommissioned in 1981. In 1985, the U.S. National Park Service declared the site a national historic landmark.

1.3.1 Communicating with a spacecraft

So far, the text has been generally referring to the communication of the spacecraft from and to Earth. This dissertation will not cover thematic as the space navigation or remote sensing. Nevertheless, some more text shall be spent to better define what *communicate* means from and to a spacecraft. In this context, the functions that shall be covered by the communication Earth-spacecraft are enumerated hereafter:

- Receive information about the spacecraft position and all subsystems status and the observable data, objective of the mission, in other words on its telemetry.
- Track the spacecraft to assure continuous contact.
- Transmit commands to the spacecraft to control its attitude and functions.

A ground station, which is able to support such tasks is termed as a TT&C station (Telemetry, Track and Command). The Pioneer Deep Space Station DSN-11 in Goldstone was the first TT&C station. TT&C stations may be quite simple or rather complicate, depending on the space mission characteristics, which

are driven by the final observable data. The characteristics of a space mission are translated into several requirements. Paramount is the orbit to be followed by the spacecraft. In fact, the orbit defines the distance of the spacecraft and therefore the required gain to be fulfilled in the link budget Earth-space (see again the Friis formula). Furthermore, having introduced the concept of tracking the spacecraft, it is straightforward to translate the requirement on the orbit to the required movable capabilities of the ground station antenna (speed, acceleration and travel ranges).

The most canonical orbits, can be classified as:

- The Low Earth orbit (LEO): up to 2000 km commonly used by Telecommunications and Earth Observation satellites and by the ISS. Particular orbits exist within this region like the High Elliptical orbit.

- The Medium Earth orbit (MEO): from 2000 km to just below the geosynchronous orbit at 35786 km; used by navigation, communication, and geodetic/space environment science satellites.

- The geostationary orbit, geostationary Earth orbit or geosynchronous equatorial orbit (GEO) is a circular orbit 35786 km above the Earth's equator and following the direction of the Earth's rotation. Particular orbits exist within this region like the High Earth orbit.

As satellites in MEO and LEO orbit the Earth faster, they do not remain visible in the sky to a fixed point on Earth continually like a geostationary satellite, but appear to a ground observer to cross the sky and "set" when they go behind the Earth. Therefore, to provide continuous communications capability with these lower orbits requires a larger number of ground terminals, so one will always be in the sky for transmission of communication signals.

Some other interesting orbits lie around the so-called Lagrangian points. Lagrangian points correspond to positions in an orbital configuration of two large bodies where a small object affected only by gravity can maintain a stable position relative to the two large bodies. The Lagrange points mark positions where the combined gravitational pull of the two large masses provides precisely the centripetal force required to orbit with them. There are five such points referred to the Earth-Sun system, labelled L1 to L5, all in the orbital plane of the two large bodies (the Earth and the Sun). The first three are on the line connecting the two large bodies and the last two, L4 and L5, each form an equilateral triangle with the two large bodies. The two latter points are stable, which implies that objects can orbit around them in a rotating coordinate system tied to the two large bodies.

Sun–Earth L1 is suited for making observations of the Sun–Earth system. Objects here are never shadowed by Earth or the Moon. The first mission of this type was the International Sun Earth Explorer 3 (ISEE-3) used as an interplanetary early warning storm monitor for solar disturbances. The LISA Pathfinder (LPF) satellite was launched on 3 December 2015 and arrived at L1 on 22 January 2016, where, among other experiments, it will test the technology needed by the forthcoming satellite LISA to detect gravitational waves.

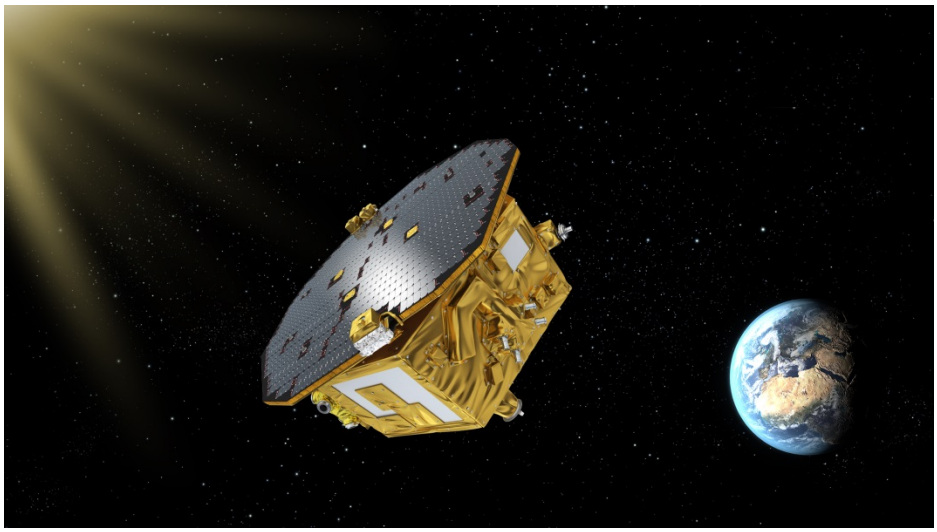

Figure 1-14: The LISA pathfinder satellite at point L1 – credits to ESA

LPF was tracked by a new ESA developed ground station at Malindi (Kenya), a 2-m terminal located close to the equator and especially designed to follow the complicate phases of the LEOP planned for such spacecraft.

LEOP is the acronym for Launch and Early Orbital Phases of a spacecraft. The launch phase begins 10 hours before launch and ends as the satellite separates from its launch vehicle. In this phase, the primarily track is performed on the launcher rather than on the satellite itself. After separation between the satellite and the launcher and before the satellite goes into its final orbit, several critical manoeuvre have to be accomplished before its on-board computer initiates an acquisition sequence of automatic operations, pointing the payload instruments to the Earth and preparing the spacecraft for the final orbit. Chapter 3 provides some more hints on the track of space launchers from ground.

1.3.2 The ESA tracking network

The ESA tracking station network (ESTRACK) is a worldwide system of TT&C ground stations providing links between a wide range of space missions in orbit and the European Space Operations Centre (ESOC). ESTRACK stations provide also tracking and first signal acquisition of the missions during the LEOP. Each ESTRACK station site hosts one or more terminals, each comprising an antenna and its associated signal processing equipment.

The core of the ESTRACK network is composed at present by eleven stations in seven countries, each consisting of one terminal (the antenna and all associated signal processing equipment) and its associated site infrastructure (a plot of land). In addition to ESTRACK's core, an Augmented Network and a Cooperative Network define a global Network (Figure 1-15) which gives to ESA the possibility to have access to a very wide number of terminals, during a short duration LEOP or other critical mission phases.
ESTRACK is constituted of a variety of ground antennas, from 2- to 35-metre of diameter.
The ESTRACK antennas operate in the ITU S-, X- and Ka-bands allocated to the space science services (Space Operation, Space Research, Earth Exploration-Satellite Services).
The ESTRACK Core Network typically provides over 45000 hours of tracking support each year, with a performance of 99% availability rate.

Figure 1-15: ESA ESTRACK core, cooperative and augmented network – credits to ESA

1.4 The electromagnetic propagation through materials

All materials contain ions and electrons. These charged particles experience Lorentz force when exposed to electromagnetic fields. Except in plasmas (ionized gases), currents are predominantly caused by electrons motion because ions are practically immobile. In common materials which are neither perfect conductors nor perfect dielectric, the superficial small currents induced by the external electromagnetic field tends to prevent the external field from penetrating into the material itself. This phenomenon is known as skin effect. Several modern application of remote sensing and telecommunication require nevertheless the capacity of overcoming such boundary, achieving the so called deep penetration. We may think for instance to non-invasive medical techniques for the characterisation of the human skin [1-13], as well as to the remote sensing of buried objects or to the communication through sea water [1-14]. All these disciplines have to face the limit stated by the skin effect which defines an exponential law for the attenuation of the electromagnetic field travelling through the lossy material. How rapidly such field is attenuated is determined by the material itself and the frequency of operation. Considering a defined material for the application in subject, one may vary only the frequency of operation, bearing in mind that lower frequencies are affected by lower attenuation. The latter represents a further limitation towards the realisation of a doable and efficient deep penetrating electromagnetic system. Nevertheless, this analysis is partially flawed. The expression for the skin depth usually given refers to penetration of the conducting medium by a homogenous plane wave. Homogeneous plane waves are the travelling planar fields which are the usual result of distance sources. However, an arbitrary wave field may contain a spectrum of inhomogeneous waves. Thus the penetrating properties of an electromagnetic field in a lossy material cannot be judged only on the basis of the skin depth for homogeneous waves. The penetrating properties of inhomogeneous waves may be quite different and must be included. Inhomogeneous waves are

represented by a variety of wave and field types, such as surface waves and antenna near fields. Typically, they are bound, though often loosely, to an interface or antenna structure. A significant property of surface wave types is that unlike ordinary plane waves, the penetration depths of these waves into a lossy material is not solely determined by the properties of the material itself (on top of the frequency of operation) but also depends upon the parameters of the medium in which the wave is launched. The employment of inhomogeneous waves is exploited in this dissertation to pave the floor for the project of a new generation of deep penetrating actuators. The enhancement of the penetrating capabilities of such systems allows, in the first place, to use higher frequencies of operation, thus avoid the employment of huge antenna systems [1-15] (see also Figure 1-16) and making available larger bandwidth for the data transmission, extending in this way the possible range of use to numerous applications.

Figure 1-16: Cumbersome ELF and VLF antennas on a submarine – credits to naval-technology.com

References

[1-1] Radio-craft, Vol. I, No. 8, Hugo Gernsback editor, Feb. 1930.

[1-2] George Biddell Airy, On the Diffraction of an Object-glass with Circular Aperture, in *Transactions of the Cambridge Philosophical Society*, vol. 5, pp. 283-291, 1835.

[1-3] H .Yagi, Beam transmission of ultra-shortwaves, Proceedings of the IRE, vol. 16, pp. 715–740, June 1928.

[1-4] S. Uda, High angle radiation of short electric waves. Proceedings of the IRE, vol. 15, pp. 377–385, May 1927.

[1-5] P. W. Hannon, Microwave Antennas Derived from the Cassegrain Telescope, IRE Transactions on Antennas and Propagation, pp. 140-153, March 1961.

[1-6] P.A. Jensen, Cassegrain Systems, in A.W. Rudge, K. Milne, A.D. Olver, P. Knight (editors), The handbook of Antenna Design, Peter Peregrinus, pp. 162-183, 1986.

[1-7] V. Galindo, Synthesis of Dual Reflector Antennas, Electronics Research Laboratory Report 62-22, University of Califonia, Berkeley, July 30, 1964.

[1-8] W. F. Williams, High Efficiency Antenna Reflector, Microwave Journal, Vol. 8, pp. 79-82, July 1965.

[1-9] C. J. Sletten, Reflector and Lens Antennas: Analysis and Design Using Personal Computers, Artech House, INC., pp. 138-141, 1988.

[1-10] L.J.Deutsch, S.A.Townes, P.E.Liebrecht, P.A.Vrotos, D.M.Cornwell, Deep Space Network: The Next 50 Years, SpaceOps Conference, 16-20 May 2016, Daejeon, Korea.

[1-11] W.A.Imbriale, Large Antennas of the Deep Space Network, Monograph 4, Deep-Space Communications and Navigation Series, JPL Publication 02, February 2002. Available online at descanso.jpl.nasa.gov/Monograph/series4/Mono4_Title-FM.pdf and published by John Wiley & Sons, 2003.

[1-12] T.Kitsuregawa, "Advanced Technology in Satellite Communication Antennas: Electrical & Mechanical Design", Artech House, INC., 1990.

[1-13] L.S.Taylor, "Penetrating Electromagnetic Wave Applicators", IEEE Transactions on antenna and propagation, Vol. AP-32, No. 10, October 1984.

[1-14] A. Al-Shammaá, A. Shaw, S.Saman, "Propagation of Electromagnetic Waves at MHz frequencies through seawater, IEEE Transactions on antennas and propagation, Vol.52, No.11, November 2004.

[1-15] D.F.Rivera, R.Bansal, "Towed antennas for US submarine communications: A Historical perspective", IEEE Antennas and Propagation Magazine, Vol.46, No.1, February 2004.

Chapter 2

SPACEBORNE ANTENNAS

How a spaceborne antenna shall be?

A spaceborne antenna shall be as light, simple and small as permissible by its application.

2.1 Spaceborne antennas optimization

Last generation satellite payload systems for telecommunications and Earth observation require the capability to scan over a wide range with a narrow beam. Space missions use more often large aperture phased planar arrays in satellite antennas to perform electronic beam scanning. Nevertheless, the use of very large arrays has drawbacks, because of their weight, the losses and the complexity of the long interconnections required to cover the entire planar array area. Smaller arrays would lead to lower costs, a lesser total weight of the payload and would give the possibility to simplify the deployment system. On the other hand, reducing the radiating area of an array increases the width of the pencil beam, leading to less accuracy in the spatial resolution of the so-called footprint at Earth. The use of metallic reflectors, combined with smaller planar arrays, is a very convenient compromise, commonly used in the spaceborne antenna payload technologies. An array with limited extension, together with a reflector system, is able to approximate the performance of a large array with an aperture equal to the main reflector one. The system can be termed as an imaging hybrid antenna. It combines the features of an imaging system constituted by metallic reflectors (i.e. focalization properties, low cost, large frequency bandwidth) and of array antennas (i.e. electronic pointing and reconfigurability). While the equivalent large array antenna exhibits better irradiative performances, the imaging hybrid antenna system is usually significantly simpler and lighter and for these reasons it may be adopted especially when large antenna apertures and limited scanning capabilities are required [2-1].

2.2 The Dragonian configuration

An example of an imaging hybrid antenna is a dual reflector system constituted by two confocal offset paraboloids fed by a planar array, probably introduced in the literature by W.D. Fitzgerald [2-2]. Later on, C. Dragone [2-3] [2-4] [2-5] has patented this antenna system further analyzing it and deriving several design rules. Since the work of Pearson [2-6], the Gregorian co-focal dual reflector system, named here for simplicity also as Dragonian configuration, has been seriously considered as an in-orbit antenna for satellite payloads [2-7][2-8], but it has still never been employed in any space mission.
Offset parabolic reflectors offer a solution in lower the side-lobes levels because the feed is mounted out of the line of sight of the aperture and the longer focal length to diameter *f/d* ratio compared with a symmetrical dish gives increased aperture efficiency.

Figure 2-1 and Figure 2-2 show the cross section, in the elevation off-set plane, of a Dragonian system. Figure 2-2, depicts the electromagnetic interactions between the array and among the reflectors according to Geometrical Optics. The GO theory is introduced in paragraph 2.5.

2.3 Imaging in the Dragonian Configuration

Considering a transmission mode, the sub-reflector is able to convert a plane wave, emerging from the planar array, into a spherical wave centered in the common focus while the main reflector re-converts the spherical wave into a plane wave with magnified transverse cross-section. For reciprocity, the transformations are the same in the receive mode case. The increase in the antenna gain, with respect to the isolated feed array, offered by the dual reflector system depends on the magnification ratio, M, which may be defined in this case from (1.4) considering the off-set configuration as the ratio of the focal length of the main reflector f_m to the sub-reflector f_s or as the ratio of the main reflector aperture size d_a to the array aperture dimension d_0 (the second definition being more general because applicable to the case of shaped reflectors as well). Thus, the magnification factor is:

$$M = \frac{d_0}{d_a} = \frac{f_m}{f_s} \tag{2.1}$$

The optical magnification factor transforms the original feed array to an equivalent feed system where all the geometrical properties are magnified. The array plane and the main aperture plane are termed as conjugate planes.

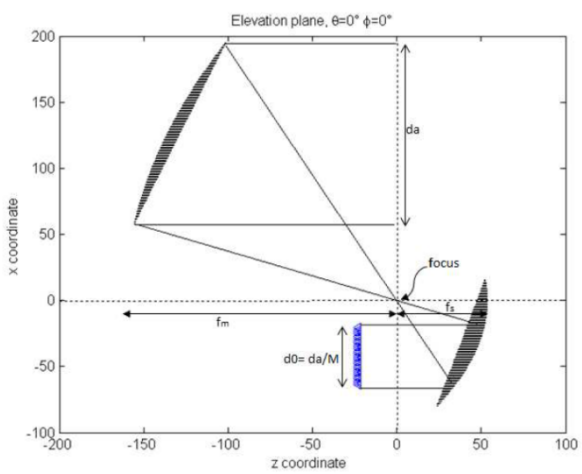

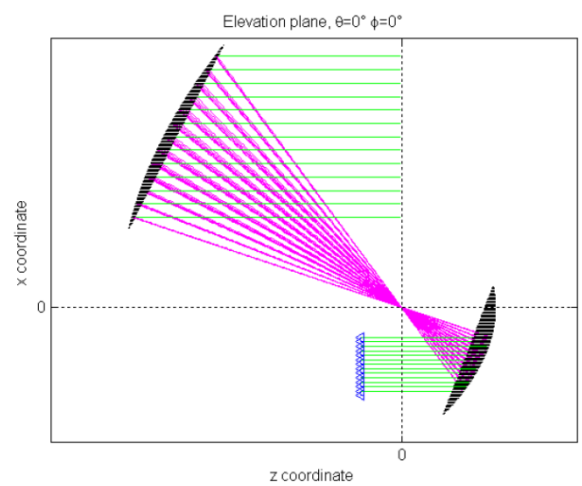

Figure 2-1. View on the elevation plane of the Dragonian system (left)

Figure 2-2. Ray tracing geometrical optics (GO) representation in the elevation offset plane (right)

As a rule of thumb, the main beam emerging from the main reflector is approximately M times narrower, i.e. M times more directive, as compared to the main beam transmitted or received by the feeding array. Furthermore, if θ and φ denote the coordinates which define the pointing direction of the main beam emerging from the array, while θ' and φ' are the corresponding directions relative to the main beam emerging from the main reflector (i.e. the main beam of the entire antenna) then, ideally:

$$\theta' = \frac{f_s}{f_m}\theta = \frac{1}{M}\theta$$

$$\varphi' = \varphi + \pi \tag{2.2}$$

The relations expressed in (2.2) represent a kind of transfer function of the imaging hybrid system between the input and output planes, the conjugate planes.

The accuracy of the equations in (2.2) decreases when increasing the scan angles and the main objective of the research presented here consists in deriving a heuristic non-linear extension for these equations. When scanning the beam originated by the feeding array with respect to the reflectors common axis, the reflected rays originated from the first reflection on the sub-reflector are not perfectly focused anymore in a single point but on a distributed caustic region which moves upwards or downwards depending on the direction of scan (see Figure 2-3 and Figure 2-4). In particular, when the array scans upwards, the main reflector scans downwards and the caustic region moves from the focal point towards the top (Figure 2-3). Vice versa, when the array scans downwards, the main reflector scans upwards and the caustic region moves down from the focal point getting closer to the feeding array (Figure 2-4). Scanning the beam emerging from the feeding array by a certain angle with respect to the boresight direction (coinciding with the direction of the axis of the two confocal paraboloids), corresponds to a tilt of the pattern of the entire antenna roughly M times smaller and in the opposite elevation direction. In addition, the pattern associated to the main reflector is about M times more directive as compared to the pattern generated by the feeding array. However, as already mentioned, the linear equations in (2.2) are well defining the macroscopic behaviour of the entire antenna system but are accurate only for very small scan angles with respect to the boresight direction. For beams deflected significantly from the boresight direction, the offset configuration determines what are defined as phase aberrations [2-5]. Aberrations cause a deviation from (2.2) on the determination of the pointing direction of the main beam in a Dragonian system and will be extensively studied in the next paragraphs.

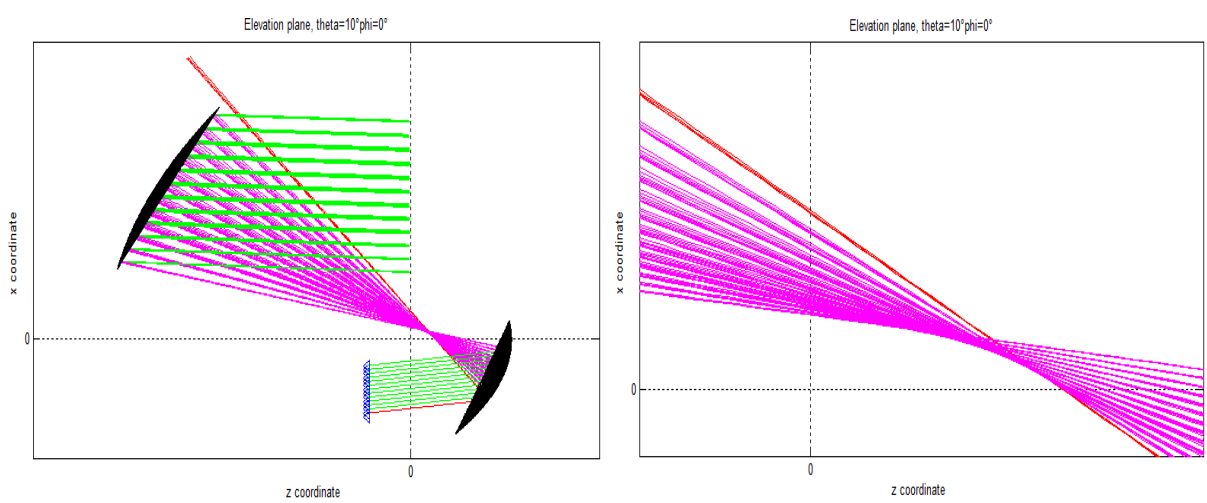

Figure 2-3. (a) GO MATLAB representation (225 rays), up-scan array 10°. Elevation cut. Spill-over is underlined. (b) Zoom on non-perfect focusing: caustic region

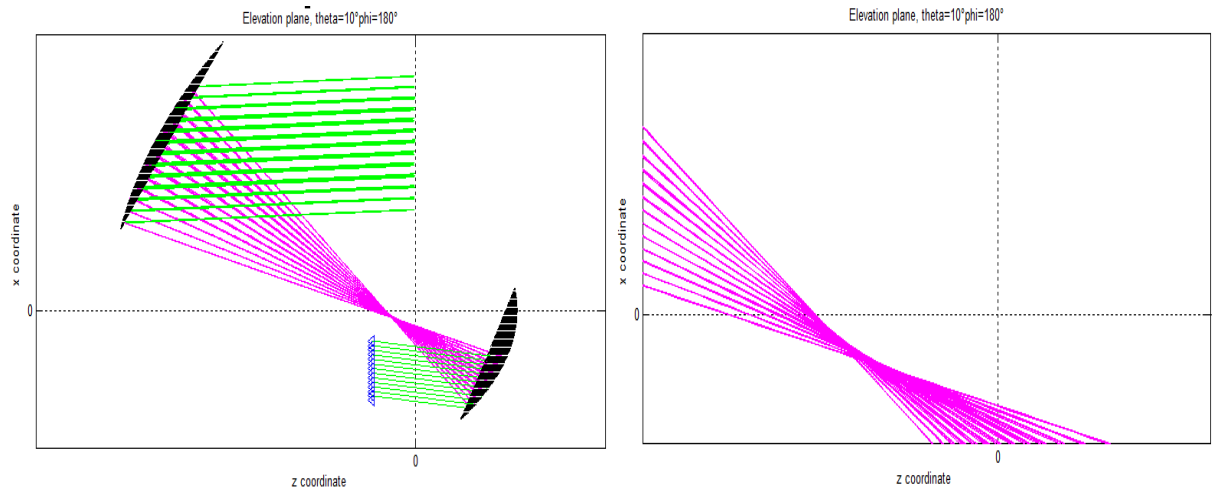

Figure 2-4. (a) GO MATLAB representation (225 rays), down-scan array 10°. Elevation cut. (b) Zoom on non-perfect focusing: caustic region

2.4 Phased arrays

An exhaustive literature exists concerning the theory of phase array systems [2-9]. A phased array is a group of discrete antennas formed along a line or a planar shield or even arranged in a 3D layout, which are usually smaller than the operating wavelength. The radiated field of an array is determined by each individual radiating element. The far-field of an array composed by identical elements can be represented by the single element pattern and by the array factor, with the latter determined by the array architecture and the relative excitations of the elements. Considering a linear array of N identical elements, the array field can be expressed as the superimposition of the individual fields:

$$\vec{E}_{array} = A_1 \frac{\exp(-jk_0 r_1)}{r_1} \vec{e}(\theta,\varphi) + A_2 \frac{\exp(-jk_0 r_2)}{r_2} \vec{e}(\theta,\varphi) + ... + A_N \frac{\exp(-jk_0 r_n)}{r_N} \vec{e}(\theta,\varphi) \tag{2.3}$$

Where A_n is the complex excitation coefficient (containing both amplitude and phase contributes) and r_n is the distance from the *n-th* element to the observation point. If the spacing between the elements is *a*, the array length will be *Na*.

In the plausible hypothesis that $r_n >> Na$ (observation distance much greater than the array length), the following approximation can be used for the exponential terms:

$$r_n \cong r_1 - (n-1)a \sin\theta \cos\varphi \quad \text{with } n = 1,2,...,N$$

Using the same hypothesis, $r_n \cong r_1$ for the denominators of (2.3).

The array field becomes:

$$\vec{E}_{array} = \frac{\exp(-jk_0 r_1)}{r_1}\vec{e}(\theta,\varphi)[\mathrm{A}_1 + A_2 \exp(jk_0 a \sin\theta\cos\varphi) + \ldots$$
$$+ A_N \exp(jk_0(\mathrm{N}-1)\mathrm{a}\sin\theta\cos\varphi)] \tag{2.4}$$

The quantity in square brackets represents the Array Factor (AF).

For a two dimensional array, the following array factor results:

$$AF(\theta,\varphi) = \sum_{n=1}^{N} A_n \exp[jk_x x_n + jk_y y_n] \tag{2.5}$$

where x_n and y_n represent the coordinate of the *n-th* element, while k_x and k_y are defined as:

$k_x = k_0 \sin\theta\cos\varphi$ and $k_y = k_0 \sin\theta\sin\varphi$.

The main result of this formulation is that the beam deflection angle of an array is related to the phase shift between the elements and to their inter-spacing.

Imposing a linear phase taper across an array of transmitting elements scans the equi-phase wavefront away from broadside direction, resulting in a deflection of the main beam. Electronic control of the array phase distribution allows a beam to be rapidly scanned; alternatively, a beam forming network can be used to simultaneously form a set of fixed beam (multiple beams antenna).

The array taper efficiency (ATE) gives a measure of the influence of the individual element taper (depends on A_n) and its distribution on the total aperture efficiency. The array aperture efficiency is, in fact, the product of the ATE and the element aperture efficiency in the array environment.

The array side-lobes can be arbitrarily specified by the correct choice of the aperture distribution, which is dependent on the phase, amplitude and radiation pattern of each element.

Limitations are imposed on the inter-element array spacing; the aperture must be sampled sufficiently to avoid ambiguities in the phase distribution, otherwise grating lobes are produced. The grating lobes shall not be confused with the side-lobes.

2.4.1 Grating lobes

For a quantitative understanding of the grating lobes phenomenon, the array factor of a phased array as expressed in (2.5) can be considered. $AF(\theta,\varphi)$ is a periodic function, being the sine and cosine periodic functions. As a result, the pattern is simply duplicated in distances that depend on the array factor, i.e. on the inter-element spacing.

With an imaging hybrid configuration, the impact of the grating lobes is substantially reduced as the inter-spacing is reduced, considering a fixed number of elements. In practice, when a large phased array is used to scan a narrow pencil beam within a coverage sector, sometimes the number of elements has to be drastically increased only to avoid grating lobes. A smaller phased array, combined in a hybrid configuration, can allow to use the number of elements strictly needed, relaxing the constraint driven by the grating lobes, thus further simplifying the complexity of the system.

2.5 A numerical method for the analysis of the Dragonian configuration

Nowadays, some commercial tools are available for the analysis of dual reflector antennas. In particular, the software GRASP (General reflector and antenna farm analysis software) developed by TICRA is extremely reliable, fast, accurate and it is considered the reference tool for reflector based antennas. Despite the maturity of the GRASP tool, for the present work a numerical hybrid routine based on the Geometrical Optics (GO) and Physical Optics (PO) has been implemented using the MATLAB in order to study the electromagnetic performances of the Dragonian configuration. As well known, to characterize the interactions between the array and the sub-reflector and the interactions between the two reflectors, the GO is sufficiently accurate and extremely fast. Geometrical Optics (GO), or ray optics, theory, describes propagation in terms of "rays". The "ray" in geometric optics is an abstraction, or "instrument", which can be used to model how the radiation will propagate. Is a good approximation for electromagnetic systems where the wavelength is considerably smaller than the objects through which it interacts. In the design procedure, the GO allows to easily make geometrical considerations. For this reason, the number of rays, into which the system is sampled, represents, in effect, a design input. The problem becomes discrete and computationally easily tractable. Depending on the number of rays chosen for the representation, the analysis and the electromagnetic antenna patterns will be more or less accurate in return of a heavier or lighter computational effort. For the far field computation, GO is not sufficiently accurate while the PO, based on a GO approximation of the fields on the reflector and on the evaluation of the corresponding radiation integrals, provide accurate results, especially for electrically large reflectors. The MATLAB procedure implemented is based exactly on this. First of all, the amplitude and phase distribution on the main aperture plane are evaluated as a function of the known amplitude and phase distributions on the array aperture resorting to the approximate GO procedure described in [2-2]. To introduce the procedure, let's consider the most simple case where the array is divided into a two-dimensional square lattice of equally spaced sampling points. This case will be used throughout the whole argumentation, since the purpose of the present study is mainly focused on the study of the aberrations. The index N sets the number of rays traced, as well as the number of sampling points on the main aperture. This parameter determines the trade-off between computational burden and the accuracy of the computed patterns. For each pair of coordinate points x_0 , y_0 and for given θ and φ , the coordinates of the reflection points on the two reflectors have been evaluated and used to determine the optical path length L. The amplitude distribution on the main aperture plane, denoted by $E(x_a(m,n), y_a(m,n))$ is related to the assumed distribution on the array imposing the conservation of energy where m,n are the indices that identify the rays into the square lattice of the array.

Thus, from the energy conservation in a ray tube in GO, the following equation [2-2] may be derived:

$$\left|E_0(x_0(m,n),y_0(m,n))\right|^2 = \Delta x_a(m,n)\Delta y_a(m,n)\ \left|E_a\ (x_a(m,n),y_a(m,n))\right|^2 \tag{2.6}$$

where

$$\Delta x_0(m,n) = x_0(m+1,n) - x_0(m,n)$$

$$\Delta y_0(m,n) = y_0(m,n+1) - y_0(m,n)$$

$$\Delta x_a(m,n) = x_a(m+1,n) - x_a(m,n)$$

$$\Delta y_a(m,n) = y_a(m,n+1) - y_a(m,n)$$

and $\left|E_0(x_0(m,n),y_0(m,n))\right|^2$, $\left|E_a\ (x_a(m,n),y_a(m,n))\right|^2$ represent the radiation densities on the array and on the main aperture, respectively.

$\Delta x_0(m,n)$ and $\Delta y_0(m,n)$, interspaces on the array, are constant quantities since the lattice is regular.

Therefore, it is possible, adopting a simple GO procedure, to derive the field distribution on the main aperture from (2.6):

$$E_a\ (x_a(m,n),y_a(m,n)) = \sqrt{\Delta x_a(m,n)\Delta y_a(m,n)}E_0\ (x_0(m,n),y_0(m,n)) \tag{2.7}$$

Rays which are computed to spill over either the sub-reflectors or the main reflector are excluded in the GO composition of the main aperture discrete field distribution.

The far field pattern $P(\theta',\varphi')$ is then estimated adopting a PO-like procedure, i.e. by numerically implementing a surface radiation integral:

$$P(\theta',\varphi') = \sum_m \sum_n \sqrt{\Delta x_a \Delta y_a}\, E_0(x_a,y_a)\, \mathrm{e}^{-j\Phi(x_a,y_a)}\, \mathrm{e}^{j2\pi fm\ \sin\theta'(x_a\cos\varphi' + y_a\sin\varphi')} \tag{2.8}$$

where the dependence of the coordinates to m,n is omitted.

Figure 2-5 compares the far field pattern obtained by the afore-described hybrid GO/PO approach and a GRASP simulation (complete PO approximation), for the boresight case.

The matching is quite good, the elaboration time is almost the same, but the advantage of having an in-house software routine allows to have the possibility of better investigating the system performances in case of scan, as shown in the following paragraphs.

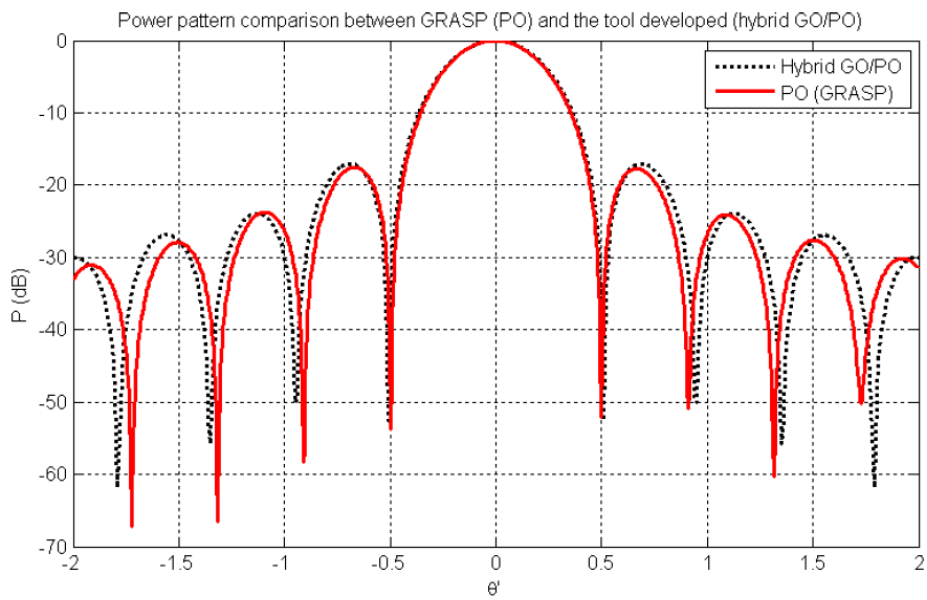

Figure 2-5. Far field comparison between GRASP (P.O.) and MATLAB (hybrid G.O./P.O.) computations

2.5.1 The test configuration

In the present work, a configuration able to generate a 1° First Null Beam Width (FNBW) with a field of view (FOV) of ±8° (corresponding to a full Earth coverage from a GEO satellite), is considered as a reference test configuration. In the following paragraphs, some design rules are derived in order to proper scale the system according to the needs, coping with the characteristic aberrations which will be presented hereafter. In this sense, the conclusion stated in the frame of this work can be considered for a general Dragonian configuration. Contextually, the antenna system designer will have to take always into account the grating lobes phenomenon (characteristic of the arrays) and to reduce the spill-over and the blockage (characteristic of the imaging systems).

In the reference configuration used here, a main circular aperture is selected to be 140λ [2-7] and the positions, as the sizing of the reflectors, have been selected to satisfy the requested scanning capabilities, minimizing blockage and spill-over. An isolated planar array, to satisfy the same pattern specifications without any reflector antennas, would be slightly smaller but the system would be heavier and more complex, as well as more expensive. The system can be specified as frequency independent. The chosen electrical dimensions correspond to a main reflector of 1.4-meters of diameter at 30 GHz. The sub-reflector is dimensioned to allow the desired scan range by the feeding array whose field of view is M times larger as compared to the one of the main reflector (±8°). In particular, due to the impact of the aberrations, the sub-reflector needs a larger oversizing in the upper part than in the lower one as it will be clarified afterwards. The geometrical parameters characterizing the chosen test configuration are listed hereafter:

Table 2-1: Geometrical parameters of the test configuration

Magnification (M)	*3*
Frequency (GHz)	*30*
First null beam width (deg)	*1*
Ratio $f/d = f_s/d_0 = f_m/d_a$	*1.15*
Offset: distance main reflector lower edge from the common axis (cm)	*56*
Ratio center/focal length for the sub-reflector	*0.6*
Ratio diameter/focal length for the sub-reflector	*1.8*
Ratio center of the array/focal length of the sub-reflector	*0.79*
Distance of the array from the focal plane (cm)	*23*

The patterns which follow are computed choosing a GO discretization of the array lattice so that the inter-element spacing is such that the grating lobes are outside the antenna main beam FOV.

2.6 Beam scanning

As mentioned, when the system is not pointing at the boresight direction, all rays are not focused on a single focal point but in a distributed caustic region. This leads to a phase aberration, i.e., a deformation of the image produced over the virtual array on the main aperture. The radiation properties of this antenna system are, as expected, affected by the offset configuration and will be characterized now. Representing a multi-beam coverage, where each beam pattern is computed by scanning the array with steps of 4°, the following figures are obtained, covering the entire desired antenna scan sector of ±8°.

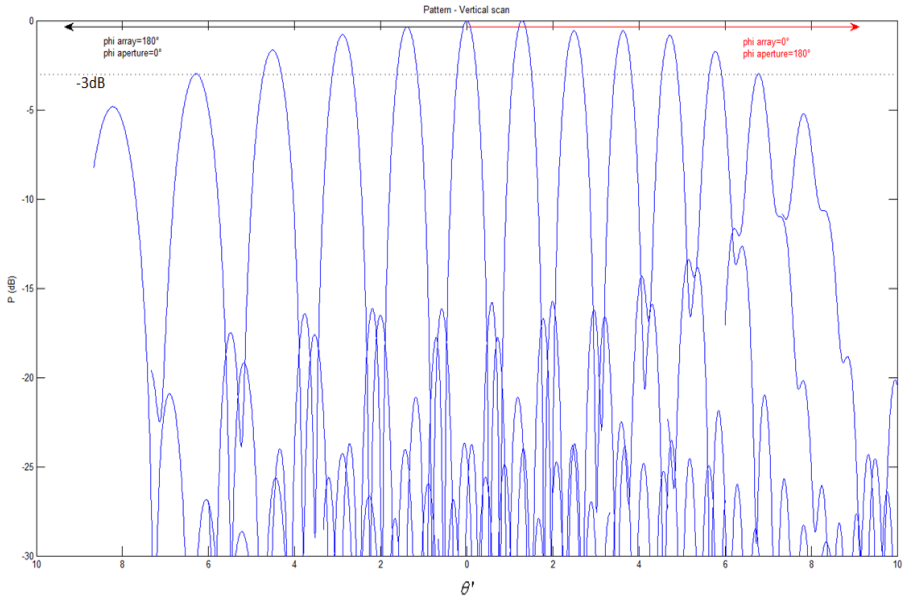

Figure 2-6. Antenna patterns on the vertical (x-z) scan plane with a 4° step on the angles of launch from the array

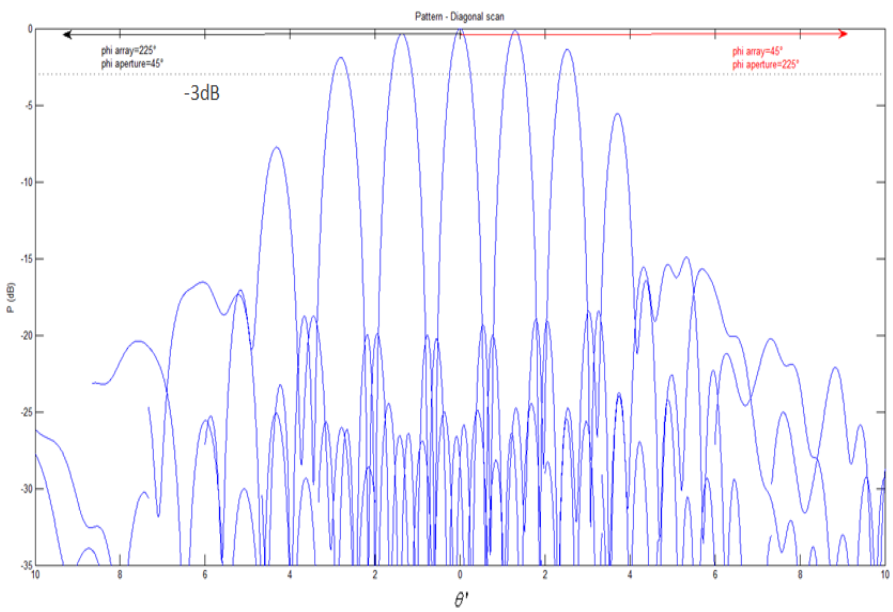

Figure 2-7. Antenna patterns on the diagonal plane (45°/225°)

In Figure 2-6 the plane of scan of the array corresponds to φ=0° when the array is scanning downwards and to φ=180° when the array is scanning upwards. As reflected also in equations (2.2), when the array is scanning downwards the main reflector is scanning upwards and vice versa. So far the pattern is characterized by φ'=180° when φ=0° and by φ'=0° when φ=180°. Due to the vertical offset, only when the array is scanning in this vertical plane the beam emerging from the array and the corresponding

one emerging from the main reflector after two reflections are in the same plane. In this case, only the θ' direction is affected by the offset configuration, as the system is symmetrical in the y-z plane. However, in general, when the array is scanning not only in the vertical plane but also in the horizontal one, the relation between the scanning angles of the array and the corresponding ones of the main reflector becomes more complicated. As a consequence, the representation of the main aperture radiation pattern on the same scan plane of the feeding array scan plane does not permit to visualize exactly the directions of maximum radiation. Moving from the offset vertical plane (characterized by φ=0°, 180° and φ'=180°, 0°) the beams emerging from the main reflector do not have their maxima in the same oblique plane where the feeding array is scanning. To clarify this property, let us assume that the feeding array is scanning in the oblique plane characterized by φ=45° and φ=225°. In Figure 2-7 the corresponding beams emerging from the main reflector are represented in the same oblique plane and, above a certain scan angle, the maxima are clearly lost. The directions corresponding to the maximum radiation, affected by the aberrations are unknown. The aberrations prejudice the formulas expressed in (2.2) and their impact is more relevant, the bigger it is the scan angle.

2.6.1 The beam tracking algorithm (BTA)

In order to evaluate the real pointing direction of the beam emerging from the main reflector, a beam tracking algorithm (BTA) routine has been implemented. The routine calculates the antenna patterns in all possible directions around the expected one, according to (2.2), within a selectable range and with a selectable accuracy. The real direction of maximum radiation of the antenna system is then associated to the absolute maximum value obtained. The 2D pattern is calculated replacing the expected angle φ' with the angle associated to the direction derived numerically, for each beam. As a consequence, in the 2D multibeam representation (e.g., Figure 2-8, continuous line), the angle φ' varies for each beam.

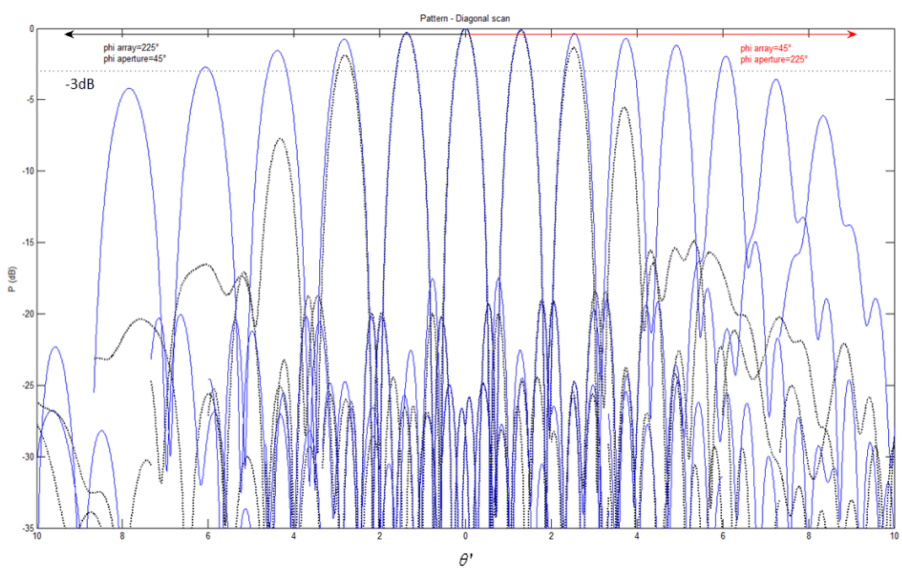

Figure 2-8. Antenna patterns on the diagonal plane (45°/225°) after BTA correction (in dotted line patterns without BTA)

In particular, Figure 2-8 shows the beams in the diagonal plane (black dotted curves) without using the BTA algorithm (as in Figure 2-7) and the beams evaluated in their maximum radiation direction as derived by the BTA algorithm (continuous line blue curves). The accuracy used in the tracking, in this case, is 0.1° for θ' and 0.2° for φ'. It is particularly convenient to adopt an orthographic projection of the coordinates θ' and φ' to visualize the real scanning behaviour underlining the phase aberration for the entire antenna system (Figure 2-9).

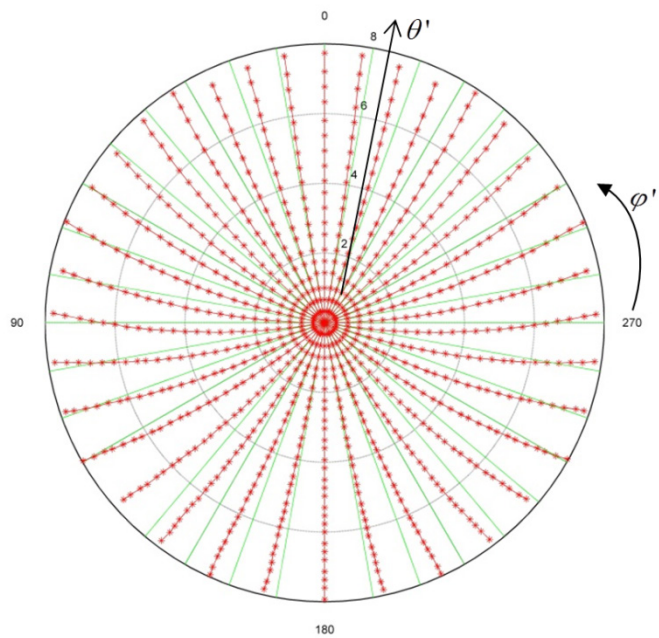

Figure 2-9. Orthographic projection on the main aperture. Real patterns directions (red line with stars) over ideal scanning directions (continuous green line)

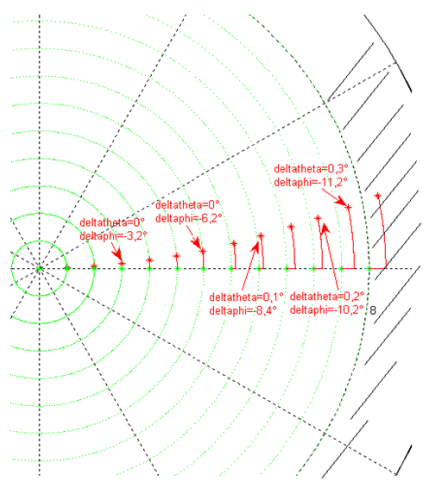

Figure 2-10. Particular on the evolution of the displacements of the output angles along the horizontal plane

In practice, the green straight lines in Figure 2-9 represent the directions where one may expect having the maximum radiation of the beams emerging from the main reflector according to Equation (2.2). Instead, the curved red lines represent the directions where the maxima are effectively located, calculated by the BTA algorithm. So the difference between each couple of lines represents the deformations caused by the offset configuration. From the orthographic projections, it can be also derived that the maximum array scan angle to guarantee 8° of coverage is about 26° in the down vertical scan case from the main aperture while it is around 21° in the up vertical main scan case. The orthographic projections prove that, despite in the vertical scan case the distortions do not affect the φ' angle (but only the elevation angle θ'), in the case of oblique scan both angles (θ', φ') do not respect both equations in (2.2), as the scan from the boresight direction is increased. In the limit case of completely horizontal scan (i.e., array scanning in the *y-z* plane) the distortions affecting both (θ', φ') angles are maximized. In particular, considering θ' for upward scanning (upper part of the orthographic circle) there is an expansion of the real pointing angles (respect to the expected ones) along a distorted (curved) plane depending on φ'. Otherwise, for downward scanning (lower part of the circle) there is a contraction of the θ' angles, respect to the expected ones. For this reason, the two reflectors are asymmetrically oversized.

2.6.2 Determination of the errors on the predicted directions

Adopting the BTA algorithm, it is possible to estimate the errors caused by the aberrations on the main beam direction angles. The following figures represent the computed variations between real and expected directions of the main beam, both for θ' and φ'. They extent what presented in Figure 2-9 and Figure 2-10.

The plot of Figure 2-11 shows the behavior of the $\Delta\varphi'$ function of both θ and φ.

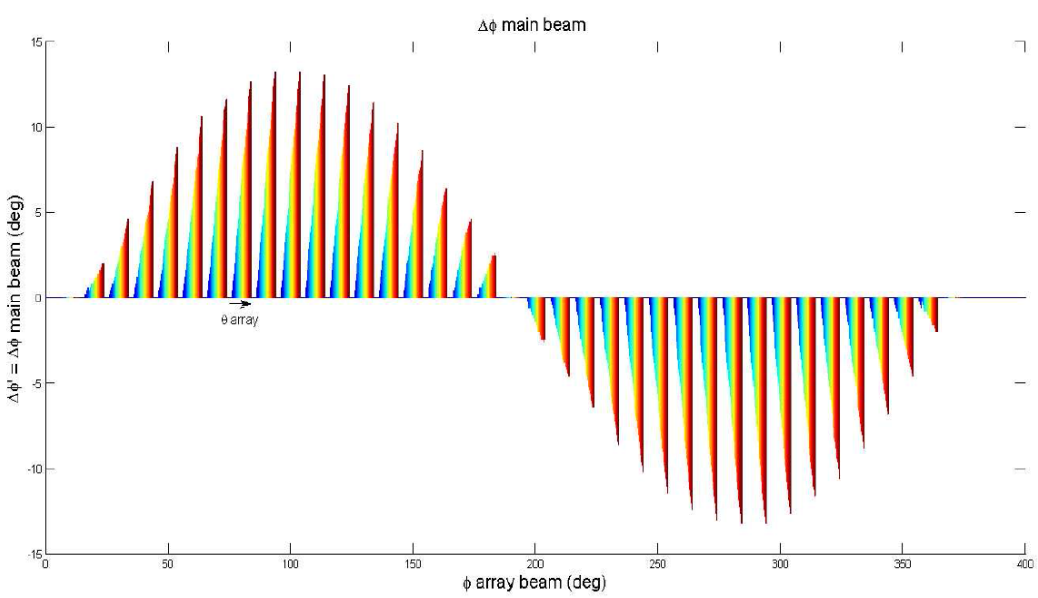

Figure 2-11. $\Delta\varphi'$ **function of** θ **and** θ

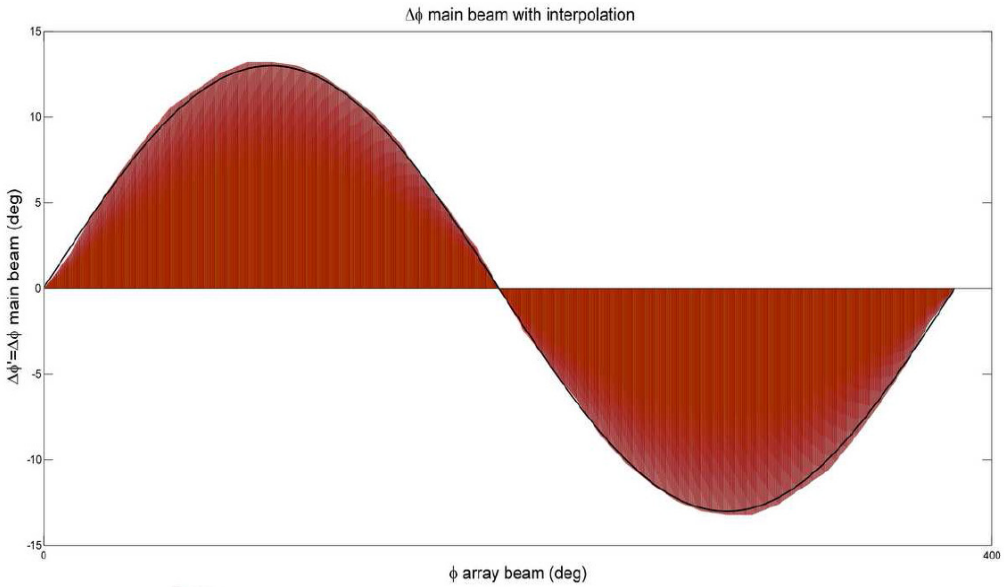

Figure 2-12. Interpolation for continuous φ and fixed θ = 26° (maximum)

In Figure 2-11, φ is considered to vary in steps of 10° from 0° to 360° and, for each plane individuated by φ, θ is varying from 0° to 26° (angle permitting to fulfill completely the Earth coverage from a geostationary satellite) in steps of 1°.
With a simple interpolation, the behavior can be generalized for each $\Delta\varphi'$ (and a fixed θ). An ideal sinusoidal behavior is underlined in Figure 2-12.

Overall, one may conclude that:

$$\Delta\varphi' = K1\sin(\varphi) \tag{2.9}$$

where the quantity $K1$ is clearly a function of θ, the magnification *M* and the ratio *f/d*.

Varying θ in steps of 1° (from 0° to 26°) the sinusoidal behavior is confirmed (see Figure 2-13).
Plotting the $\Delta\varphi'$ (main aperture beam) as a function of the θ of the array (for a fixed φ), a quasi-linear dependence can be appreciated (see Figure 2-14).
The not perfect linearity of the curves depicted is due to the numerical approximation of the BTA. The quantity defined as $K1$, which corresponds to the amplitude of the sine function individuating the relationship between φ' and φ, can be derived from the curve corresponding to φ=90°. For the test configuration proposed (*M*=3, *f/d*=1.15), $K1$ is well interpolated by the relation $K1 = 0.51 * \theta$.

Therefore:
$\Delta\varphi' = 0.51 * \theta\sin(\varphi)$

It represents the first of the two relationship which links the real and theoretical directions of main beam scan.

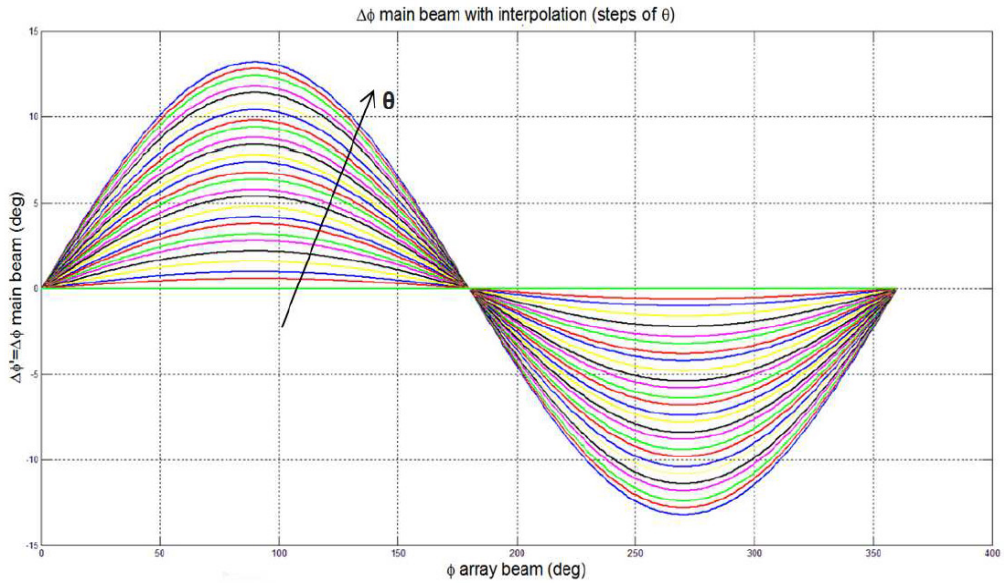

Figure 2-13. Interpolation showing $\Delta\varphi'$ for continuous φ and 27 case of θ (from 0° to 26°: step 1°)

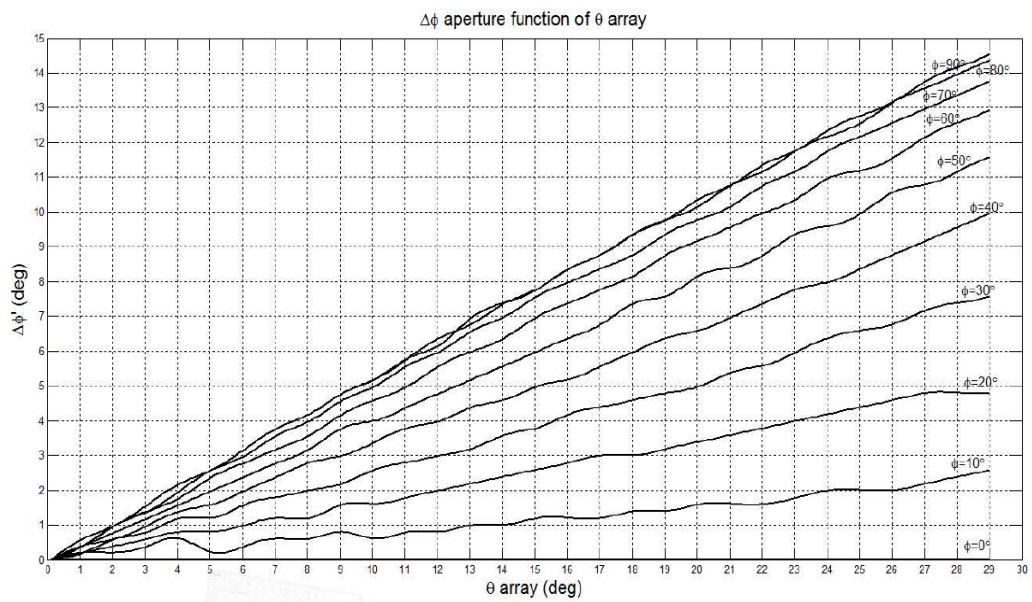

Figure 2-14. $\Delta\varphi'$ function of θ for 10 cases of φ (from 0° to 90°; step 10°)

Based on these results, a new improved equation may be presented for the azimuthal scanning properties of the antenna system.

$$\varphi' = \varphi + \Pi + \Delta\varphi' = \varphi + \Pi + K1 * \theta \sin(\varphi) \tag{2.10}$$

Equation (2.10) represents a generalization of the second equation in (2.2).

A similar analysis has been implemented in order to characterize $\Delta\theta'$.

A saturation behavior can be observed in Figure 2-15 in the case of upward scan. It is due to the fact that the sub-reflector is exactly dimensioned for an Earth coverage ($\pm 8^\circ$). For upward scan, this is achieved with a scan angle of around 21° on the array, while 26°, as already specified, are required only for main scan downwards. Removing this constraint (which in any case refers to the best system dimensioning), a quick interpolation can be performed on the data. The behavior in Figure 2-16 is obtained, showing that:

$$\Delta\theta' = K2\cos(\varphi + \Pi) \tag{2.11}$$

Where $K2$ is a function of θ, M and f/d.

In Figure 2-16, θ reaches 27° with a granularity of 3°.
Plotting the $\Delta\theta'$ (main aperture beam) as a function of the θ of the array (see Figure 2-17), a quasi-linear behavior is found again, although sensibly smoother than for the $\Delta\varphi'$. The quantity $K2$ can be derived from the curve corresponding to $\varphi = 180^\circ$.
For the present test configuration, the following extrapolation has been derived: $K2 = 0.086 * \theta$.

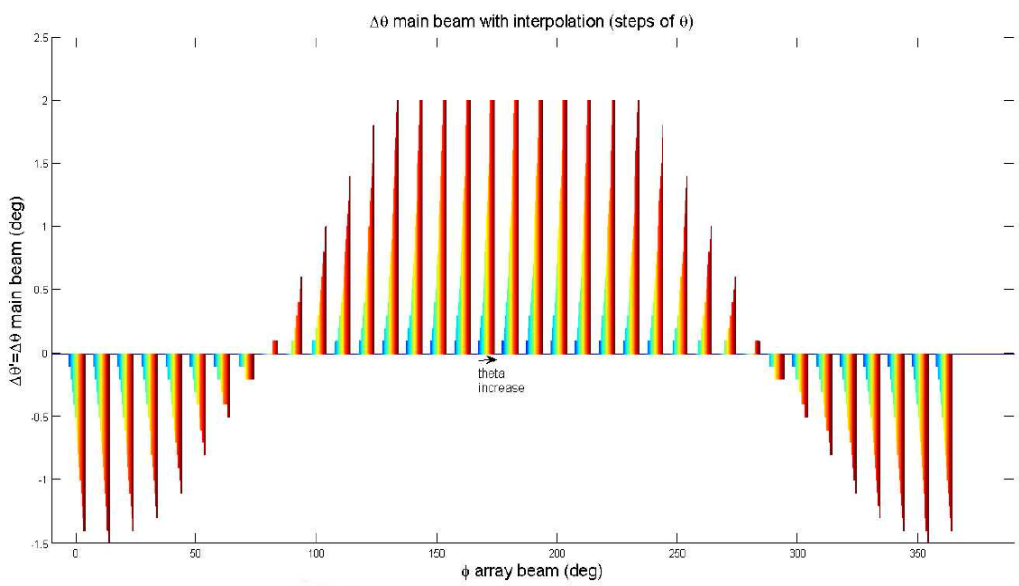

Figure 2-15. $\Delta\theta'$ function of θ and φ. θ varies from 0° to 26° (1° step) for every 0° ≤ φ ≤ 360° (10° step)

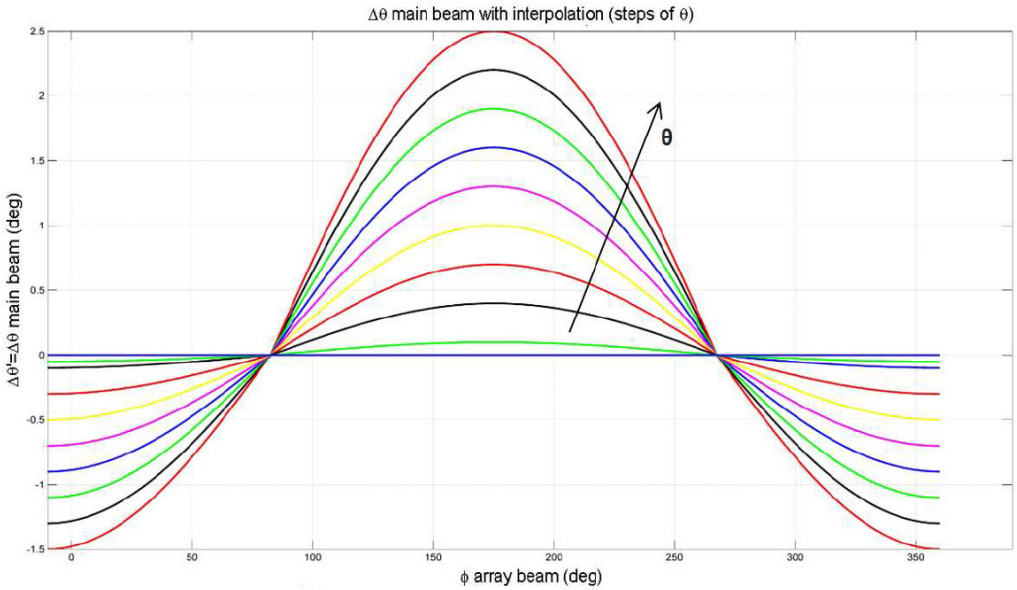

Figure 2-16. Interpolation showing $\Delta\theta'$ for continuous φ and 10 cases of θ (from 0° to 27°, step 3°)

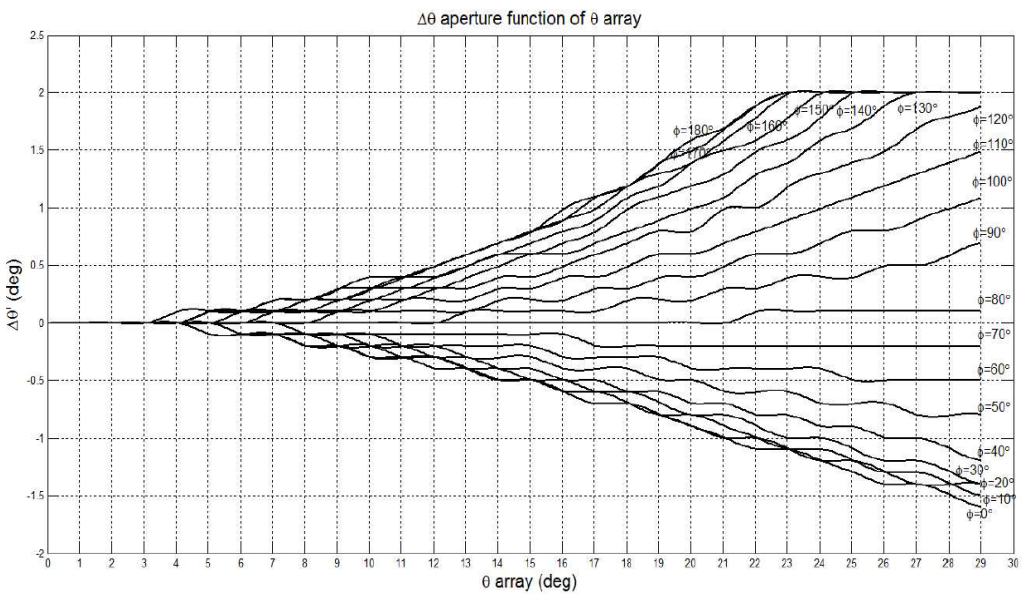

Figure 2-17. $\Delta\theta'$ function of θ for 19 cases of φ (from 0° to 180° ; step 10°)

Considering the first equation in (2.2), we can re-formulate it as:

$$\theta' = \frac{1}{M}\theta + \Delta\theta' = \frac{1}{M}\theta + K2 * \theta\cos(\varphi + \Pi) \tag{2.12}$$

Since smaller variations on $\Delta\theta'$ are obtained (as respect to $\Delta\varphi'$), a better accuracy of the BTA is in general needed in this case, as underlined by the ripple in the curves in Figure 2-17. Nevertheless, this is considered, at present, a point of improvement for the BTA routine, since the actual code would lead to very large computational times. The saturation previously justified is visible also in Figure 2-17.

In conclusion, the empiric laws derived:

$$\Delta\varphi' = K1\sin(\varphi)$$

$$\Delta\theta' = K2\cos(\varphi + \Pi)$$

allow to redefine the "transfer function" in (2.2) for an offset Dragonian configuration according to:

$$\begin{aligned} \varphi' &= \varphi + \Pi + a\theta\sin(\varphi) \\ \theta' &= \left(\frac{1}{M} + b\cos(\varphi + \Pi)\right)\theta \end{aligned} \tag{2.13}$$

where each of the new angles of the main scan depends on both the angles of the array scan. a and b are two simple scalars derived extracting θ from $K1$ and $K2$. a and b depend exclusively on M and f/d.

Having characterized the Dragonian configuration via the new transfer function derived in (2.13), one may think of adopting array excitations techniques to compensate the distortions, i.e. the aberrations, introduced by the imaging hybrid system, as already done to compensate distortions of the reflector antenna surfaces caused by manufacturing tolerances or ageing [2-7].

2.6.3 Dependence on M and f/d

Ultimately, let us consider the two characteristic parameters which define the Dragonian system. The magnification factor (M) and the ratio between focal distance and diameter (f/d). The reference test configuration considered M=3 and f/d=1.15. Nevertheless, a larger set of combination can be deemed suitable for the best optimization of the system with respect to the desired field of applications. Therefore, other solutions were validated with the BTA approach. The method implemented allows to determine easily the coefficients $K1$ and $K2$, depending on the configuration selected (i.e. on M and f/d).
The analyses showed, in general, that with lower M, higher $K1$ and $K2$ coefficients are obtained.
Higher $K1$ and $K2$ coefficients are obtained as well with lower f/d.

The analysis of suitable ranges for the two parameters was also part of the study. It has been demonstrated that high values for the magnification factor cause lower distortions (see Figure 2-18), but require higher scan capabilities for the array feed and imply a reduced compactness so that a trade-off should be performed. Vice versa, there is a higher flexibility in the selection of the ratio between the focal length and the diameter (see Figure 2-19); in practice, the minimum value which guarantees an absence of blockage can be used.

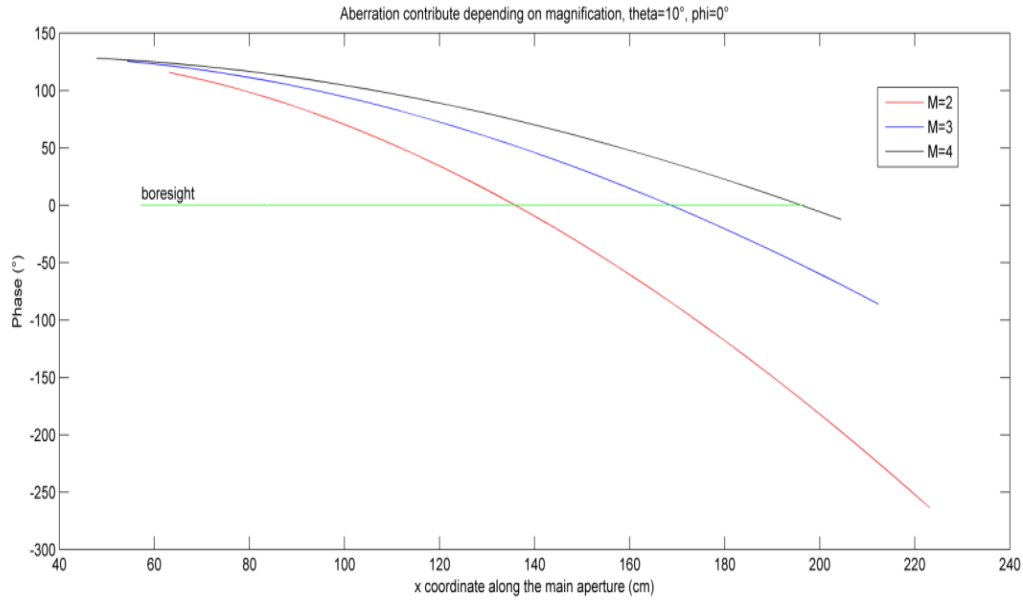

Figure 2-18. Aberrations on the phase on the main aperture in case of M=2,3,4

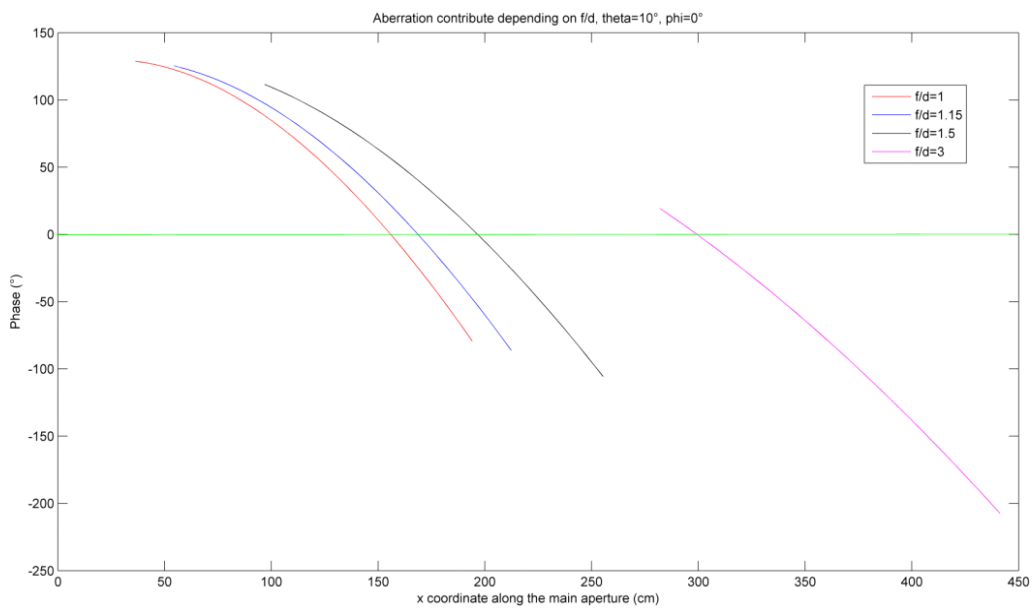

Figure 2-19. Aberrations on the phase on the main aperture in case of f/d ratio of 1,1.15,1.5,3

2.7 Conclusion

An imaging dual reflector hybrid antenna fed by a planar array has been presented and its properties investigated. The configuration, termed as Dragonian antenna, represents an extremely valid solution in order to reduce the weight, the complexity of the implementation and the encumbrance of spaceborne modern payload antenna systems. In fact, with such layout, a large and dense array matrix is not needed, allowing also at reducing the impact of the grating lobes. This is achieved at the cost of compensating for the non-linearity (i.e. aberrations) introduced by the off-set configuration. In this context, heuristic equations, representing an extension of the linear equations available in the literature, have been derived which permit predicting the system's pointing direction as a function of the pointing direction of the feeding array in a significant field of view. All the proposed equations may be used for arbitrary configurations with an assigned magnification factor (M) and ratio between focal length and diameter (f/d). It has been verified that the equations are extremely accurate when the system is scanning up to more than 10 beamwidths in all the directions starting from the boresight direction. The validity of the equations remains good even extending further the field of view. However, this extension is, in general for such systems, not recommended because spillover, blockage, cross-polarization effects are seriously affecting the radiative performance. Inside the field of view identified, a fine tuning of the antenna performance in case of electronic scan may be obtained by implementing a pre-mapped excitation of the feeding array, according to the equations presented. In addition, other solutions as shaping of one or both reflectors, mechanically modifying the reciprocal positions of the array versus the two reflectors, as proposed in [2-7] can be implemented.

References

[2-1] N. Gatti, A. Catalani, L. Russo, P. Rinous, and G. Toso, Shaped confocal antenna fed by active sparse array for multibeam satcom applications, *34th ESA Antenna Workshop*, Noordwijk, The Netherlands, 2012.

[2-2] W. D. Fitzgerald, Limited electronic scanning with an offset-feed near-field Gregorian system, *ESD-TR-71-272, Technical Report 486*, Lincoln Laboratory, 1971.

[2-3] C. Dragone and M. J. Gans, Imaging reflector arrangements to form a scanning beam using a small array*, Bell Syst. Tech. J.*, Vol. 58, No. 2, 501-515, 1979.

[2-4] C. Dragone et al., Scannable antenna arrangements capable of producing a large image of a small array with minimal aberrations, *U.S. Patent 4203105*, May 13, 1980.

[2-5] C. Dragone, Theory of imaging in Cassegrainian and Gregorian antennas, *IEEE Trans. Antennas Propag.*, Vol. 34, No. 5, 689-701, 1986.

[2-6] R.A. Pearson, An array-fed dual reflector antenna, Ph.D. Thesis, 1988.

[2-7] J. B. L. Rao, Bicollimated offset Gregorian dual reflector antenna system, *U.S. Patent 4755826*, Jul. 5, 1998.

[2-8] J. A. Martinez-Lorenzo, A. Garcia-Pino, B. Gonzalez-Valdes, and C. M. Rappaport, Zooming and scanning Gregorian confocal dual reflector antennas, *IEEE Transactions on Antennas and Propagation*, Vol. 56, No. 9, Sep. 2008.

[2-9] A.K. Bhattacharyya, Phased array antennas, John Wiley & Sons INC., 2006.

Chapter 3

GROUND-BASED ANTENNAS FOR SPACE COMMUNICATIONS

How a ground-based antenna shall be?

A ground-based antenna shall be as powerful, versatile and sustainable as permissible by its application.

3.1 The electromagnetic eyes to space

A ground-based antenna for space applications is a terrestrial terminal designed for either the communication with a spacecraft or the reception of radio waves from an astronomical radio source. In this last case, the antenna can be termed also as a ground radio telescope. When a ground antenna is functionally designed to perform the tracking of a spacecraft, to receive its telemetry and to transmit to it commands, the antenna can be termed as a TT&C antenna (see also Chapter 1). When ground stations are specifically conceived for deep-space missions, they are referred to as deep-space antennas. In Chapter 1, it was assessed that the gain required by a ground station antenna depends primarily on the distance, i.e. on the orbit, of the spacecraft communicating with the ground antenna. Accordingly, the size, the complexity and the costs, as well as the electromagnetic impact of the ground antenna can significantly vary. At the same time, since during a LEOP the orbital predictions cannot be so accurate and the launcher position is characterized by a huge dispersion area, the performance required by the ground antenna may, alternatively, rely preferably on the tracking capability rather than on the achievable gain. An excursus of technological solutions from a simple terminal for the tracking of space launchers to deep space TT&C antennas is probably the best way to understand how a ground-based antenna shall be. Some design rules and approaches are given for the types of antennas introduced. At the end of the present chapter, an extensive study is presented concerning the upgrade of a radio telescope into a TT&C deep space antenna.

3.2 Tracking a launcher

Tracking consists of maintaining the axis of the antenna beam in the direction of the satellite in spite of movement of the satellite or the station [3-1]. Launchers tracking support implies vehicle telemetry reception and is indispensable for flight safety and accurate spacecraft separation. Above all technical and operational challenges, paramount are the uncertainty of the launcher trajectory dispersion during the first phases of the flight, the high speed of the launcher and the continuous frequency swapping

due to the launcher's spin. As an example, more than 1500 parameters are received globally from the Ariane-5 launcher vehicle and recorded throughout the flight (from launch to separation of the payload) [3-2]. Dedicated tracking stations are developed on Earth, for instance by the European Space Agency, for the support of the Ariane-5, Soyuz and Vega launchers.

Figure 3-1. Launch of Ariane-5 at Kourou (French Guiana) – credits to ESA

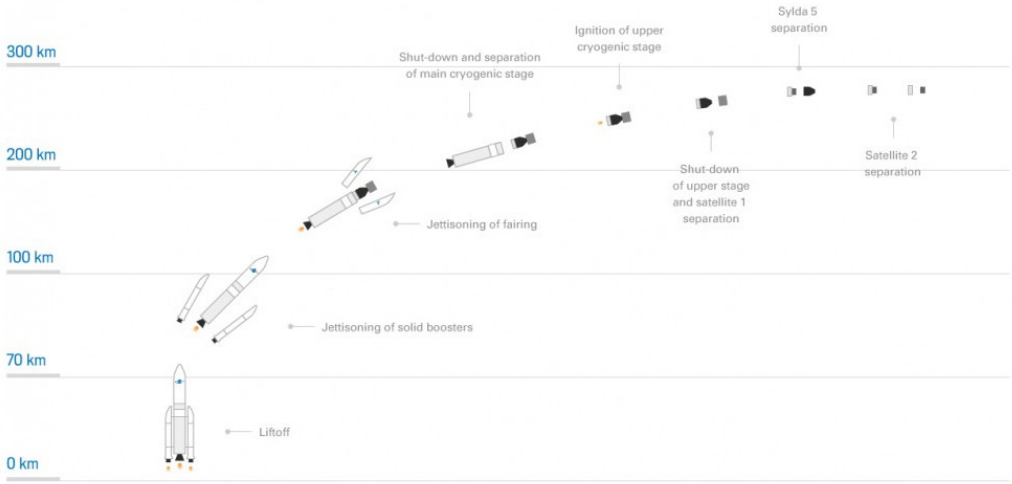

Figure 3-2. Ariane 5 launch phases from lift-off to satellite separation – credits to ESA

ESA's launchers tracking stations are located on the island of Santa Maria in the Azores archipelago and in Perth, Australia. While for long ballistic or steady-state flight phases it is possible to use on-board data recorders to cover the reception holes between one ground station and the following, for some key phases, e.g. engine start/shutoff and stages or payload separations, the real-time data reception is mandatory, so requiring the positioning of specific receiving facilities in the right geographical locations. For this reason the ESA tracking stations, part of the ESTRACK network, belong also to the so-called "Ariane network", composed of several facilities, fully or partially dedicated to the launch vehicle telemetry reception, located throughout the whole globe.
For instance, Santa Maria is ideally located to acquire signals from launchers climbing up toward the North-East from the launch site in Kourou (French Guyana). The antenna in Santa Maria, built in 2007 [3-3], is designed to track a launcher during the first propulsion and ballistic phases of a LEOP of a space mission up to spacecraft's separation. The antenna is tailored to receive Ariane 5 telemetry at 1 Mb/s. The antenna in Santa Maria is an S- and X-band receiving only Cassegrain antenna, fitted with a shaped 5.5 meters parabolic main reflector on a *Y over X* mount and a dichroic not shaped sub-reflector. In practice, the antenna is used as a prime focus single reflector antenna during launchers tracking in S-band, being the X-band functionality reserved for outsourced Earth observation missions. The antenna of Santa Maria has a G/T of 16.57 dB/K and an HPBW of 1.7deg at 2200 MHz. The requirements of a tracking antenna like the one in Santa Maria are not driven by the achievable gain and the efficiency, but by an autonomous tracking (auto-track) capability over a large spatial range. In fact, the auto-track capability is crucial for launchers tracking as the pointing predictions may not be as accurate as for satellites in well-known orbits. The acquisition range for tracking is inversely proportional to the beam-width of the antenna, therefore to the antenna diameter.

Figure 3-3. Santa Maria 5-5-m tracking ground antenna

The author of this thesis has been involved during 2012 in the second development of the prime focus S-band feed for the tracking station of Santa Maria [3-4]. The feed is based on the use of a four element array of crossed dipoles. The four cavity-backed crossed dipoles, printed on a dielectric substrate, are aligned in pairs with the antenna axes *H* and *V* (two for each axis). Each of these pairs of cavities is used to obtain the tracking signals of each axis. The received signal is formed at a multiplexing unit combining the signals received individually by each dipole and represents the main reference signal (boresight signal). A sequential lobing is therefore performed through a sequential switching via an electronic scanning board. The scanning board provides the synchronous switching of the lobes together with the detection of the signals. The scanning sequence will be *S, A, B, C, D, S, A, B* etc., such that the output is formed by a sequence of the main received sum signal *S* and the individual signals from the outer dipoles (denoted as *A,B,C* and *D*). The scanning sequence is controlled by the Electronic Scan Discriminator and Controller (ESDC). The ESDC is in charge of performing the detection of the amplitude envelope in a non-coherent way, separating the main signal and the signals from the outer dipoles and computing the error signals since it knows the scanning sequence. The phase feature is not taken into account since the detection is non-coherent. The signals *B* and *D* are used to determine the *H* axis errors, the *A* and *C* signals, the *V* axis errors. The axes errors are fed into the so called tracking receivers which close the servo loop and derive the voltages to properly drive the antenna motors with the goal of nulling the difference for each axis. The feed is such that it is possible to receive two signals with the same frequency and different polarization (polarization diversity, each chain devoted to one polarization) or two different frequencies with the same polarization (frequency diversity, each chain devoted to one frequency).
The Electronic Scan Discriminator and Controller is able to determine the maximum signal both in polarization diversity mode or in frequency diversity mode.

A *Y over X* mount has been selected for the tracking station of Santa Maria since it does not have any limitation in tracking zenith passes.
Furthermore, it allows the use of same components in both axes, in order to achieve lower configuration's price and easier maintenance. On the other hand, an *Elevation over Azimuth* mount guarantees in general more precise and smoother pointing since it can directly swivel in azimuth and require less axes movement and therefore reduced workload for the drive system. But, the Elevation over Azimuth is not able to support zenith passes. The limitation of zenith passes is also known as a keyhole and corresponds to an area in the sky where an antenna cannot track a spacecraft.

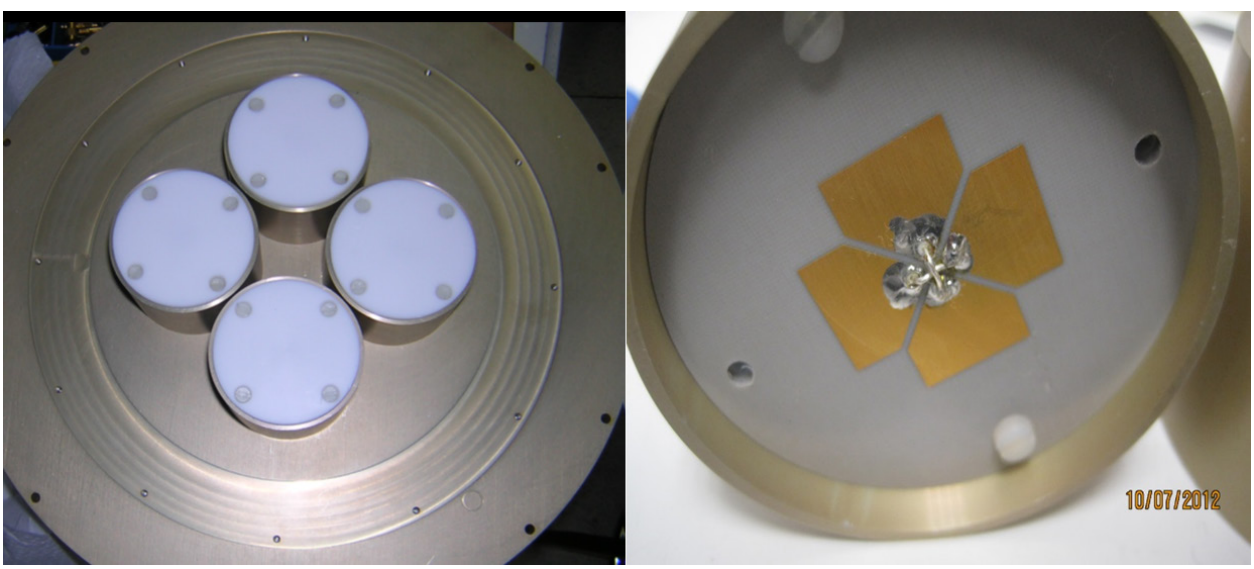

Figure 3-4. Front-end dipoles of the S-band feed (left) and particular on one cavity-backed crossed dipole (right)

If a spacecraft was to pass directly overhead, the Elevation over Azimuth antenna would rise in elevation until it reached its straight-up maximum near 90°. But then the antenna would have to whip around rapidly in azimuth as the spacecraft is, for example, first on the east side of the antenna and then, a moment later, is on the west. The antennas slew rate is not fast enough to track that way, so there would be an interruption in tracking until acquiring on the other side. Elevation over Azimuth antennas are often equipped with a third tilted axis to bend over backwards, or "plunge" in elevation, so to annul the keyhole. This is implemented, as for example, in the ESTRACK TT&C antennas of Kiruna, Sweden (see also Figure 3-9), located beyond the Arctic circle, where zenith passes can be frequent in supporting LEO polar orbit missions.

In this context, the author of the present thesis has been collaborating with the Westphalia University of Applied Sciences in Gelsenkirchen, Germany, on the development of an antenna simulator for the determination of the antenna tracking capabilities based on the orbital parameters of a spacecraft. The performance provided by the different mounting solutions were analyzed. A comparison between *Elevation over Azimuth* and *Y over X* mounts is given, among the others, in the figures and the tables below for a test satellite pass. The tracking predictions performed by the simulator were validated with the actual antenna angular movements recorded by the Antenna Control Unit (ACU), connected to the antenna servos, during ESA's satellites test passes (see Figure 3-8).

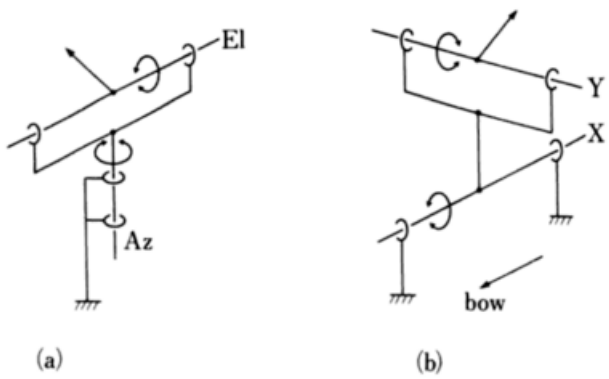

Figure 3-5: Pictorial representation of the *Elevation over Azimuth* mounting concept (a) versus the *Y over X* concept (b)

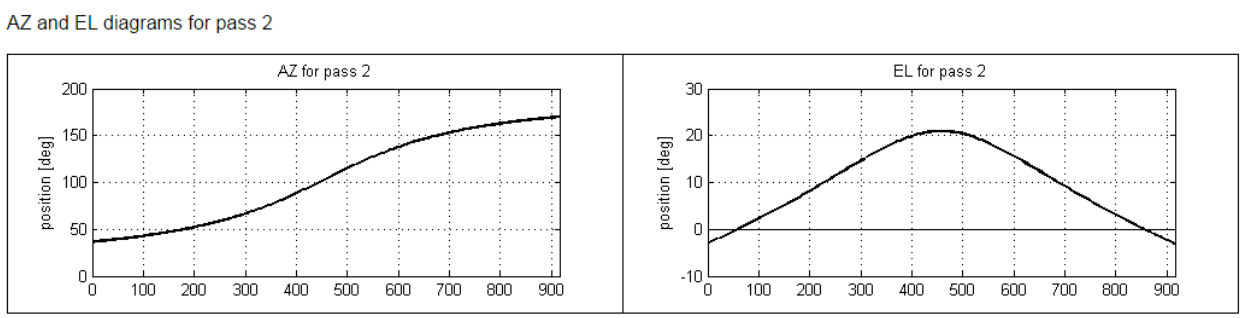

AZvel_max [deg/s]	AZacc_max [deg/s²]	ELvel_max [deg/s]	ELacc_max [deg/s²]	R_AOS [km]	AZ_AOS(*) [deg]	R_LOS [km]	AZ_LOS(*) [deg]	R_min [km]	R_max [km]
0.27	0.00	0.08	0.00	3611	36	3634	170	1706	3634

Figure 3-6: Analysis of the antenna simulator for a test pass considering an *Elevation over Azimuth* mount

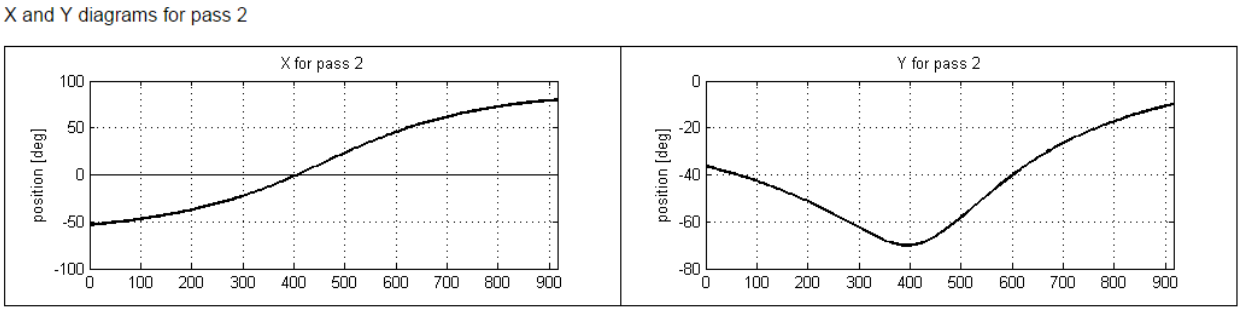

Xvel_max [deg/s]	Xacc_max [deg/s²]	Yvel_max [deg/s]	Yacc_max [deg/s²]	R_AOS [km]	R_LOS [km]	AZ_LOS(*) [deg]	R_min [km]	R_max [km]
0.25	0.00	0.19	0.00	3611	3634	170	1706	3634

Figure 3-7: Analysis of the antenna simulator for the same test pass considering an *Y over X* mount

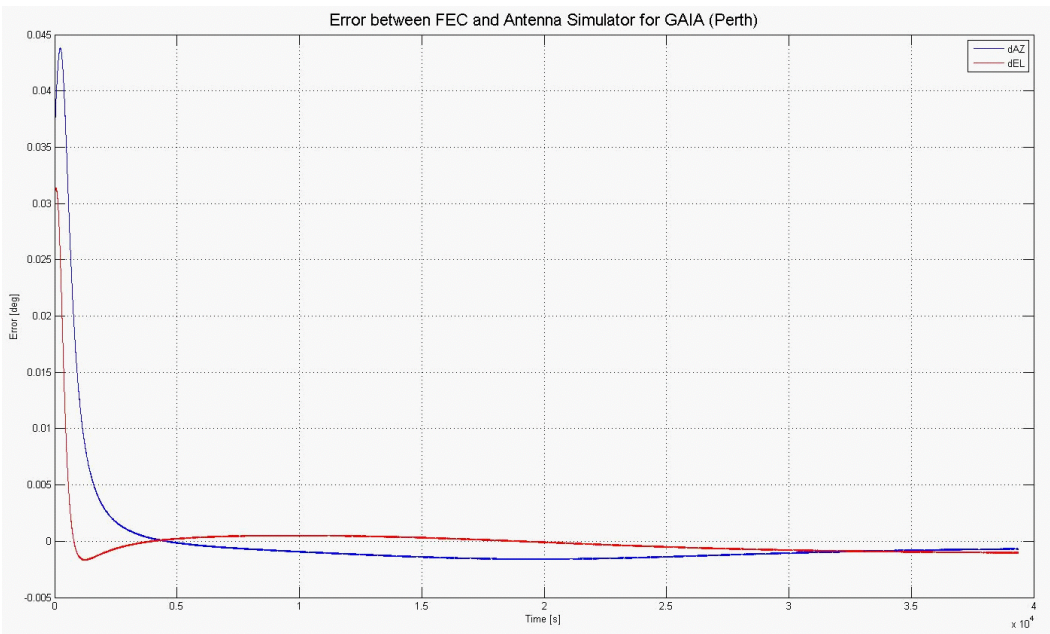

Figure 3-8: Evaluation of the error in Azimuth and Elevation between the antenna simulator predictions and the actual antenna (Perth antenna) movement for a satellite (GAIA) pass

The sequential lobing implemented in the tracking station of Santa Maria is one of the possible techniques of performing auto-track and possibly the easiest. Auto-tracking thorough monopulse tracking is probably the most advanced and complex closed loop tracking system employed in ground station antennas [3-1]. This approach makes use of a particular class of higher-order modes, which present radiation patterns exhibiting a central null in correspondence to the fundamental mode central maximum. The higher modes selected in the monopulse tracking system are extracted by a so called tracking coupler. As described in [3-5], the modes most commonly employed are TM01, TE21, and TE01 in circular waveguides, and TE11 and TM11 in rectangular waveguides. Ideally, i.e. when the antenna is perfectly aligned with the satellite, the null of the higher order mode used (also known as delta mode) coincides with the peak of the fundamental mode (also known as sum mode). If the alignment is not perfect, the not-null higher order

modes extracted by the tracking coupler and redirected to a unit denominated tracking receiver are compared to the sum mode, in order to compute the off-pointing angle and subsequently correct for it. The higher order modes present a steep central characteristic slope around the null for the amplitude and a phase pattern linearly varying around the null. To perform auto-tracking in both polarizations, two orthogonal higher order modes are used. A monopulse tracking is implemented in the 15 meters class of ESA TT&C antennas of the ESTRACK network, for which the author is one of the main technical responsible at ESOC for sustaining and development projects.

3.3 ESA TT&C 15-m antennas

The ESA 15-m class antennas are devoted to the support of LEOPs and the daily TT&C operations of LEO/MEO space missions. High elliptical orbits, which overtake GEO altitudes (as Integral, which apogee is around 150000 Km) are also supported with limited performances on the data rate. For this kind of support, the required gain starts to be significant and thus the size of the antenna. A large reflector aperture provides high gain, which is required for high speed data transmission, and consequently a very narrow beam. The automatic tracking system implemented in such an antenna permits to follow the spacecraft trajectory with a very high accuracy. A double reflector optics is adopted with the goal of maximizing efficiency according to what discussed in the Chapter 1 of this dissertation. Ground antennas with a diameter's aperture of 15 meters are required especially to cope with link budget requirements for LEO/MEO satellites operating in X-band (15 meters correspond approximately 400 wavelengths in X-band). In general, the use of a Cassegrain layout is probably the best configuration as previously explained in Chapter 1. The Cassegrain configuration is used in all the 15-m ESA ground antennas.

Figure 3-9: Kiruna 15-m ground antenna (KIR-1) equipped with a *tilt over Elevation over Azimuth* mount to cope with very high elevation passes

As illustrated in Chapter 1, the total efficiency for an aperture antenna is given by the product of the aperture efficiency and the radiation efficiency, with the latter including the contributions from reflectors spill-over, ohmic losses, heating losses, phase non-uniformity, blockage, surface roughness losses and cross polarization. Therefore, the efficiency of a dual reflector antenna is mainly determined by the ability of its source to illuminate the main dish evenly, both in terms of amplitude and phase (i.e. illumination efficiency), to minimize the energy that does not intercept the reflectors (spill-over efficiency) and to minimize the amount of power blocked by the sub-reflector and by the feed itself (blockage efficiency). Whereas blockage may be reduced (but not eliminated) by appropriately sizing the sub-reflector [3-6] and the feed cone, illumination and spill-over efficiencies tend to be inversely proportional and any attempt to increase the degree of uniformity of the illumination will result in a concurrent increase of the spill-over. In the same way, a low spill-over solution (i.e. high spillover efficiency) will result in a poor illumination efficiency. This cannot be completely controlled for the main reflector by the sub-reflector due to its inability of modifying the feed pattern beyond a mere magnification in classical dual reflector systems. Nevertheless, shaping approaches can be adopted to optimize the illumination efficiency and minimize the spill-over for a determined range of frequencies. Techniques for maximizing the antenna gain and aperture efficiency of reflector antennas involve as well control of the illumination function of the feed. An ideal feed system has a very rapid energy cut-off at the reflector edge, thereby maintaining relatively uniform reflector illumination while at the same time minimizing spill-over energy. In practice, some spill-over is always present due to the finite size of the reflectors. On the other hand, properly modifying the feed radiation pattern may be achieved at an high cost. Therefore, the feed is normally tapered by a simple cosine function where the taper at the edge can be chosen accordingly to well know figures [3-6, 3-7]. The optimization achieved through the shaping of the reflectors is commonly adopted and it has become over the years the preferred approach for designing dual reflector antennas, where some tuning capabilities are needed in terms of antenna efficiency. ESA's 15-m antennas employ both shaped sub- and main reflectors together a feed (generally a dual S- and X-band feed) at the Cassegrain focus providing a cosine type tapering and achieving a value at the edge of the sub-reflector of around 12 dB. This value is very close to the optimum derived in [3-6]. Considering this illumination, the 15-m ESA antennas present a total efficiency of 59% at S-band and 76.9% at X-band.

There are mainly two geometrical optics procedures for dual reflector shaping. The first one has been described by W. F. Williams and C. J. Sletten respectively in [3-8], and [3-9]. It is based on the classical Cassegrain (Gregorian) geometry, and it is performed in two independent steps. In particular, the first step consists in modifying the sub-reflector to achieve a specific main reflector illumination law, while the second step deals with the modification of the main reflector, which is performed to compensate for the phase error introduced by the first step. In other words, sub and main reflectors shaping have respectively an impact on the amplitude and phase distribution of the aperture field. The main issue related to this two steps procedure is that the shaped system instead of presenting a focal point, presents a focal region, which can be more or less extended, depending on the quality of the main reflector phase correction. As a consequence, even though this algorithm may generate high performance designs, a correction of the feed position and characteristics may be required in order to optimize the overall system performance. The other procedure described hereafter is a new formulation of the most common shaping procedure employed nowadays that has been for the first time described by Dr. Victor Galindo in [3-10] and [3-11]. Contrarily to the other approach, this one generates the main and the sub-reflector contemporaneously, it does not make use of analytical surfaces as a starting point, and it generates a dual reflector system presenting a specific focal point. In practice, the new reflectors are generated from scratch, given the position and radiation characteristic on the feed, the diameters of the reflectors, and a reference point on the main reflector, such as its rim, or its vertex. This shaping is based on the following optical principles:

- conservation of energy along a ray tube (geometrical-optics approximation)
- Snell's law of reflection on both reflectors

- uniform phase and equal path length for all rays.

This procedure consists, similarly, of two steps:

1) the power emerging from the feed is required to be equal to that hitting the aperture plane according to the selected illumination law

2) Snell's law and equal path length condition are iteratively applied to obtain the points of the new reflectors.

The synthesis method is described for rotationally symmetric surfaces, thus the algorithm generates only half of the 2D profile. The procedure can be straightforwardly extended to doubly curved surfaces following the reported guidelines in the two symmetry planes.

The 15-m ESA antennas are performance oriented (shaping of both reflectors; some of them employ low temperature cryo low noise amplifiers (LNAs)), but the level of complexity achieved in order to increase the available gain is still a compromise. The Solid State Amplifiers (SSA), used in the 15-m antennas during telecommands transmission, are relatively simple machines with an available power in the range of hundreds of Watts, which don't require cooling or particular maintenance. The optimization of the performances is stressed further in the 35-m Deep Space Antennas (DSA) involving, as for instance, extremely low temperature cryo LNAs, advanced feed tapering, High Power Amplifiers (HPA), very accurate time reference (employing MASERs), very high panel accuracy, possibility of struts shaping.

3.4 Beam Wave Guide systems for the deep space

The prime mission of a deep space antenna is to receive extremely weak signals over vast interplanetary distances.
Due to the inverse relationship between the received signal power and the square of the distance between the spacecraft and the Earth, a deep space ground station antenna shall have a very high available gain.
To have an idea of the scaling in power received by a deep space antenna, consider that if a spacecraft in GEO orbit will receive one ten thousandth power that a low orbit satellite does, a spacecraft at the Moon will receive that same signal with roughly one millionth the power, a deep space mission, as for instance a spacecraft at Mars will receive the same signal with roughly three trillionths the power.
Deep-space antennas do not usually mount their feeds at the focal point of the dual reflector, but employ beam-waveguide (BWG) feed systems. BWG systems were introduced in Chapter 1. The design of BWG antennas can vary case by case, depending essentially on the dimension on the final mirror of the beam waveguide, the main mirror, the required phase illumination on the main mirror and the frequency bands desired.

3.5 Quasi-optical Design: the Gaussian Beam Approach

The classical geometrical optics approach of designing antenna mirrors follows the Mizusawa's condition, that in the case of two curved mirrors and a circularly symmetric source, state that:

- all the focal points must be arranged on a straight line
- the eccentricities of the reflectors must be equal to each other, or equal to the reciprocal of each other.

Depending on the frequency span covered by the operating bands, some feeds designed through the classical Geometrical Optics approach using Mizusawa condition may be unfeasible or unpractical, as low frequency sources require larger apertures in order to generate patterns equivalent to those generated by the high frequency ones. To cope with this problem, beam-waveguides are typically designed in two different sections: the upper part following Mizusawa's condition and the lower part mounting additional curved reflectors refocusing the beams. In the ESA deep space antennas layout, depicted in Figure 3-10 a beam-waveguide layout including additional curved reflectors, which are not respecting Mizusawa's condition, is employed. By exploiting the magnification properties of these mirrors, the narrow beam image required at the dual reflector focal point may be generated by employing a smaller size feed producing a wider beam, which is then magnified by the curved surface. In the figure, the upper beam-waveguide part (M1 to M4) is still designed applying Mizusawa's technique. It may be considered transparent to field propagation, neglecting the finite size of mirrors under geometrical optics approximation, in the sense that placing a feed in Cassegrainian focus of the antenna is exactly equivalent to placing it in the focus of M5. Mirror M5, on the other hand, is not balanced by any other curved mirrors, as seen by feeds 1 and 2, thus it is acting as a magnifying element, and, therefore allowing for reducing the size of the two feeds, and of mirrors M6, M7 (both frequency selective surfaces), and M8, by refocusing the beam emerging from FM5 into FM5'. Mirror M8 might as well be used to fulfill Mizusawa's criteria, as seen by feed 3, but it typically is not, in order to exploit its ability to allow for equipping a smaller aperture feed. In these situations, a trade-off has to be done, between the need of manufacturing smaller feeds and reflectors, and the need of reducing cross-polarization or beam squint (the beam squint phenomenon will be explained later on). The typology of beam-waveguide reported in the Figure 3-10 is therefore only partially designed through Mizusawa's approach and, due to the presence of a curved M5 and therefore to the reduced size of mirrors M6, M7, and M8, the lower beam-waveguide (green) is not designable through standard geometrical optics, as diffraction effects may become dominant. In these situations a *quasi-optics* (also known as Gaussian beams) approach is required to achieve optimal performance. The first mathematical expression of Gaussian beams derived from the solution of Maxwell's equations was given by Dr. G. Goubau and Dr. F. Schwering in 1961 [3-12]. *Quasi optics* provides an approach for dealing with those structures that cannot be analysed through geometrical optics, because of the limited size of their source or reflectors, but fails when dealing with elements too small in terms of wavelengths, where physical optics should be used. The analytical formulation of Gaussian beams in presented in Appendix A of the present chapter.

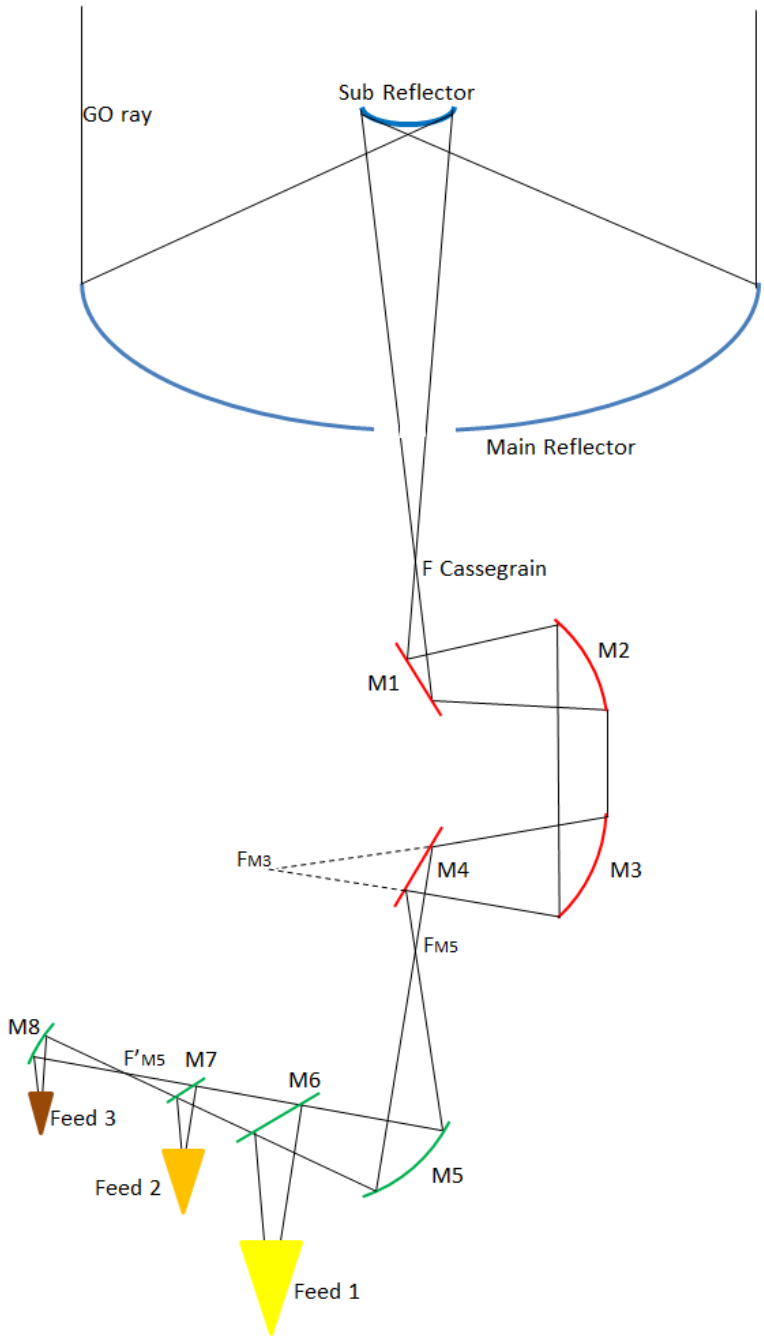

Figure 3-10: ESA DSA BWG layout with combined Mizusawa (upper red part) and *quasi-optics* (lower green part) approach

3.6 Other optimization elements

Cryogenic low noise (LNA) amplifiers, anti-deformations techniques for the reflectors panels, struts shaping are applied for lowering the system noise temperature, which is the only remaining

parameter to play with as soon as the dimension and optical magnification of the ground antenna are defined, as far as the receiving part is concerned.
By using cryogenic amplifiers, the receiver noise-temperature contribution can be small (as low as 2 to 3 K for the highest performing masers), and it then becomes imperative to minimize both the antenna and feed-system contributions. For ambient conditions, it should be noted that feed-system losses contribute to noise temperature at the rate of 7 K per 0.1-dB loss. Cryogenic LNA modern technologies are more and more closer to the feed, becoming an integrating part of the feed itself.

Modern multi band feeds employing cryogenic LNAs help also in reducing the number of FSS apt to split the beams in a BWG layout, reducing the related insertion losses (in the order of 0.1 dB corresponding to 7 K).

Surface accuracy is also an important parameter in determining the effective aperture area, as is demonstrated in Figure 3-11, which plots the reduction in gain versus root-mean-square (rms) surface error. It demonstrates that the rms surface error must be an extremely small fraction of the reflector diameter.

Surface errors fall into two main categories [3-13]:
(a) time-invariant panel mechanical manufacturing errors and panel-setting errors at the rigging angle
(b) time-varying errors induced by gravity, wind, and thermal effects.

Improvements in panel manufacturing and in panel setting using microwave holography have left gravity distortions as a function of elevation angles as the major error source in deep space antennas for higher-frequency operation. A study conducted by ESA with Vertex Antennentechnik showed that the employment of sub-frames (see Figure 3-12) for the compensation of the time varying errors can lead to an improvement of 70% on the surface rms error.

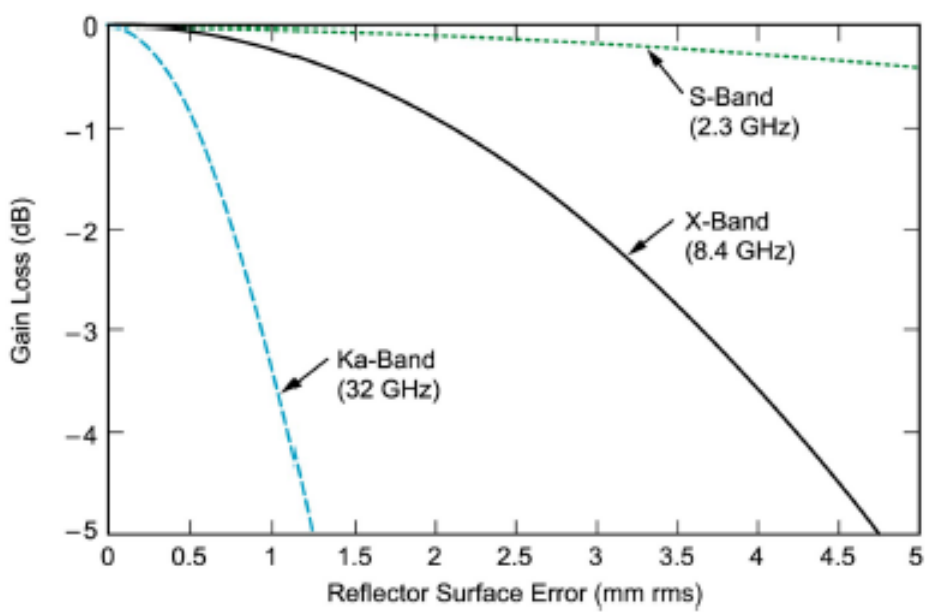

Figure 3-11: Gain loss depending on surface accuracy for the ESA frequency bands of operation

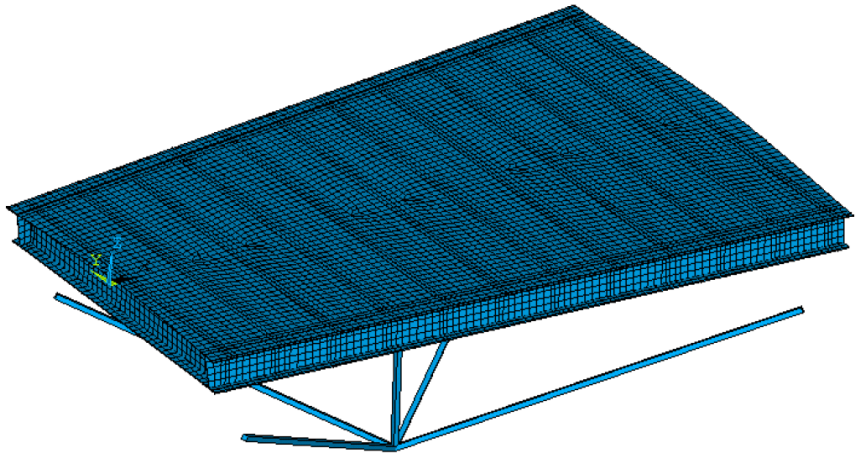

Figure 3-12: Example of a sub-frame for panels distortion compensation – FEM model

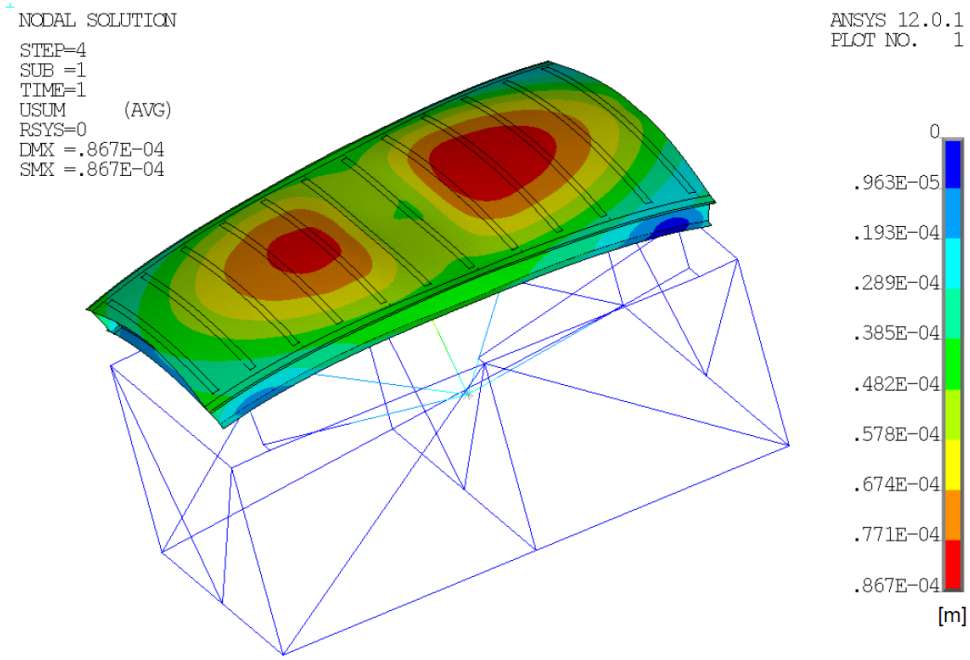

Figure 3-13: Analysis of the rms panel surface accuracy for a temperature displacement of 1 K

Other approaches for improving the antenna noise temperature (between 0.5 K to 1.5 K over the entire range of antenna elevation angles) in deep space antennas focus on struts shaping, implementing a wedge shaped shield that reduces also near-field RF exposure [3-14].

3.7 The upgrade of a BWG radio telescope into a TT&C Deep Space Antenna

3.7.1 The Sardinia Radio Telescope

The Sardinia Radio Telescope (SRT) is a fully steerable radio telescope, completed in 2012 in San Basilio, Sardinia, Italy. SRT is the third antenna of the Italian VLBI (Very Long Interferometry Baseline) network, part of the European VLBI Network (EVN) [3-15, 3-16]. It is currently operated by the Italian astrophysics institute (INAF) for radio astronomy observations and it was co-financed by the Italian Space Agency (ASI). SRT is a multiple reflector Gregorian antenna with a large main reflector (64 meters of diameter) whose surface is made of 1008 aluminium "active" panels controlled by actuators, in order to guarantee high efficiency over the very large operational band foreseen for radio astronomy (0.3 – 100 GHz). Furthermore, SRT employs a beam waveguide system which makes the antenna very versatile, allowing for multiple focal positions. The BWG system of SRT [3-17] is located below the main reflector. The BWG mirrors are distributed over the two lower floors of the so-called Elevation Equipment Room (EER) (see Figure 3-15). At the third floor of the EER, a Gregorian feed rotator (GFR) is used by INAF to position different reception feed systems in the Gregorian focus by means of rotation. The GFR is a truncated disc, to allow the optical path to be further routed downward to the BWG when reception is not intended to be performed at the Gregorian focus.

Figure 3-14: SRT during commissioning - credits to INAF

This means that the use of the Gregorian feed rotator and of the BWG system is mutually exclusive. At present, only two receivers for radio astronomy are assembled and used on the GFR: one C-band and one K-band horn. At the second floor of the EER, a rotating elliptical mirror (M3) is used to direct the optical path to the four BWG focal positions via four fixed elliptical mirrors (M4, M5, M6, M7). A C-band receiver is installed at the focus of M4 for radio astronomy operations by INAF. Moreover, the positioning of a radio astronomy receiver in the prime focus (the focus of the main parabola) of SRT is achieved by means of a movable mechanical arm, called Prime focus positioner (PFP), which is mounted aside the sub-reflector. In rest position, i.e. when the use of the antenna doesn't contemplate the reception in the prime focus, the PFP is parked. When the reception in the prime focus (instead of at the GFR level or down in the BWG) is intended, the PFP folds down below the sub-reflector, positioning, by means of translation of the supporting structure, the requested feed at the prime focus. On the PFP, a dual coaxial P-L-band feed is mounted by INAF together with two X-band feeds (one for holography). All feeds mentioned have circular apertures. Figures 3-15 and 3-16 illustrate all the elements just introduced.

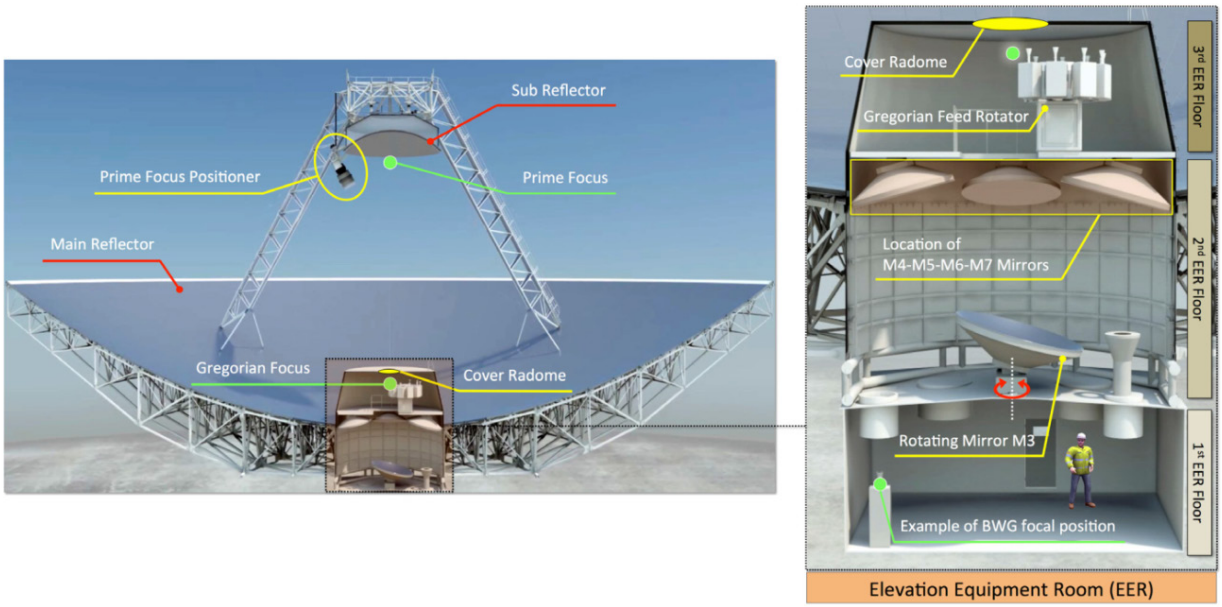

Figure 3-15: Schematic of SRT reflectors, struts, PFP and EER with the GFR (left); EER floors (right) - credits to Seiès Comunicazione & Design

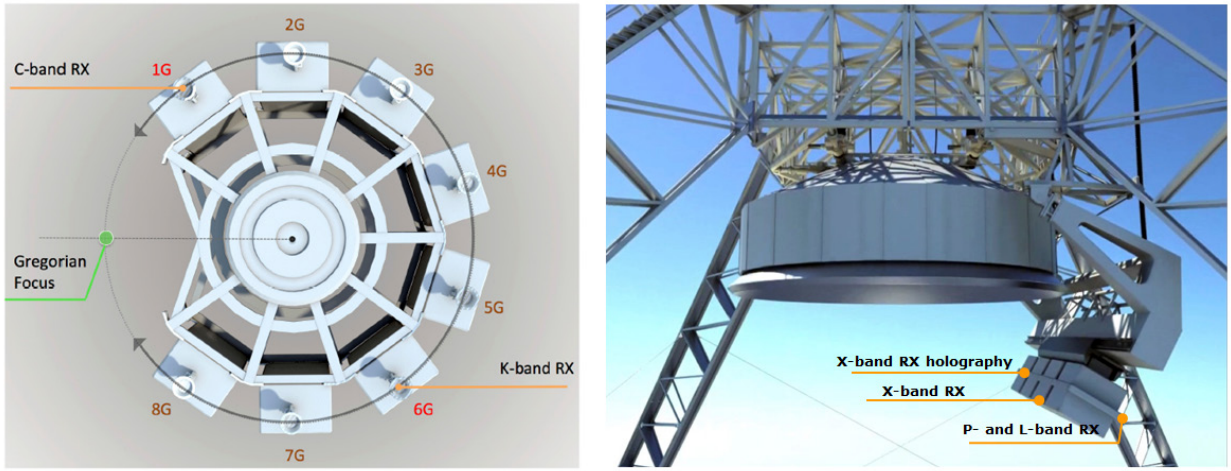

Figure 3-16: Particulars on the GFR (left) and the PFP (right) - credits to Seiès Comunicazione & Design

3.7.2 The upgrade to TT&C capabilities

Following its upgrade to TT&C capabilities, planned by the Italian Space Agency (ASI), SRT will be able to support communication to/from deep space probes, as presently performed by the deep space antennas (DSA) of the European Space Agency (ESA). The perspective would be to add SRT to the ESA's DSAs network. Among the four focal positions identified by the movement of M3, two (using M4 and M5) are dedicated to radio-astronomy observations (INAF), the remaining two (using M6 and M7) will be assigned to ASI for TT&C with space missions. Technical support was contracted by ASI to ESOC, for the *Phase 1* of the upgrade. In this phase, the technical specifications and the upgrade requirements were defined at first. The work was partially sub-contracted to the Microwave Department of the University of Pavia, who carried out most of the design of the new layout for the TT&C upgrade. The author of the present work was involved at a later stage and figured as a technical responsible at ESOC for a study which addressed design optimisation techniques, electromagnetic compatibility (EMC) and interference (EMI) analyses, as well as the evaluation of the biological hazard. As a matter of fact, in order to implement the upgrade of SRT for the TT&C, its original and present implemented design shall be enhanced. The design of the TT&C system shall take into account the possibility of supporting both planetary as well as astronomical missions. Planetary missions operates at X-band for transmission (TX) (7.145 – 7.235 GHz) and for reception (RX) (8.025 – 8.4 GHz) as well as at Ka-TX (34.2 - 34.7 GHz) and Ka-RX (31.8 - 32.3 GHz). Astronomical missions may use a K-band reception only capability (25.5 - 27 GHz) together with X-band (8.4 – 8.5 GHz). The upgrade to TT&C will make SRT one of the most versatile antennas in the world in terms of type of operations supported and related science applications.

3.7.3 SRT TT&C proposed optical layout

The feed system for the TT&C upgrade proposed by the University of Pavia is based on corrugated horns [3-18]. A multiband feed horn operating simultaneously in TX and RX at X-band and only for reception at Ka-band is proposed together with a single-band horn working at Ka-band for transmission. Both feeds are provided for planetary applications. On the other side, astronomical operations will be supported by a multiband horn working in TX and RX at X-band and by a single band horn working at K-band only for reception, to be physically interchanged when required. Figure 3-17 depicts the proposed layout. The separation of the Ka-TX and Ka-RX bands is achieved by means of dichroic mirrors [3-19, 3-20], in particular the dichroic mirror M8, and exploiting the possibility to simultaneously rotate M10 and M11 mirrors. The separation of the Ka-band is proposed to overcome the beam squint problem, which will be introduced during this dissertation. The design of the SRT BWG architecture has been developed under the assumptions of the Gaussian Beam theory as it represents a feasible compromise between computational time and accuracy gathered by geometrical and physical optics (PO) methods [3-21]. The analytical formulation of the Gaussian beam theory, introduced in the previous paragraphs, is reported in the Appendix A. According to this formulation, the radiation beam is defined as an ideal Gaussian intensity profile (fundamental zero-order mode) propagating along the optical axis [3-22]. In this framework, the main aspect that remarks the effectiveness of the Gaussian Beam theory is the negligible computational time required. Due to this, it is possible to fashion additional optimization tools in order to achieve the best design parameters for all the specified frequency bands. The optimization routine that has been developed by the University of Pavia and ESOC takes into account various parameters, i.e., position, inclination, geometry of the BWG mirrors and distances between each other, feed horn dimensions and location.

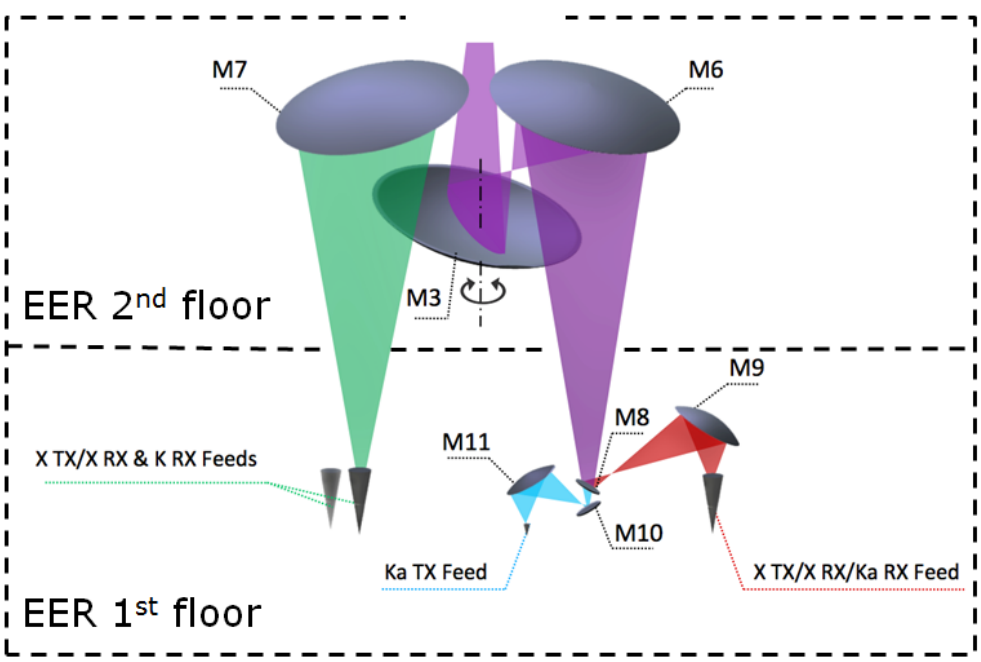

Figure 3-17: Proposed layout for the TT&C upgrade of SRT with G.O. ray tracing. - credits to University of Pavia

In the synthesis process, two are the principal aspects that have to be carefully considered to meet the system requirements: first of all, the bulky BWG architecture shall be designed to fit the EER room and, second, an edge taper value of 12 dB shall be maintained on the sub-reflector (the same that had been employed for its shaping in the original design) in order to reasonably limit both noise contributions and side-lobe levels. The first goal of the optimization process is to maximize the antenna illumination efficiency by approximating the beam aperture and the beam radius of curvature obtained on the sub-reflector, respectively, to the sub-reflector diameter and to the distance between its vertex and the Gregorian focus. In this way, the optimum illumination efficiency is retrieved for all operating frequency bands in terms of amplitude and phase. The next step is to define the rim contour of each BWG mirror, which has been arranged by keeping the edge taper around 16 dB for preventing excessive spill-over losses and for hindrance reasons in the EER room. The corrugated horns design refinements and the final antenna verifications have been carried out by employing the optimized results of the Gaussian analysis in TICRA's commercial tools CHAMP and GRASP. In doing so, the overall antenna performance has been retrieved using the PO method, gathering relevant data like antenna gain (including illumination, phase, blockage and spill-over contributions) and the relative radiation patterns for each operating frequency band. These results are reported in Figure 3-18.

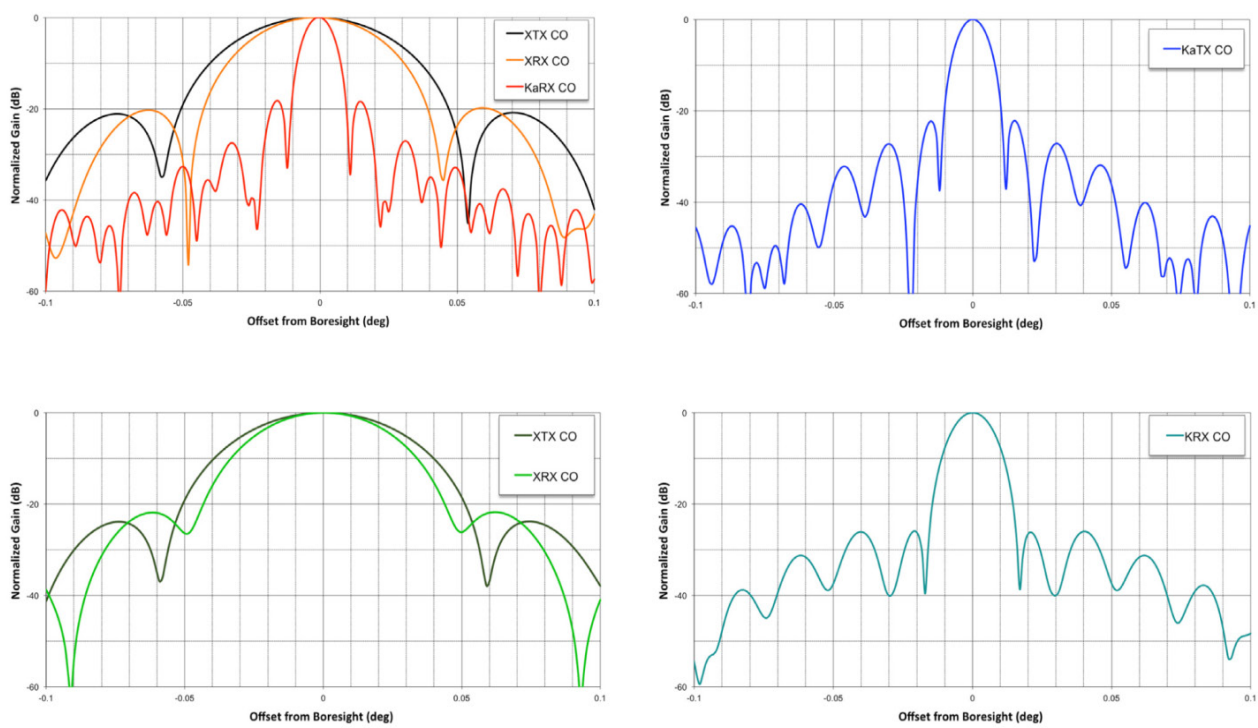

Figure 3-18: Radiation Patterns of the SRT for frequency bands supporting planetary missions (top) and astronomic missions (bottom) - credits to University of Pavia

3.7.4 The beam squint

Precise tracking of a distant probes implies the establishment of a two way link between the ground station and the spacecraft. In this configuration the signal transmitted from the ground station is received by the spacecraft, turned-around (after demodulation) and retransmitted back to earth. During the signal round-trip light time (RTLT), the spacecraft moves in the plane of the sky as seen from the Earth. Therefore, from the ground station, the targets for the uplink and downlink signals are seen spaced by an angular offset (i.e. beam squint). Such offset is directly proportional to the transverse component of the spacecraft velocity. Such phenomenon is known as RX-TX beam squint effect. If the distance between the spacecraft and the Earth is extremely large (i.e. large RTLT) and the spacecraft is in an orbital phase in which the transverse component of its velocity is maximum (i.e. superior solar conjunction), this angular squint becomes considerable. In such cases the RX-TX beam squint converts directly into a significant gain loss, which can severely impact the antenna performance. The described situation is shown in Figure 3-19, where an angular separation is forced between the TX and RX beams. Recent observations from all ESA 35-m deep space antennas derived that the maximum beam squint angle evaluated on interplanetary missions may reach up to 40 mdeg (e.g., MESSENGER missions nearby Mercury during a superior solar conjunction [3-23]). As it is common practice to determine optimized orbit predictions for reception, the beam squint correction is usually applied to the transmission path. Figure 3-19 reports an example of the SRT radiation pattern at Ka-band with no squint correction capability: at 40 mdeg from the nominal boresight direction, it is remarked that a considerable and unpredictable gain loss would occur in case of a real-time full-duplex communication is required.

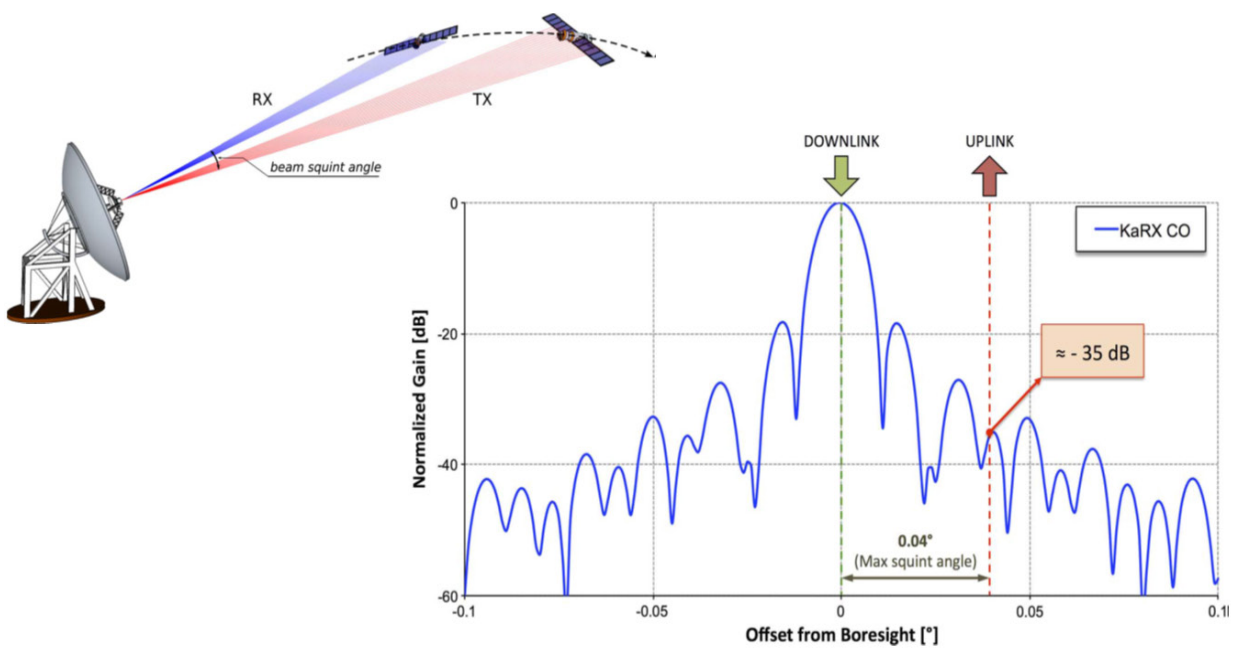

Figure 3-19: Beam squint representation and simulated SRT radiation pattern in Ka RX band – credits to University of Pavia

A system able to independently steer the RX and TX beams is needed. For this reason, the lower BWG architecture of the SRT has been specifically designed for separating Ka-TX and Ka-RX. The geometry reported in Figure 3-17 was proposed and has been used for the simulations described in this document. As can be noticed in Figure 3-17, the Ka-TX path is separated from the rest to allow beam squint compensation by means of moving mirrors M10 and M11. Further solutions are currently being investigated to isolate also the X-TX feed in order to apply as well a beam squint compensation. This would be in principle as well possible thanks to the high versatility grant by the BWG layout. Anyhow, due to its narrower beamwidth, the Ka-band is more critical in terms of beam squint, but, for a 64-m large aperture, as for SRT, beam squint also becomes a problem for deep space probes in X-band. For instance, ESA's 35 meters DSAs do not need beam squint compensation in X-band. Displacing the mirrors M10 and M11 relies on the use of accurate servo motion controllers in such a way to steer the antenna main lobe in transmission along the appropriate squint angle without shifting the RX beam from the nominal pointing direction. The most binding constraint in this process is represented by the need for keeping the antenna gain loss as low as possible: it is evident that, if the optical geometry of the BWG is modified from the one obtained from the Gaussian analysis at Ka-TX band, the optimum beam amplitude and phase conditions on the sub-reflector will not be satisfied any longer and this obviously turns into lower antenna illumination efficiency. Preliminary studies performed on the SRT demonstrated that movement strategies involving only one BWG element are rather unreliable if compared with double mirror tilting techniques, which can provide much higher beam steering sensitivity and less severe illumination efficiency reduction. The most straightforward movement investigated was a rotation of M10 and M11 along their X- and Z- axis, as shown in Figure 3-20. This choice has been preferred in spite of other options as it ensures a minor hindrance in the first floor of the EER and permits to install a lower cost servo system mechanism. The standard approach for the beam squint correction can be defined as a single-step "bottom-up" analysis: the antenna is simulated from the transmitting feed horn to the main dish throughout the entire BWG system by means of the PO method. However, a single bottom-up analysis requires a heavy computational effort (some hours) to compute a large antenna system such as the SRT and iterative simulations are needed for each mirror displacement to retrieve the antenna gain with the relative beam squint.

3.7.5 Beam squint compensation

A novel technique based on a top-down approach has been developed by the University of Pavia and ESOC in order to overcome the main drawbacks of the standard bottom-up approach previously described. The basic idea of this method is to illuminate the antenna main dish with a plane wave impinging from a given direction, corresponding to the desired beam squint angle, and to calculate the field on a fictitious planar grid located at a convenient level along the BWG propagation path (see Figure 3-20). On the other side, the field radiated by the feed horn is calculated on the same fictitious planar grid trying to match as accurately as possible the footprint of the plane wave by rotating both mirrors M10 and M11. This idea has been already employed in the past with the aim of performing a similar study for the beam squint compensation on an ESA ground station antenna at Ka-band [3-24]. Nevertheless, due to the lack of an automatic algorithm for the field-matching procedure, only a limited number of mapping tests were simulated in this case and the achievement of the best configuration was not accurately guaranteed. The main advantage of that novel approach lies in the minimization of the processing time for achieving the optimum solution in all beam squint cases. In fact, the PO analysis of the main and sub-reflectors represents the most time-demanding simulation part, which, indeed, does not change for the beam squint correction and so it can be performed once for each plane wave inclination. On the contrary, the beam radiated from the feed source is calculated on the planar grid in a very short computing time. As a consequence, it has been possible to fashion an iterative MATLAB routine that runs in sequence several (thousands) bottom-up simulations in a few minutes, assuming all possible displacements of M10 and

M11 defined within an arbitrary rotation range and resolution (project specification: rotation range of 6 deg, movement resolution of 0.1 deg around both X and Y axes). The program also manages to speed up even further the procedure by automatically identifying the most effective mirror-tilting strategy to appropriately overlap the field configurations on the fictitious grid. The optimum matching condition is found by minimizing the $|\Delta_{amp} + \Delta_{phase}|$ factor, where:

$$\Delta_{amp} = \left|\overline{x}_{PW}^{amp} - \overline{x}_{feed}^{amp}\right|$$
$$\Delta_{phase} = \left|\overline{x}_{PW}^{phase} - \overline{x}_{feed}^{phase}\right|$$

In these expressions, $\overline{x}_{PW}^{amp}$, $\overline{x}_{feed}^{amp}$, $\overline{x}_{PW}^{phase}$ and $\overline{x}_{feed}^{phase}$ are the Cartesian coordinates where the maximum for the magnitude and the phase of the field occurs, respectively for the plane wave and feed analyses. Thus, Δ_{amp} and Δ_{phase} represent the spatial offsets between the peak coordinates of the plane wave and feed analysis with respect to the amplitude and phase, respectively. Once optimum field matching is achieved in terms of amplitude and phase on the fictitious grid, a single overall bottom-up analysis has to be performed to confirm the beam squint value and to assess the gain loss. The top-down approach has been repeated for different beam squint angles, in particular ± 10, ± 20, ± 30 and ± 40 mdeg. In doing so, it has been possible to obtain the analytical law that shall be applied to the servo actuators for the optimum beam squint correction. Figure 3-21 summarises these results for elevation and cross-elevation plane cuts respectively, both exhibiting a good accuracy for any squint. It is noted that, for a maximum beam squint angle of -40 mdeg, the worst gain degradation is below 0.8 dB, which is to be considered rather compatible with the future planetary missions requirements. It is also important to remark that there a linear proportion is verified between the beam squint and the rotation angles of M10 and M11, which will help when implementing the servo-mechanism moving algorithm for the beam squint correction.

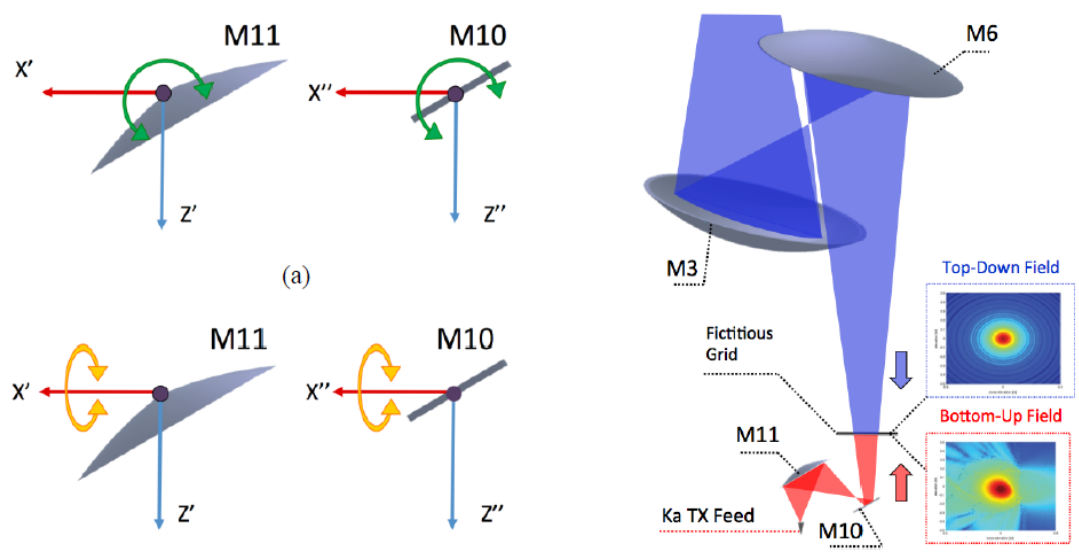

Figure 3-20: Rotation of mirrors M10 and M11 around their the Y-axis and X-axis (left).Field mapping method for the top-down approach (right) - credits to University of Pavia

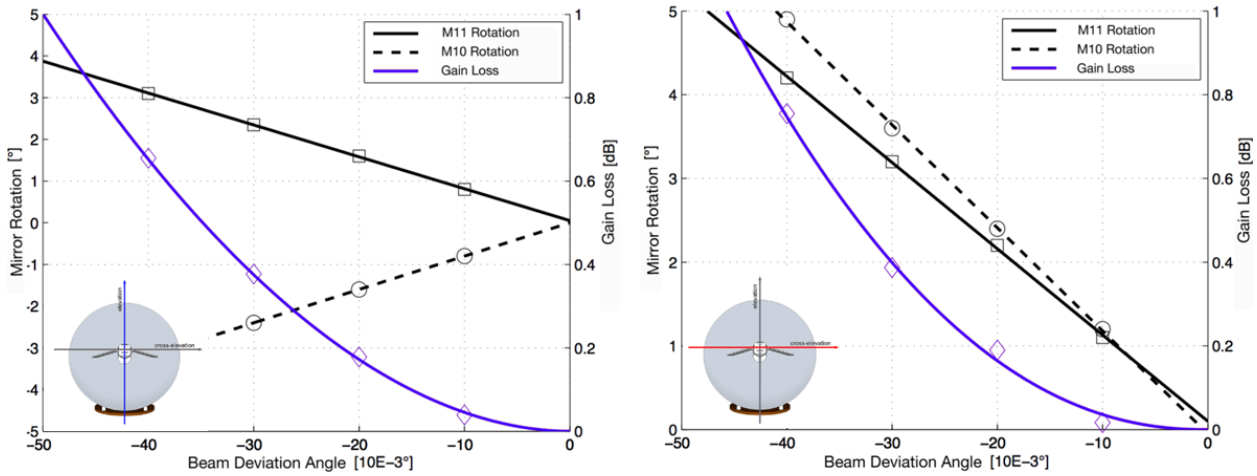

Figure 3-21: Retrieved gain loss for negative beam squint angles along the elevation plane cut (left) and the cross elevation plane cut (right) - credits to University of Pavia

3.7.6 EMC, EMI and Hazards

The future upgrade of SRT will make the radio astronomers, receiving only, capabilities, coexist with TT&C equipment, thus including transmitting equipment. Moreover, the high power of transmission of SRT (at present up to 5 KW are foreseen), together with the high gain provided by the 64-m antenna aperture (EIRP up to 107 dBW in X-band) will generate questions on the sustainability of the upgraded system. Consequently, an electromagnetic compatibility (EMC) study has been performed with reference to the interior and the exterior of the antenna structure. Using the same simulation aids, an electromagnetic interference (EMI) analysis is carried out with respect to the main auxiliary ground station existing equipment and in the event of overflying aircrafts. The biological hazard is finally evaluated on human beings. This dissertation is aiming at providing a complete EMC analysis related to the power collected by the INAF receivers previously introduced, when the antenna will be used in TT&C mode by ASI, thus transmitting in X- and Ka-band. The foreseen transmitted powers are 5kW and 500 W, respectively for X- and Ka-band. The simulations have been performed using GRASP by TICRA. For some post-processing MATLAB is used. The whole existing antenna layout and the foreseen TX layout have been geometrically modelled (see Figures 3-22, 3-23, 3-24) with their true dimensions foreseen by the optical TT&C layout just introduced. Both the GFR and the PFP were reproduced and considered in their rest position, since an uplink mode has been simulated. The contributions of the EER walls have been considered along the direction of the electromagnetic beams (i.e. only floors and ceiling were accounted). Second order effects (multipath, minor objects scattering) were neglected in order to have manageable simulation times. The influence of the antenna struts has been as well neglected, because very small impact is expected, having the struts a very small cross-section compared to whole antenna aperture area. Both the sub-reflector and the main-reflector consider their true shaping. The simulations were done at the lowest foreseen TX frequencies of the allocated band for deep space missions support. To the lowest frequencies is theoretically linked the widest distribution of power along the propagation paths. All reflections are considered from perfect metallic surfaces.

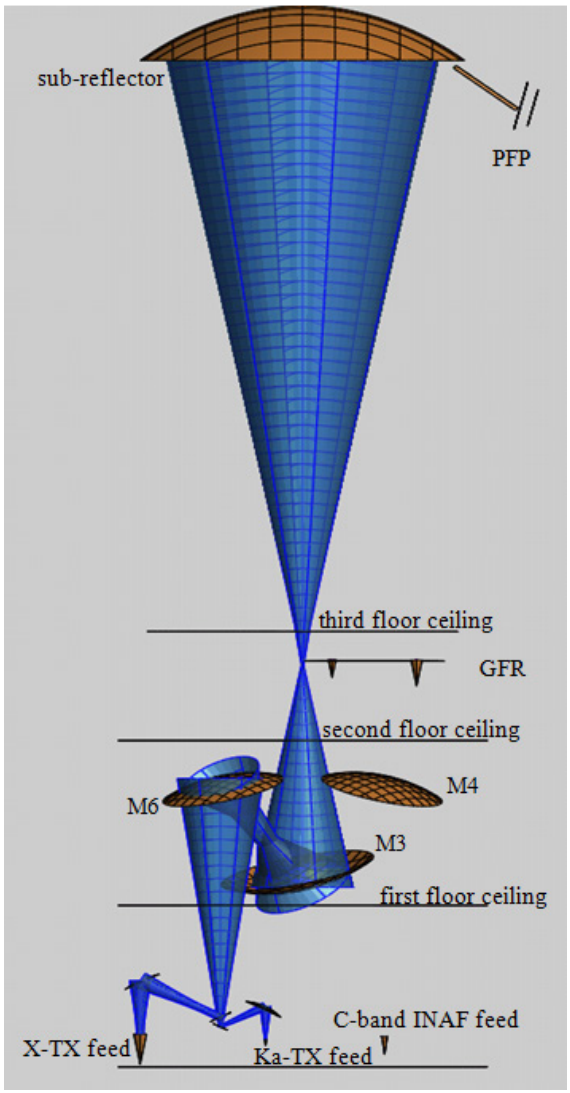

Figure 3-22: GRASP geometrical model of SRT (main reflector hidden) with uplink in X- and Ka-band represented by Gaussian beams

The simulations are performed on the assumption of unitary coupling between all frequencies in TX mode and all frequencies in INAF mode. Although being this a rough approximation, it is considered valid since the uplink frequencies used are in general higher than the INAF ones (propagation of higher order modes). This was verified via CST (Computer Simulation Technology), which showed that, the consideration of higher order modes could lead, in some cases, to coupling factors close to one. With these hypotheses, representing the worst case scenario, the EMC analyses were performed, according to the following. A Gaussian beam excitation was simulated at the foreseen X- and Ka-band feeds locations and propagated along the foreseen BWG paths. The fields were evaluated using the Physical Optics (PO) method. The auto-convergence tool was used to aid the PO points calculation needed on the mirrors for a proper electromagnetic characterization. The power spread along the BWG and outside the main reflector was computed and ultimately evaluated on test surfaces, corresponding to all INAF RX feed circular apertures. All contributes from the reflecting surfaces were taken into account with a first order approximation (no multipath considered). For instance, to compute the power impinging the feeds accommodated on the GFR (see Figure 3-22), the following contributes were considered:

- Power reflected from the third floor ceiling
- Power scattered by the GFR structure itself
- Power entering back to the EER from the reflection on the sub-reflector
- Return loss of the radome positioned at the third floor ceiling hole to avoid rain and moisture entering the EER

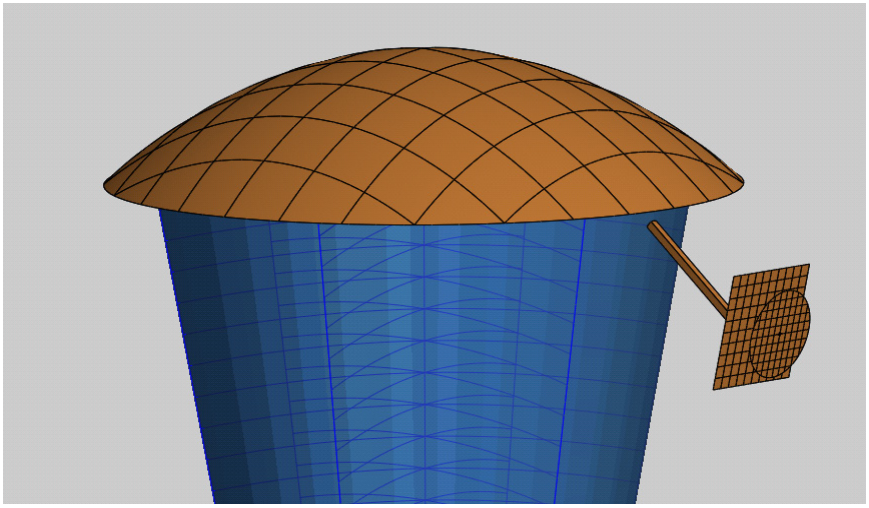

Figure 3-23: Zoom on the GRASP model of the sub-reflector with the PFP aside

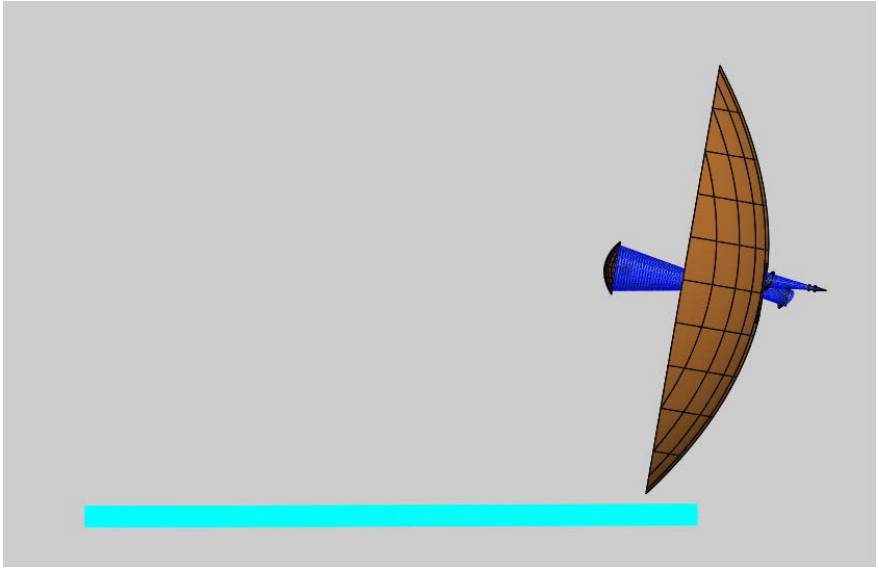

Figure 3-24: Example of an evaluation surface at ground for EMI analysis with SRT elevation of 10°. The main reflector is here shown

Figure 3-24 shows one of the evaluation surfaces defined for the EMI analysis carried out for the outdoor auxiliary electronic equipment. Similar surfaces were defined for the EMI study with regard to the aircrafts and for the evaluation of the biological hazard on human beings.

The applicable regulations to be fulfilled are:

- [3-25] applicable for EMI on electronic equipment; 1V/m (equivalent to 0.00265 W/m²) is used as reference although valid up to 2.7 GHz. The regulation does not define a limit for our frequencies of interest.
- The EMI limit applicable in Europe to civilian airplanes certified before 1986 is 20 V/m (1 W/m²) for the instantaneous average field in continuous wave mode transmission [3-26]. According to the ECC Report 66 [3-27], 40% of the flying airplanes in Europe belonged to this category in 2004. The actual estimation is 10%.
- [3-28] is applicable for the human beings. The limit of 40 V/m (4.24 W/m²) is considered.

3.7.6.1 EMC results

Some of the most significant plots obtained are presented hereafter for the X-band uplink, which, being for design specifications ten times more powerful than the Ka-band transmission, is potentially more harmful. Moreover, as mentioned, higher frequencies confine better the power transported by the electromagnetic propagation. Figure 3-25 shows the power flux density on the GFR, as calculated by GRASP and post processed by MATLAB. In the figure, the positions occupied by the radio-astronomers feeds are highlighted. Figure 3-26 shows the power flux density on the C-band feed located in the first floor of the EER, while Figure 3-27 depicts it on the P- and L-band feeds apertures. All the EMC results are summarised in Table 3-1 (X-band) and Table 3-2 (Ka-band).

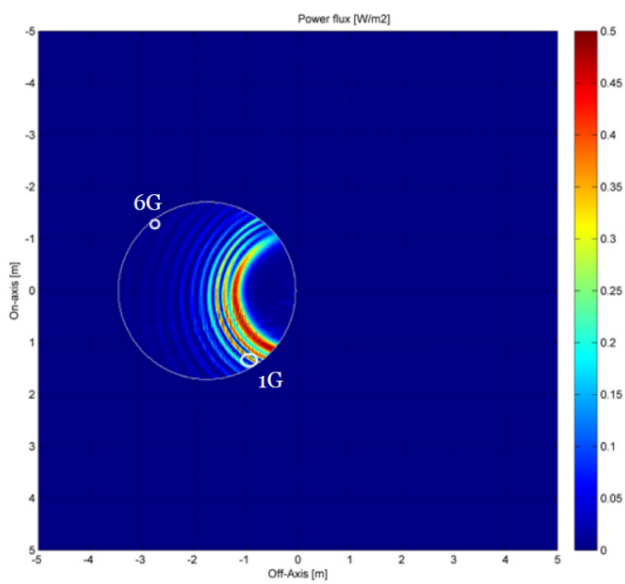

Figure 3-25: Simulated power flux density on the GFR with locations of the INAF installed feeds highlighted (1G: C-band feed; 6G: K-band feed)

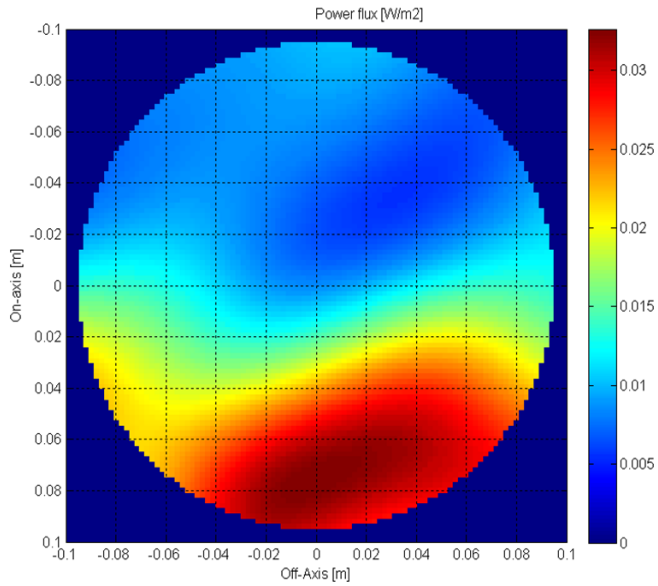

Figure 3-26: Simulated power flux density on the INAF C-band feed in the first floor of the EER

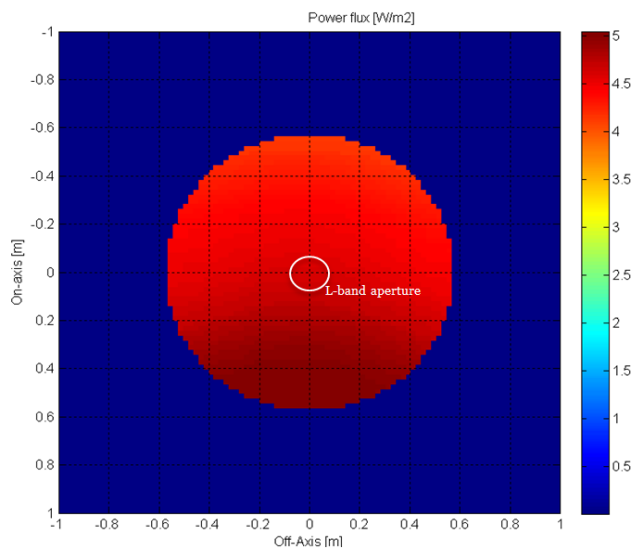

Figure 3-27: Simulated power flux density on the multi-band feed mounted on the PFP (P- and L- band apertures shown; X-band aperture not shown for clarity of the image)

TABLE 3-1: EMC results on existing receivers for X-band TX (5 KW)

INAF Receiver Name	Limit P_{MAX} LNA_S	$P_{MAX\ simulated}$
	[mW]	[mW]
1G on GFR (C-band)	50	5.67
6G on GFR (K-band)	50	0.037
P-band on PFP	50	5000
L-band on PFP	50	109.31
X-band on PFP	50	5.31
C-band BWG	50	Final value hardly predictable due to mirrors spill-over and multi reflections

Table 3-2: EMC results on existing receivers for Ka-band TX (500 W)

INAF Receiver Name	Limit P_{MAX} LNA_S	$P_{MAX\ simulated}$
	[mW]	[mW]
1G on GFR (C-band)	50	0.090
6G on GFR (K-band)	50	0.0005
P-band on PFP	50	1017.16
L-band on PFP	50	24.06
X-band on PFP	50	1.011
C-band BWG	50	0.1

The maximum power simulated is derived from the integration on each RX feed aperture of the power flux density calculated by GRASP. The limit of 50 mW indicated corresponds to the damage level of the receiver at the LNAs input, as communicated by INAF. EMC issues are clearly identified on the PFP, both for X- and Ka-band transmission. This result was somehow expected, as the PFP is within the radiation cone of the main reflector. Dedicated countermeasures have to be applied. The proposed solution is twofold:

- A mechanically movable screen which should be able to protect the INAF aperture from direct radiation of the main reflector in TT&C TX mode, being the PFP in rest position. The screen must not degrade the radio astronomers performances.
- The installation, covering the INAF PFP aperture, of a frequency selective surface (FSS) being able of (almost completely) reflecting the X- and Ka-band and almost transparent for L- and P-band. Simulations showed, in fact, that the X-band feeds on the PFP are safe and no intervention is needed.

From the procedure applied in the present study it is straightforward to derive the necessary rejection factors needed to safeguard the LNAs. This is reported in the following table.

Table 3-3: Rejection factor needed with a FSS with respect to TX TT&C frequencies and P- and L-band INAF feeds at PFP

TT&C Frequency	TT&C TX Power	INAF Receiver Name	Limit P_{MAX} LNA_S	$P_{MAX\ simulated}$	Needed rejection
[GHz]	[kW]		[mW]	[mW]	
7.145	5	P-band on PFP	50	5000	21 dB
7.145	5	L-band on PFP	50	109.31	5 dB
34.2	0.5	P-band on PFP	50	1017.16	14 dB
34.2	0.5	L-band on PFP	50	24.06	0 dB

The eventual choice of such a device should be carefully performed in collaboration with INAF in order not to impact the performances in radio astronomy mode.

Moreover, with regard to the C-band feed located in the EER first floor, although a first order simulation didn't result in any particular EMC warning (see Figure 3-26), the information provided by GRASP about the total radiation spilled-over from the BWG mirrors may suggest for further investigations in X-band. The power impinging the C-band aperture has been computed accounting all the contributes coming from the mirrors and the ceiling of the floor. But, overall, the indication of the power which spills over the BWG mirrors results quite significant at the first and at the second floors. In those rooms, several optical reflections are performed and the beams are not focused (as in the third floor) and therefore multi-reflection of the overall power spilled-over may become significant also on a narrow feed aperture. Although one could think that this may be improved by an optimisation of the BWG layout for the uplink part, it can be shown that the optical layout proposed results from best performance analyses in terms of antenna efficiency, which aim at having the best illumination over the two main reflectors. It shall be also considered that some of the optical part is common to X- and Ka-band uplinks, such that a compromise had to be found to cope with both bands.

Finally, Figure 3-28 highlights that the impact of the beam squint compensation can be considered negligible as far as the EMC impact is concerned. In Figure 3-28 (image on the right) mirrors M10 and M11 are properly rotated in order to minimize the beam squint effect at 40 mdeg according to Figure 3-20. The evaluation of the field is performed in this case at the third floor ceiling, which is one of the most representative location, where the beam is very confined and any blurring of the field footprint results more visible. Moreover, any notable significant distortion of the field beam at such level would impact on the power received both in the EER (especially at the GFR) and on the PFP.

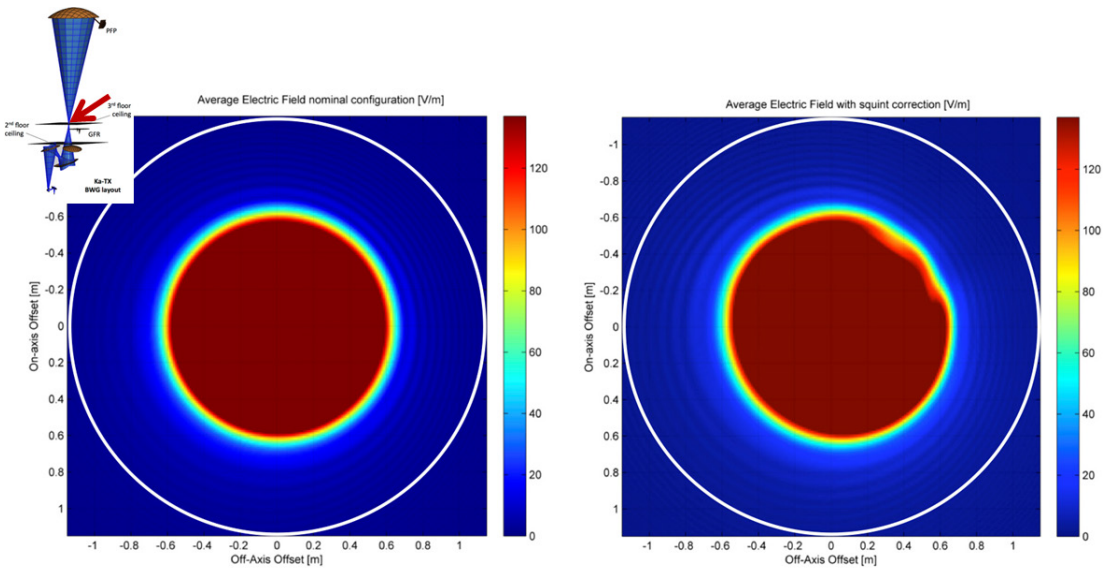

Figure 3-28: Field distributions at the second floor ceiling level in the nominal configuration (left) and in the corrected configuration for beam squint correction (right) with the appropriate rotations of M10 and M11 to achieve 40 mdeg squint. In white, the contour of third floor ceiling.

3.7.6.2 EMI results for the electronic equipment

The information on the spill-over on the BWG reflectors has been used as well for the EMI evaluation on the indoor auxiliary electronic equipment (Tables 3-4 and 3-5). The values derived inside the whole EER can be taken into account also for evaluating the safety for the working personnel, in order to eventually avoid the presence of any person inside the EER when the antenna is transmitting.

Table 3-4: EMI for the EER auxiliary equipment - X-band TX (5 kW)

EER Location	Total Power dissipated (simulation) [W]
Third floor	2
Second floor	318.5
First floor	84

Table 3-5: EMI for the EER auxiliary equipment - Ka-band TX (500 W)

EER Location	Total Power dissipated (simulation) [W]
Third floor	3
Second floor	17
First floor	2

With respect to the regulatory limit reported above (0.00265 W/m²), it shall be noted that this is valid up to 2.7 GHz, as commercial microprocessors for electronic equipment normally work below such rate. Moreover, the analysis provided the total power spread in the room, but a local real evaluation of the field on specific areas becomes computationally very demanding due to multi-reflections. The immediate outcome of the EMI study inside the EER is the suggestion of shrouding the uplink part at the first floor and installing any auxiliary equipment outside the shroud, as well as avoiding the installation of auxiliary

electronic equipment in the second floor and forbid the entrance of working personnel at the second floor when the antenna is in uplink.

In Figure 3-29, the radiated average electric field is shown on an evaluation surface of 1000x335 meters for a 10° elevation X-band uplink of SRT (minimum elevation allowed for deep space transmissions).

The spill-over from the two main reflectors is evident and it is the only source of concern with regard to outdoor EMI issues at ground. The spill-over from the main reflector causes some unwanted radiation just below its lower edge (in the case of 10° elevation at around 18 meters distance at ground from the centre of the main reflector). Similarly, the spill-over from the sub-reflector causes some radiation at ground at a farther distance (see Figure 3-29 and 3-31). At the lowest elevation, both contributes are maximal at ground. The average electric field obtained at ground is quite low with confined maxima (up to 3 V/m) and the interference with the outdoor electronic equipment is considered unlikely, including INAF devices (a RFI monitoring systems and a radiometer). As mentioned, the limit defined in [3-25] is considered only as a reference, since valid up to 2.7 GHz. Figures 3-30 and 3-31 show a quantitative comparison, between the electric field at ground caused by the uplink of SRT at minimum elevation and the one generated by a mobile phone during a call.

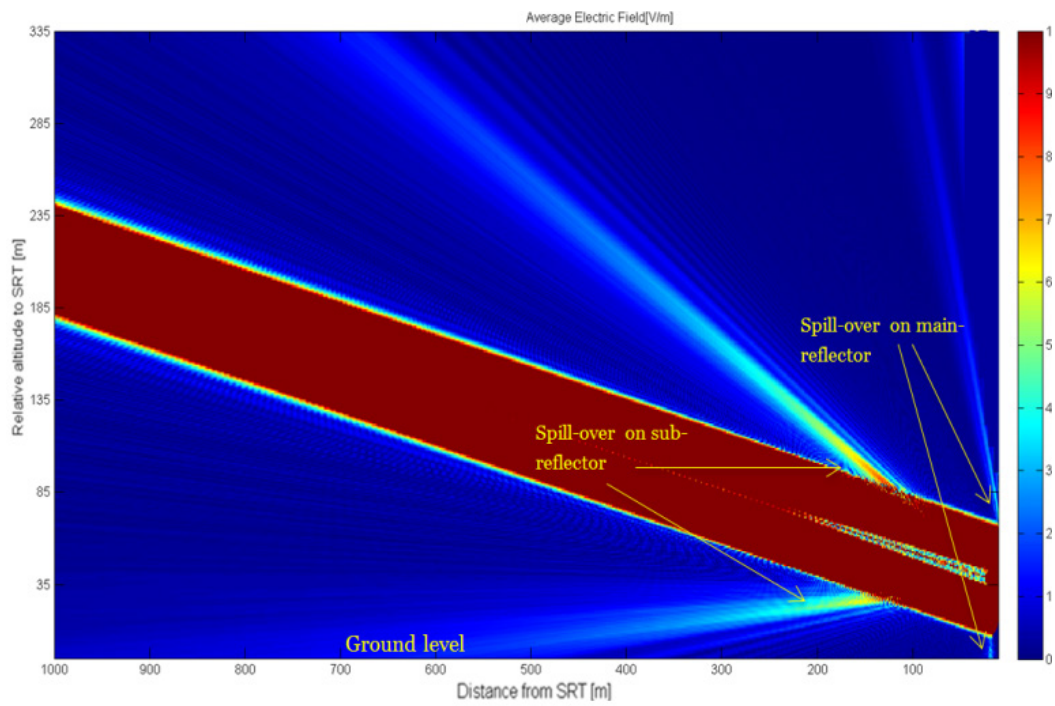

Figure 3-29: Simulated average electric field radiated in the near field of SRT

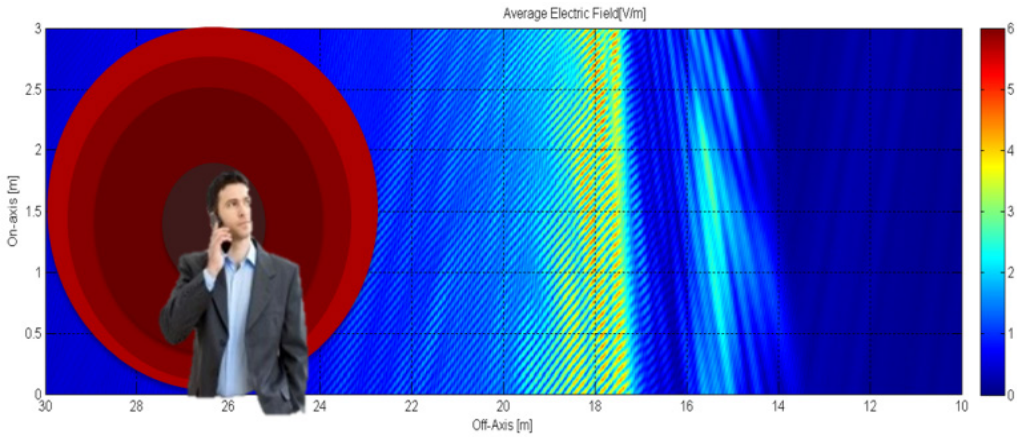

Figure 3-30: Simulated X-band average electric field spilled-over from the main reflector at ground at 10° elevation for a short evaluation surface. Quantitative comparison with electric field radiated from a mobile phone in conversation

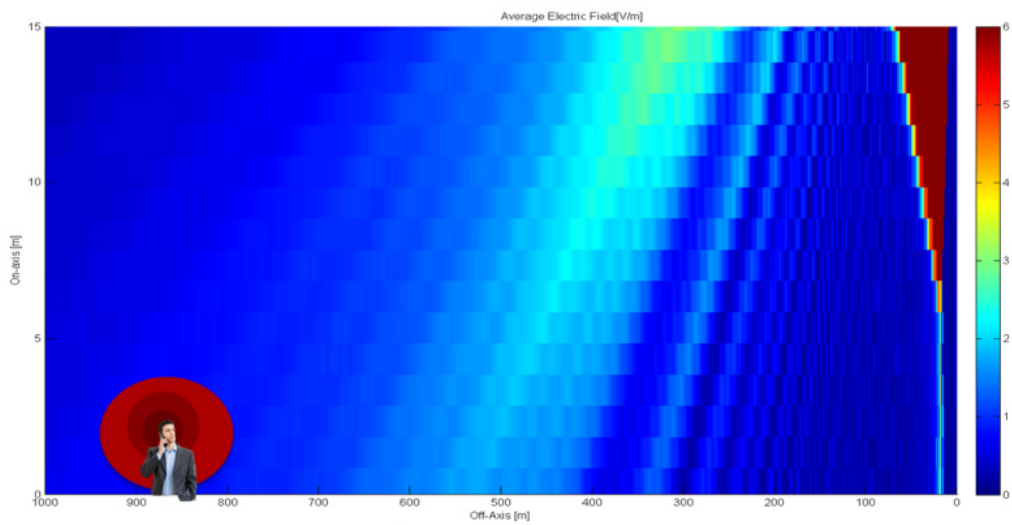

Figure 3-31: Simulated X-band average electric field spilled-over from the sub- reflector at ground at 10° elevation for a medium range evaluation surface. Quantitative comparison with electric field radiated from a mobile phone in conversation.

3.7.6.3 EMI results for the aircrafts and the biological hazard

In Figure 3-32, the average electric field is evaluated on a boresight surface at 90° elevation up to far field distances for X-band uplink with 5 kW. The 20 V/m limit for aircrafts is highlighted, together with the 40 V/m limit for the hazard on human beings. A closer look along the boresight line in the same uplink conditions (Figures 3-33 and 3-34), shows how the limit is overcome for normal aircrafts altitudes (up to 15 Km), significantly for X-band and slightly for Ka-band. Figure 3-33 and 3-34 clearly shows that the transmission option foreseen for SRT is not compliant with the Italian regulations concerning aircraft RF equipment safety. In order to have the permission for transmitting in Sardinia, some solutions have to be implemented. An approach aimed at reducing or switching off the transmitted power if a flying aircraft is detected shall be considered. Employing aircrafts detection tools (a dedicated active radar or a virtual radar box [3-29]), the

emission could be immediately inhibited or, in alternative, a system controlling the transmission amplifiers could be implemented to allow transmission with reduced power.

As a remark, the authors would like to underline, that, for example, considering the equivalent regulations valid for the U.S. (150 V/m and 170 V/m, respectively), both X- and Ka-band uplink conditions for SRT would be totally within the regulations.

From the several analyses performed and considering a 40 V/m limit according to [3-28], the biological hazard on human beings has to be considered within the normative specifications for all the locations at ground and in general when outside the cone of transmission of SRT (see Figure 3-29). The safe condition at ground is always guaranteed considering a 10° minimum elevation transmission and the fact that there aren't mountains where humans can station in the nearby of the radio telescope. As shown, spill-over phenomena have a minor impact. An hazard is potentially present for a human being only in X-band TX if inside an overflying airplane (see Figure 3-32). In this case the potential screening provided by the aircraft itself shall be evaluated. Nevertheless, this condition shall not be allowed by the even more stringent requirement on the EMI for the aircrafts instrumentation, as just discussed.

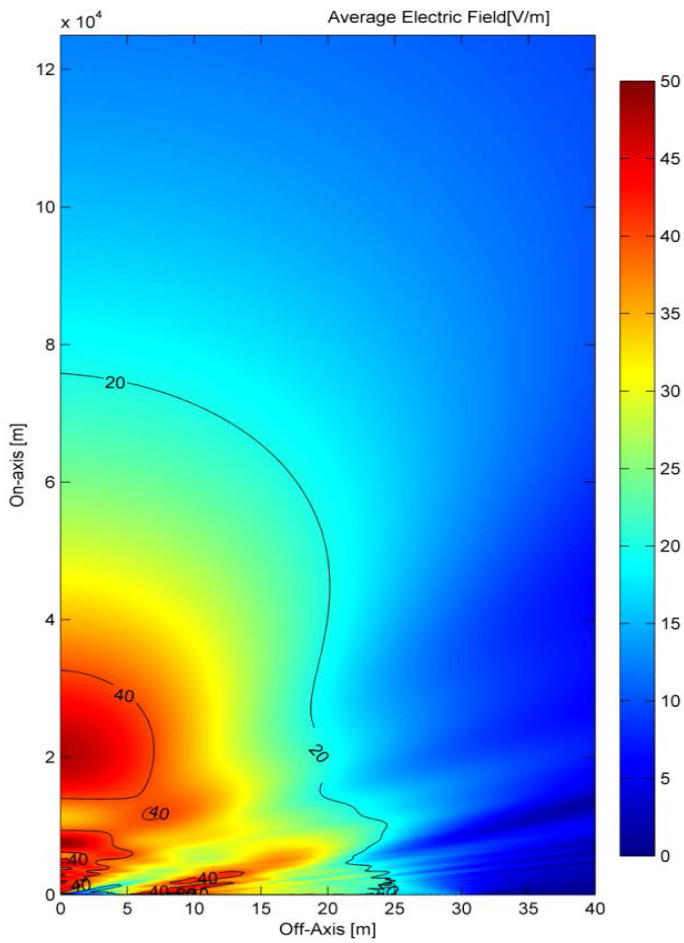

Figure 3-32: Simulated X-band average electric far field at 90° elevation on the boresight evaluation surface with limits valid for aircrafts and human beings.

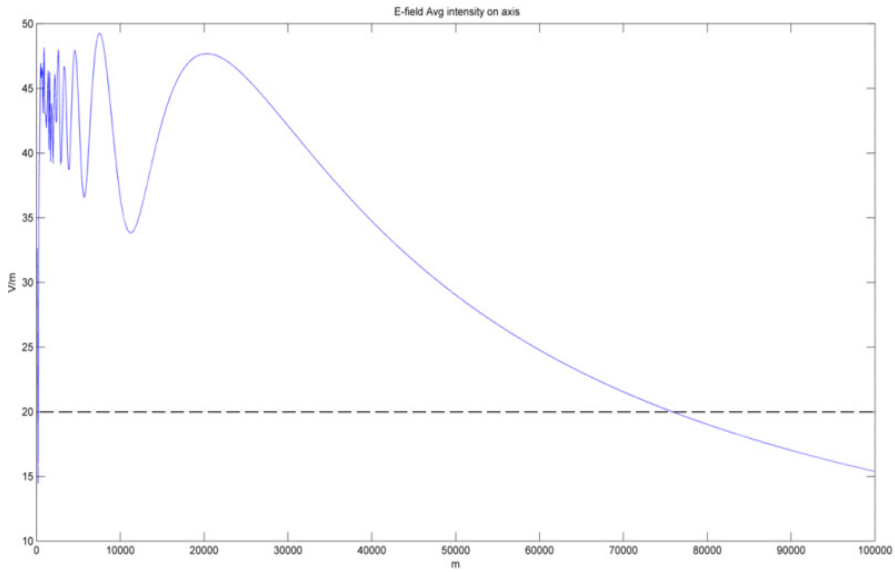

Figure 3-33: Simulated X-band average electric far field at 90° elevation along the boresight direction with the indication of the limit for the aircrafts.

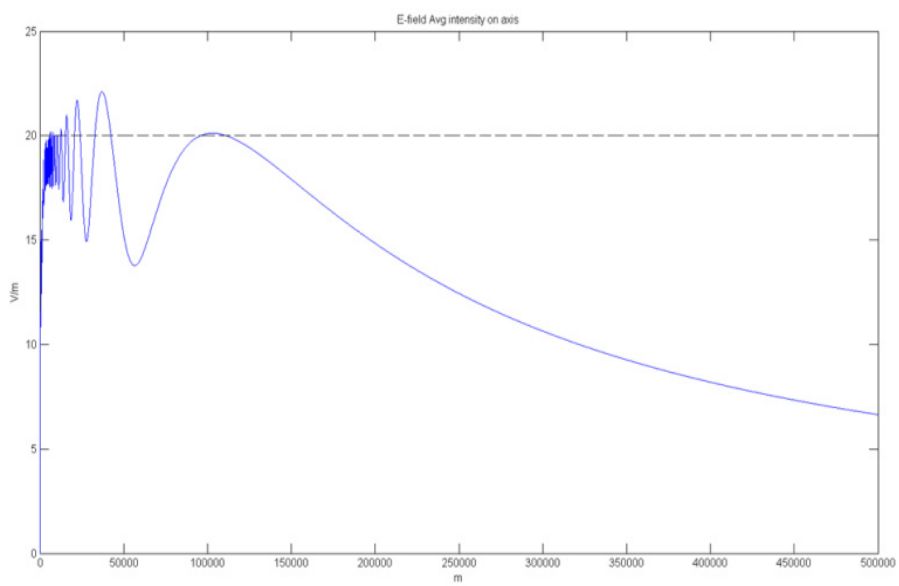

Figure 3-34: Simulated Ka-band average electric far field at 90° elevation along the boresight direction with the indication of the limit for the aircrafts.

GRASP simulations showed that, for X-band, which is definitely the most critical case as shown by Figure 3-33, a transmitted power of 800 W, instead of 5 KW, would make the antenna compliant with the 20 V/m limit. Likewise, a reduction to 450 W from 500 W in case of Ka-band transmission is enough to guarantee the fulfilment of the regulations.

3.8 Further analyses to assess the electromagnetic sustainability of the sites

EMC, EMI and safety issues are becoming progressively a paramount topic related to the sustainability of ground antenna terminals with high power of transmission. The study on SRT showed some approaches for characterising the impact on the electromagnetic environment in the surroundings of 64-m antenna, modelling its entire transmitting subsystem. Other analyses have been performed, for instance, related to the ESA deep space sites. In this concern, the author performed a study to evaluate the impact of the installation of a solar array field close to the 35-m dish of New Norcia. Different layouts proposed were investigated and simulated providing an EMC impact of the solar panels field installation on the antenna patterns, concluding that the layout shown in Figure 3-35 is not harmful in terms of irradiative characteristics of the deep space antenna (see Figure 3-36 and 3-37). Only the angular portion corresponding to the ground level elevation affects the pattern (Figure 3-37), but this portion is considerably far from the main lobe of the pattern.

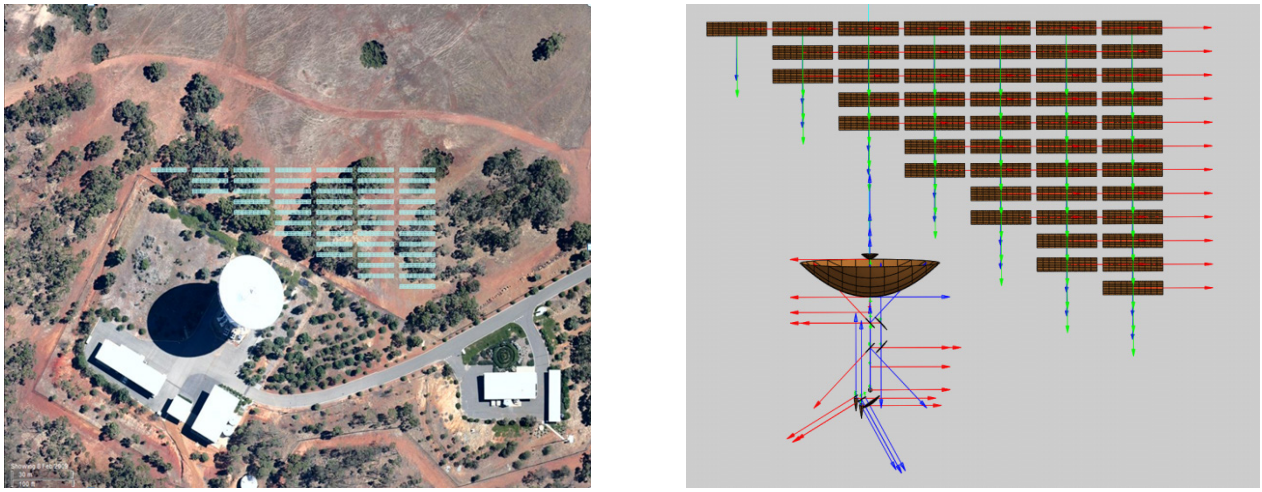

Figure 3-35: Solar panels rendering over the New Norcia site map (left). GRASP model for the simulations at 10° elevation (right).

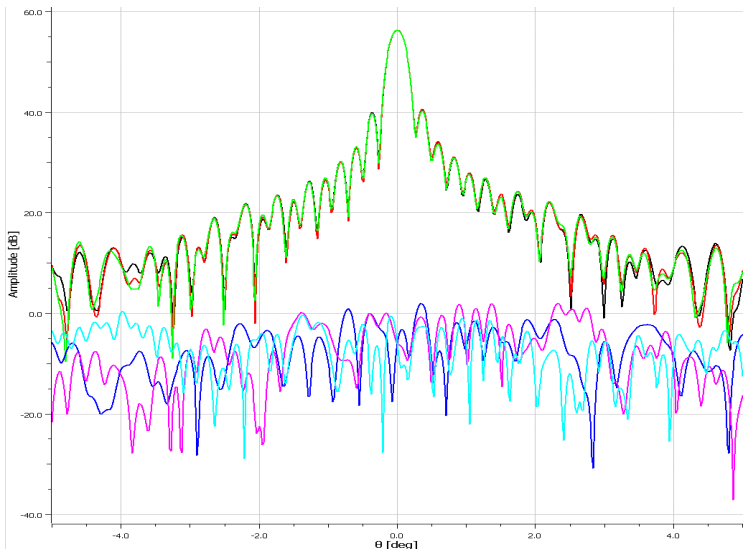

Figure 3-36: X-band radiation patterns of the DSA of New Norcia at 10° elevation without solar panels field. 3 cuts (0°, 45° and 9°0). Co-polar and Cross-polar components

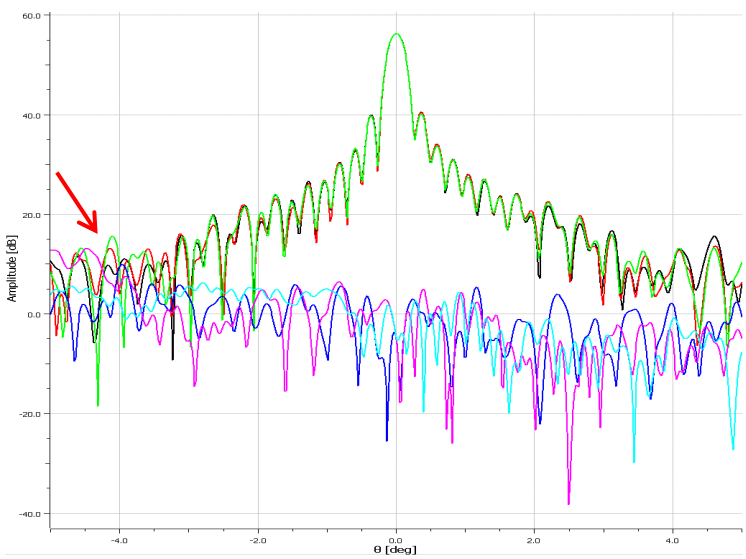

Figure 3-37: X-band radiation patterns of the DSA of New Norcia at 10° elevation with the solar panels field according to Figure 3-35. 3 cuts (0°, 45° and 9°0). Co-polar and Cross-polar components

3.9 RFI

The ITU recommendations define the antenna pattern envelopes over the full 360° angular region of a ground parabolic antenna terminal in order to ensure that a potential unknown external radio frequency interference (RFI) is not harmful (ITU-R SA.509-3 for the co-polar component, ITU-R S.731-1 for the cross polar component).

The author of this work would like to mention, at this regard, the example of the 15-m ESA ESTRACK antenna in Perth. At the beginning of 2010 the deployment of WiMAX (Worldwide Interoperability for Microwave Access) base stations has started in Perth, Western Australian. These base stations are spread all over the city and thus also close to the ESA 15-m terminal. The WiMAX base stations are transmitting down to 2302 MHz, which falls just outside the operational S-band ESA range (2200-2300 MHz). The strong signal is not properly attenuated by the standard S-Band diplexers and this caused interferences to be detected at the frequencies close to the upper edge of the operating frequency range, especially in the direction where more base stations are seen from the antenna, their signals inter-modulating each other. This had caused frequently recurrent problems to the telemetry reception of the CLUSTER 3 and CLUSTER 4 spacecrafts, showing that a shielding of such interferents was needed. This was one of the reason why the Perth terminal was shut down in 2016. As it is very likely that in the close future, WiMAX licenses will be negotiated also for the area surrounding the ESA Deep Space station of New Norcia (approx. 75 Km far away from Perth), to prevent the problems occurred in Perth, a RFI surveying for the site was required. At first instance, to monitor the current situation with respect to the base stations already operating in far areas (e.g. Perth). Secondly, to coordinate at best, when the WiMAX implementation will take place in the near-by, the location of the new deployed base stations, to facilitate a frequency coordination of the licenses and, eventually, to implement RF countermeasures to block the interfering signals from entering the receiving chain of the deep space antenna.

The author was responsible of the project for the deployment of a system able to survey some defined bands of the spectrum, sensing any potential radio frequency interfering signal and also detecting its direction of arrival, which was installed in New Norcia and afterwards in other deep space sites (se Figure 3-38).

Figure 3-38: Installed RFI scanning array in the deep space site of Cebreros (Spain)

3.10 Conclusion

The world of ground based antennas is investigated in this chapter through the introduction of various antenna topologies, all devoted to the support of space missions. Tracking techniques are presented together with the contribution of the author to the project of a small antenna terminal for the support of space launchers. Afterwards, higher classes of antennas for the support of LEO, MEO and Deep Space missions are introduced addressing to several optimization design elements the author has been dealing with. Each solution presented highlights how the space application drives the requirements on the complexity of the ground based antenna. Several factors may contribute to the optimization, aiming at enhancing the available gain. The available gain, for the case of the support of Deep Space missions, is pushed to the edge of the present technologies. A ground based antennas may be thought to be not only performance oriented and tailored to a specific use, but to have a certain degree of versatility too. The case of the upgrade of a radiotelescope towards a TT&C antenna supporting different bands and optical configurations has been analyzed. In this frame, design techniques have been presented by the author, including a *quasi-optical* analysis with the employment of Gaussian beams and an ad-hoc electromagnetic approach for the compensation of the so-called beam squint phenomenon. The analysis has been extended to an EMC, EMI and RF hazards study, so addressing to the sustainability of such powerful Earth transmitting stations with respect to the surrounding environment and the living beings, as well as to any other electronic and functional equipment of the site. In this context, all the results obtained through electromagnetic simulations are discussed and corroborated by practical considerations. When licit, the values obtained are directly compared to the applicable normative and some design countermeasures are proposed.

The deployment of a ground station antenna is, alike many other engineering projects, an effort which is not only involving technology capabilities and know-how, but also programmatic choices, requiring an exhaustive knowledge on the present and future applications and on the impact on the chosen installation territory. Furthermore, everything has to deal with political and financial issues. But, this is a different story.

Appendix A: The Gaussian beams

As a rule of thumb, the Gaussian beams approximation is applicable when objects are approximately larger than twenty wavelengths and smaller than forty wavelengths, where geometrical optics starts to be valid. Propagation within *quasi-optical* systems may be expressed as an infinite, discrete spectrum of Gaussian beam modes, which are the solution of the paraxial wave equation, derived from the Helmholtz equation. In the paraxial approximation, the field amplitude variation along the direction of propagation is assumed small over a distance comparable to the wavelength and compared to the variation on the orthogonal direction. *Quasi-optical* design is usually performed employing the fundamental mode only, and its simple formulation allows relatively straightforward implementation, high computational speed and good accuracy. Beam waveguides are usually fed by corrugated feed horns, whose field may be modeled with Gaussian beams emitted by a region of finite extent, whereas a beam expressed in terms of geometrical optics approximations is generated by an infinitesimal point source.

The fundamental mode Gaussian field may be expressed in cylindrical coordinates as:

$$E(r,Z) = \left(\frac{\omega_0}{\omega(Z)}\right)\exp\left(\frac{-r^2}{\omega^2(Z)} - jkZ - \frac{j\pi r^2}{\lambda R(Z)} + j\phi_0\right) \tag{A.3.1}$$

where k is the wave number equal to 2π/λ and ω_0 is the beam waist radius corresponding to the minimum beam radius. The beam radius ω, the radius of curvature R, and the beam phase shift ϕ_0 are defined respectively as:

$$\omega(Z) = \omega_0\sqrt{1+\left(\frac{Z}{Z_c}\right)^2} \tag{A.3.2}$$

$$R(Z) = Z + \frac{Z_c^{\,2}}{Z} \tag{A.3.3}$$

$$\phi_0(Z) = \arctan\left(\frac{Z}{Z_c}\right) \tag{A.3.4}$$

with $Z_c = \frac{\pi\omega_0^{\,2}}{\lambda}$ representing the confocal distance.

Figure A.3-1 is the schematic representation of the fundamental mode Gaussian beam electric field, showing the main parameters just introduced. As expected, at the beam waist ω_0, the electric field presents its maximum value, according to the conservation of energy principle and the radius of curvature is infinite, being the phase front planar. Moreover, according to Equation A.3.2, the beam radius varies with Z hyperbolically.

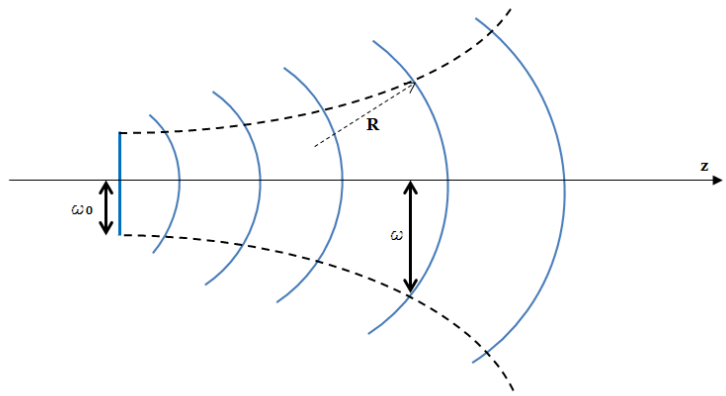

Figure A.3-1: 2D electric field distribution according to the Gaussian beam representation

The confocal distance is a critical parameter, differentiating the near and far field propagation regions. For Z less than Z_c the beam radius does not significantly change and thus the beam remains substantially collimated. When Z becomes much larger than Z_c, propagation takes place in the far-field and the beam radius grows linearly with Z.

Having defined the fundamental Gaussian mode, it is now interesting to characterize the beam in terms of its relative power level at a specific radius. Defining T_e as the edge power taper at a distance from the axis where the normalized field falls by e^{-1}:

$$T_e = \frac{P(r_e, Z)}{P(0, Z)} = \exp\left[-2\left(\frac{r_e}{\omega(Z)}\right)^2\right] \tag{A.3.5}$$

it is easy to see how the beam width ω corresponds to a taper e^{-1} with respect to the maximum value on axis (when $r_e = \omega$ and $T_e = e^{-2}$). These considerations are particularly important and useful in dimensioning a beam-waveguide reflector system, where the size of all reflectors has to be properly chosen in order to mirror the source image accurately enough, minimizing spillover, and accounting for manufacturing constraints and costs, which are typically proportional to the reflectors area. A diameter of 4ω truncates the beam at a power level of approximately 35 dB below the peak, and includes 99.97 % of the fundamental mode power.

As a consequence, if a mirror is dimensioned so that its radius is equal to 2ω, spill-over losses will be negligible (~ 0.001 dB).

The optimization of the feeds dimensions and positions may be achieved assuming a corrugated horn, employing the following relationships:

$$\omega_a = 0.664a \tag{A.3.6}$$

$$\omega_0 = \frac{\omega_a}{\sqrt{1+\left(\frac{\pi\omega_a^{\,2}}{\lambda R_h}\right)^2}} \tag{A.3.7}$$

$$\partial Z = \frac{R_h}{1+\left(\frac{2R_h}{k\omega_a^{\,2}}\right)^2} \tag{A.3.8}$$

Equation A.3.6 defines the horn aperture providing the best coupling between the horn fundamental mode HE_{11} and the Gaussian beam.

Figure A.3-2 depicts schematically the parameters just defined.

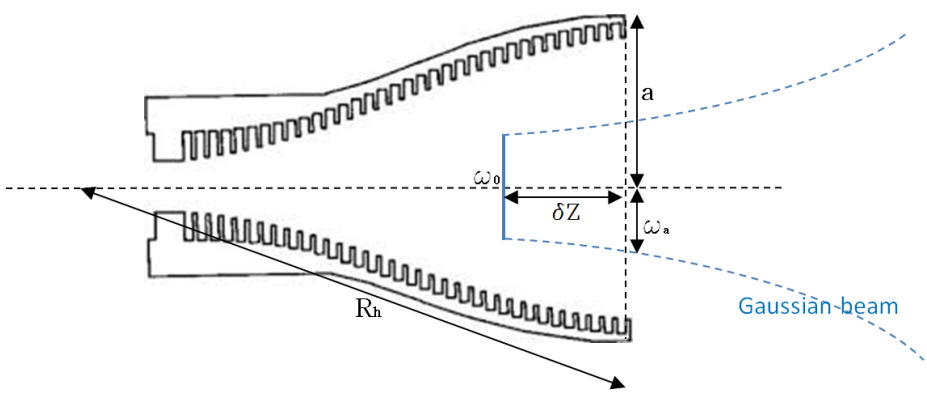

Figure A.3-2: Schematic of a corrugated horn generating a Gaussian beam

Propagation of a Gaussian beam within a system of quadric reflecting mirrors (e.g. ellipsoids, hyperboloids, and paraboloids) may be computed by considering the equivalent thin lenses employing the well-known formula:

$$\frac{1}{f_{eq}} = \frac{1}{R_1} + \frac{1}{R_2} \tag{A.3.9}$$

where R_1 and R_2 are the distances between the incidence point and the two foci of each mirror. The effect of each reflector is to transform the impinging beam defined by its radius of curvature at the incidence point R_{inc} and by its beam waist and position ω_{inc} and Z_{inc}, in a beam characterized by a radius of curvature at the incidence point R_{out} and by a beam waist and position ω_{out} and Z_{out}. In particular, defining:

$$R_{inc} = Z_{inc} + \frac{Z_{c_{inc}}^{\ 2}}{Z_{inc}} \tag{A.3.10}$$

$$\omega_m = \omega_{0_{inc}} \sqrt{1 + \left(\frac{Z_{inc}}{Z_{c_{inc}}} \right)^2} \tag{A.3.11}$$

where ω_m is the beam waist on the reflector surface, one obtains:

$$R_{out} = \frac{R_{in} f_{eq}}{R_{in} - f_{eq}} \tag{A.3.12}$$

$$\omega_{0_{out}} = \frac{\omega_m}{\sqrt{1 + \left(\frac{\pi \omega^2}{\lambda R_{out}} \right)^2}} \tag{A.3.13}$$

$$Z_{out} = \frac{R_{out}}{1 + \left(\frac{\lambda R_{out}}{\pi \omega_m^{\ 2}} \right)^2} \tag{A.3.14}$$

The parameters reported in the above formulas are depicted in Figure A.3-3 in the case of incidence on a sector of a parabola, where one focal point is infinitely distant from the impinging point. The schematic depicts the behaviour for the reflection of a Gaussian beam on a paraboloidal mirror.

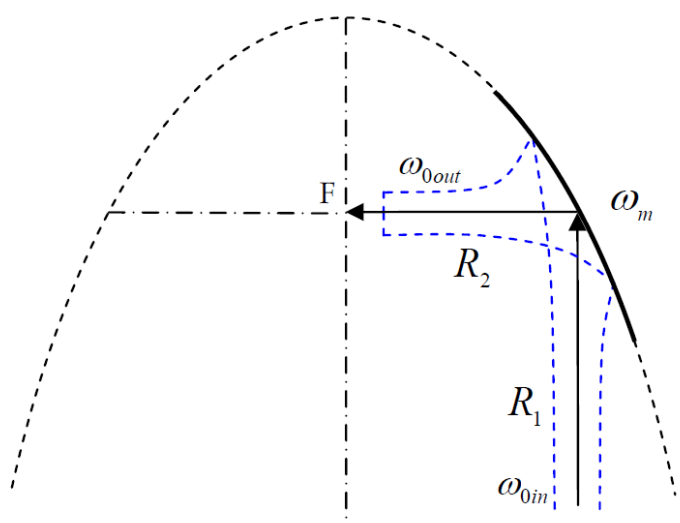

Figure A.3-3: Gaussian beam transformation by a paraboloidal reflector

Flat mirrors do not produce ay transformation on the propagating Gaussian beams, while curved ones produce a “Gaussian” transformation of the beams according to what stated above. Figure A.3-4 depicts a Gaussian beam representation over a portion of a BWG system constituted by flat and curved (paraboloidal) mirrors.

References

[3-1] G. Maral and M. Bousquet, Satellite Communications Systems, John Wiley & Sons INC., fourth edition, 2002.

[3-2] G. Billig, R. Launer, F. Pelorossi, Launcher tracking support from ESTRACK, Ground-based Space Facilities Symposium, Paris, Jun. 2013.

[3-3] G. Billig and B. Smeds, Another element in a European launcher tracking network, ESA bulletin, Aug. 2008.

[3-4] C. Barquinero, J.M. Hermoso, J. Vera, Dual S-band/X-band Tracking Antenna of Santa Maria Ground Station, ESA TTC Workshop 2013

[3-5] T. Kitsuregawa, Advanced Technology in Satellite Communication Antennas: Electrical & Mechanical Design, Artech House INC., 1990.

[3-6] Per-Simon Kildal, "The Effects of Subreflector Diffraction on the Aperture Efficiency of a Conventional Cassegrain Antenna. An Analytical Approach," IEEE Transactions on Antennas and Propagation, November 1983, pp. 903-909.

[3-7] Christophe Granet, "Designing Axially Symmetric Cassegrain or Gregorian DualReflector Antennas from Combinations of Prescribed Geometric Parameters," IEEE Antennas and Propagation Magazine, April 1998, pp. 76-82.

[3-8] W. F. Williams, "High Efficiency Antenna Reflector," Microwave Journal, Vol. 8, pp. 79-82, July 1965.

[3-9] C. J. Sletten, "Reflector and Lens Antennas: Analysis and Design Using Personal Computers," Artech House, INC., pp. 138-141, 1988.

[3-10] V. Galindo, "Design of Dual Reflector Antennas with Arbitrary Phase and Amplitude Distributions," IEEE Transactions on Antennas and Propagation, Vol. AP-12, pp. 403-408, July 1964.

[3-11] V. Galindo, "Synthesis of Dual Reflector Antennas," Electronics Research Laboratory Report 62-22, University of Califonia, Berkeley, July 30, 1964.

[3-12] G. Goubau and F. Schwering, "On the Guide Propagation of Electromagnetic Wave Beams," Institute of Radio Engineers Transactions on Antennas and Propagation, Vol. AP-9, No. 5, pp. 248–256, May 1961.

[3-13] J. Ruze, "Antenna Tolerance Theory: a Review," Proceedings of the IEEE, Vol. 54, No. 4 pp. 633-640, April 1966.

[3-14] B. Khayatian, D.Hoppe, M. J. Britcliffe and E. Gama, Reducing Near-Field RF Levels and Noise Temperature on a 34-m Beam-Waveguide Antenna by Strut Shaping, IPN Progress Report 42-192, February 15, 2013.

[3-15] W. Baan et al., "The Future of the European VLBI Network," EVN2015 [Online]. Available: http://www.evlbi.org/publications/EVN2015FinalV2.pdf, accessed Aug. 2013.

[3-16] J. Morgan, "Very long baseline interferometry in Italy wide-field VLBI imaging and astrometry and prospects for an Italian VLBI network including the Sardinia radio telescope," Ph.D. disseration, Università di Bologna, Bologna, Italy, 2010, [Online]. Available: http://amsdottorato.cib.unibo.it/2830/ accessed Aug. 2013.

[3-17] G. Tofani et al., “Status of the sardinia radio telescope project,” in Proc. SPIE Ground-Based Airborne Telescopes II, Marseille, France, Jun. 2008, vol. 7012, pp. 70120F-1–70120F-12.

[3-18] P. J. B. Clarricoats and A. D. Oliver, Corrugated Horns for Microwave Antennas. London, U.K.: Institution of Engineering and Technology, Mar. 1984.

[3-19] M. Pasian, M. Bozzi, and L. Perregrini, “Accurate modeling of dichroic mirrors in beam-waveguide antennas,” IEEE Trans. Antennas Propag., vol. 61, no. 4, pp. 1931–1938, Apr. 2013.

[3-20] M. Bozzi, L. Perregrini, J. Weinzierl, and C. Winnewisser, “Efficient analysis of quasi-optical filters by a hybrid MoM/BI-RME method”, IEEE Trans. Antennas Propag., vol. 49, no. 7, pp. 1054–1064, Jul. 2001.

[3-21] T. A. Milligan, Modern Antenna Design. Hoboken, NJ, USA: Wiley, 2005.

[3-22] P. F. Goldsmith, Quasioptical Systems: Gaussian Beam Quasioptical Propagation and Applications ser. Chapman & Hall Publishers Series on Microwave Technology and RF, Piscataway, NJ, USA: IEEE Press, 1998.

[3-23]D. P. Mackey and A. B. Calloway, “Planning and operations for superior solar conjunctions during the MESSENGER mission,” in Proc. IEEE Aerosp. Conf., Big Sky, MT, USA, Mar. 3–10, 2012, pp. 1–6.

[3-24] P. Besso, M. Bozzi, M. Formaggi, and L. Perregrini, “A novel technique for high-performance correction of beam aberration in deep space antennas,” IEEE Antenna Wireless Propag. Lett., vol. 6, pp. 376–378, 2007.

[3-25] IEC 61000-6-1, Part 6-2: Generic standards - Immunity for residential, commercial and light-industrial environments, ed2.0, 2005.

[3-26] RTCA DO-160G standard, Environmental conditions and test procedure for airborne equipment, section 05/05/2011.

[3-27] Electronic Communications Committee (ECC), Protection of aircraft from satellite Earth station operating on the ground in the vicinity of airfields, Report 66, Riga, June 2005.

[3-28] Italian Ministerial Act N.381 10/09/1998, Regolamento recante norme per la determinazione dei tetti di radiofrequenza compatibili con la salute umana.

[3-29] https://www.pplir.org/latest-news/394-ads-b-gets-easa-nod-for-sole-surveillance-reports-david-learmount

Chapter 4

MEDIA PENETRATING ANTENNAS

How a media penetrating antenna shall be?

A media penetrating antenna shall be as much electromagnetically penetrating as permissible by its application.

4.1 Introduction

In the previous chapters, cases where the propagation was given in free space conditions were considered. In the present chapter, electromagnetic problems are discussed, where the radiation encounters different media during its propagation. Electromagnetic propagation through the interface of different media has been in the years an interesting and challenging topic of study and research [4-1][4-2][4-3]. The constraints related to such problematic are sometime strongly boundary, but often various interesting solutions were developed in order to overtaken them [4-4]. In the present dissertation the theory behind the electromagnetic propagation through dissipative media is presented together with some technical solutions to achieve the so called deep penetration. With the term deep penetration, it is intended the penetration of the electromagnetic radiation into the medium impinged, trough the surface, for distances much bigger than the radiation wavelength. In particular, in the present work, it is shown that, for inhomogeneous waves, specific conditions exist for the phase and the attenuation vectors to achieve the deep wave penetration into lossy dielectrics. A lossy dielectric is a medium in which an electromagnetic wave loses power as it propagates due to poor conduction. In other words, a lossy dielectric is a partially conducting medium (imperfect dielectric or imperfect conductor) with electric conductivity $\sigma \neq 0$ but $< \infty$, as distinct from a lossless dielectric (perfect or good dielectric), for which $\sigma = 0$.

4.2 Theoretical background

Considering a lossy dielectric medium (with characteristics of linearity, isotropy, homogeneity [4-1]), that is charge free and omitting the time factor, one can easily transform the Maxwell equations into the homogeneous vector Helmholtz equations:

$$\nabla^2 \underline{E} - k^2 \underline{E} = 0$$
$$\nabla^2 \underline{H} - k^2 \underline{H} = 0 \tag{4.1}$$

where:

$$k^2 = j\omega\mu(\sigma + j\omega\varepsilon) \tag{4.2}$$

k is called the propagation constant (in per meter) of the medium, where ω is the angular frequency of the radiation expressed by the fields $\underline{E}$ and $\underline{H}$. σ is the conductivity, μ is the permeability and ε is the permittivity; they represent the three constitutive parameters of the medium.

Since k in Equations (4.2) is a complex quantity, we may let:

$$k = \alpha + j\beta \tag{4.3}$$

We obtain α and β by noting that :

$$-\mathrm{Re}(\mathrm{k}^2) = \beta^2 - \alpha^2 = \omega^2\mu\varepsilon \tag{4.4}$$

and

$$\left|k^2\right| = \beta^2 + \alpha^2 = \omega\mu\sqrt{\sigma^2 + \omega^2\varepsilon^2} \tag{4.5}$$

From the equations (4.4) and (4.5), we obtain:

$$\alpha = \omega\sqrt{\frac{\mu\varepsilon}{2}\left[\sqrt{1+\left[\frac{\sigma}{\omega\varepsilon}\right]^2} - 1\right]} \tag{4.6}$$

$$\beta = \omega\sqrt{\frac{\mu\varepsilon}{2}\left[\sqrt{1+\left[\frac{\sigma}{\omega\varepsilon}\right]^2} + 1\right]} \tag{4.7}$$

Without loss of generality, if we assume that the wave propagates along $+a_z$ and that $\underline{E}$ has only an x-component, then we obtain from the homogeneous Helmholtz equations:

$$H = \frac{E_0}{|\eta|} e^{-\alpha z} \cos(\omega t - \beta z - \theta_\eta) a_y \tag{4.8}$$

where η represents the wave impedance and θ_η angle between the $\underline{E}$ and $\underline{H}$ vectors.

It can be noticed from equation (4.8) that as the wave propagates along $+a_z$, it decreases or attenuates in amplitude by a factor $e^{-\alpha z}$ and hence α is known as the attenuation constant of the medium. It is a

measure of the spatial rate of the decay of the wave in the medium. The distance d through which the wave amplitude decreases by a factor e^{-1} is called skin depth or penetration depth of the medium. The skin depth is a measure of the depth to which an electromagnetic wave can penetrate the medium:

$$d = \frac{1}{\alpha} \tag{4.9}$$

Table 1 reports the skin depth obtained with a pure conductor (silver), a good ferromagnetic conductor (the iron) and an imperfect dielectric (the sea water). The sea water has a non-negligible conductive component and it will be the ultimate study case of the present analysis in order to seek for the deep penetration in imperfect dielectrics. Table 1 shows clearly the strong dependence of the skin depth with the frequency of operation.

Table 4-1: Skin depths for different materials at various frequencies

Material	Properties	d		
		f = 60 Hz	f = 1 MHz	f = 1 GHz
Silver	$\sigma = 6.17\times10^{7}$ S/m	8.27 mm	0.064 mm	0.002 mm
Iron	$\sigma = 1.00\times10^{7}$ S/m $\mu_r \approx 10^{3}$	0.65 mm	0.005 mm	0.00016 mm
Seawater	$\sigma = 4$ S/m $\varepsilon_r = 72$	32 m	0.25 m	12.37 mm

From equation (4.6) we notice that if $\sigma = 0$, as is the case for a lossless medium such as free space, α equals zero and the wave is not attenuated as it propagates. The quantity β is a measure of the phase shift per length and it is called the phase constant or wave number. In terms of β, the wave velocity υ and the wavelength λ are, respectively, given by:

$$\upsilon = \frac{\omega}{\beta} \tag{4.10}$$

$$\lambda = \frac{2\pi}{\beta} \tag{4.11}$$

Finally, it shall be noted that the ratio of the magnitude of the conduction current density J to that of the displacement current density (rate of change of electric displacement field) J_d in a lossy medium is:

$$\frac{|J|}{|J_d|} = \frac{|\sigma E|}{|j\omega\varepsilon E|} = \frac{\sigma}{\omega\varepsilon} = \tan\delta \tag{4.12}$$

where $\tan\delta$ is known as the loss tangent and δ is the loss angle of the medium. Although a line of demarcation between good conductors and lossy dielectrics is not easy to make, $\tan\delta$ may be used to determine how lossy a medium is. A medium is said to be a good (lossless or perfect) dielectric as much as $\tan\delta$ is close to zero.

From the viewpoint of wave propagation, the characteristic behavior of a medium depends not only on its constitutive parameters σ, ε and μ but also on the frequency of operation. A medium that is regarded as a good conductor at low frequencies may be a good dielectric at high frequencies. This is reflected in the definition of $\tan\delta$, which is frequency dependent. The $\tan\delta$ can be also written as:

$$\tan\delta = \frac{\varepsilon''}{\varepsilon'} \tag{4.13}$$

Being ε' and ε'' the real and imaginary part of the so-called complex permittivity of the medium, defined as:

$$\varepsilon_c = \varepsilon\left[1 - j\frac{\sigma}{\omega\varepsilon}\right] = \varepsilon_0(\varepsilon' - j\varepsilon'') \tag{4.14}$$

Considering again (4.5), we may re-write for non-dispersive media (ε and μ real and positive and σ real non-negative):

$$k^2 = \omega^2\mu\varepsilon_c = \omega^2\mu\left(\varepsilon - j\frac{\sigma}{\omega}\right) = \omega^2\mu\varepsilon - j\omega\mu\sigma \tag{4.15}$$

Considering a generic expression of the field as:

$$\underline{E} = \underline{E}_0 e^{j\underline{k}\cdot\underline{r}} \tag{4.16}$$

where $\underline{k}$ is the complex propagation vector $\underline{k} = \underline{\alpha} + j\underline{\beta}$, we can note that the functional expression of the spatial derivative of the ∇ coincides with the vector $j\underline{k}$, thus the first of the homogeneous vector Helmholtz equations becomes:

$$\nabla^2\underline{E} + k^2\underline{E} = \nabla\cdot\nabla\underline{E} + k^2\underline{E} = j\underline{k}\cdot j\underline{k}\underline{E} + k^2\underline{E} = 0 \tag{4.17}$$

which leads to

$$\underline{k}\cdot\underline{k} = k^2 \tag{4.18}$$

Also known as the separability condition. The separability condition allows to derive the other important relation:

$$\underline{\beta}\cdot\underline{\alpha} = \frac{\omega\mu\sigma}{2} \tag{4.19}$$

$\underline{\alpha}$ and $\underline{\beta}$ are termed as attenuation and phase (or propagation) vectors, respectively.

For non-dissipative (lossless) media, σ equals zero. Being $\underline{\beta}$ non-null, this results in either $\underline{\alpha} = 0$ or $\underline{\beta} \perp \underline{\alpha}$. Therefore this relation shows that, for non-dissipative media, the attenuation vector can be non-null. This is the case of a non-uniform (non-homogenous) plane wave, attenuated in the direction orthogonal to propagation.

An electromagnetic wave is called uniform or homogenous if the equi-amplitude surfaces coincides with the equi-phase surfaces. Being the equi-amplitude surfaces the surfaces on which the wave has a constant amplitude (there perpendicular to the attenuation vector) and the equi-phase surfaces the surfaces on which the wave has a constant phase (there perpendicular to the phase vector), an homogenous wave presents either $\underline{\beta} \parallel \underline{\alpha}$ or $\underline{\alpha} = 0$.

For dissipative media $\underline{\alpha} \neq 0$. Therefore, for homogenous wave must be $\underline{\beta} \parallel \underline{\alpha}$.

The table below summarizes the four possible cases.

Table 4-2: Types of waves and types of media

Wave / Medium	**Lossless**	**Dissipative**
Homogenous	$\underline{\alpha} = 0$	$\underline{\alpha} \neq 0$ $\beta \cdot \alpha = \beta\alpha$
Inhomogeneous	$\underline{\alpha} \neq 0$ $\beta \cdot \alpha = 0$	$\underline{\alpha} \neq 0$ $\beta \cdot \alpha = \beta\alpha \cos\eta$

4.3 Conditions for the deep wave penetration

The cases reported in Table 4.2 related to an homogenous wave are of less interest, because either the wave is not attenuated in a lossless medium or the wave is attenuated in the direction of propagation, as expected. Inhomogeneous waves are of much interest, since the direction of attenuation is in general different from the direction of propagation (even orthogonal, in the case of lossless media) and this property can be used to achieve the deep penetration. In particular, willing to penetrate dissipative media, we should consider the following relations for non-ferromagnetic materials, easily derived from the relations given above:

$$\beta^2 - \alpha^2 = k_0{}^2 \varepsilon'$$
$$2\beta\alpha\cos\eta = k_0{}^2 \varepsilon'' \tag{4.20}$$

where the first one is also known as the dispersion condition.

$k_0 = \omega^2 \mu_0 \varepsilon_0$ is the vacuum wave number.

With some algebra, we can derive:

$$\beta = k_0 \sqrt{\frac{\varepsilon'}{2}} \sqrt{\sqrt{1 + \left(\frac{\varepsilon''}{\varepsilon'\cos\eta}\right)^2} + 1}$$
$$\alpha = k_0 \sqrt{\frac{\varepsilon'}{2}} \sqrt{\sqrt{1 + \left(\frac{\varepsilon''}{\varepsilon'\cos\eta}\right)^2} - 1} \tag{4.21}$$

Although they are not handy expressions, (4.21) indicate that the phase and attenuation constants are determined by the properties of the lossy material and that the only free parameter is the so-called inhomogeneity angle η, which depends on the inhomogeneous wave impinging the medium. The inhomogeneity angle is the angle measuring the difference between the directions of the $\underline{\alpha}$ and $\underline{\beta}$ vectors.

Let us now consider a planar interface between a lossy medium 2 with a medium 1 (either lossless or lossy) from where the electromagnetic inhomogeneous wave is travelling, according to Figure 4-1.

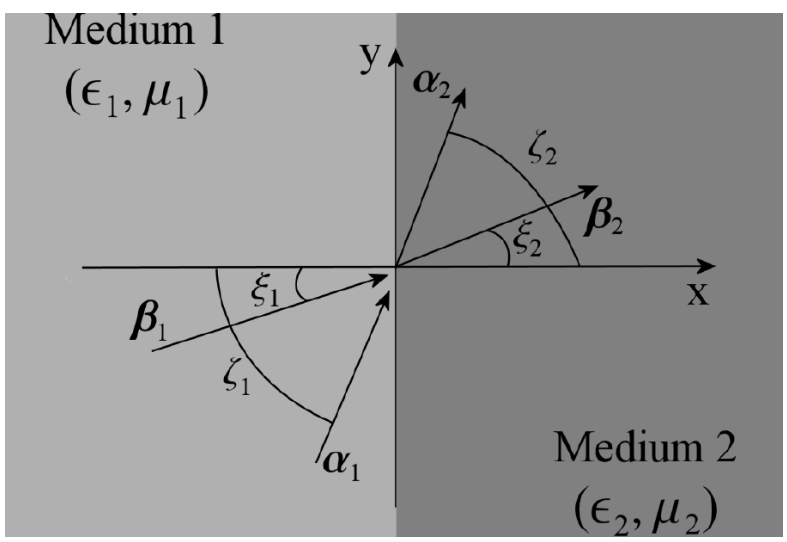

Figure 4-1. Interface between two different media with generic attenuation and phase vectors

The half-space $x<0$ is filled with a medium 1, with relative permittivity and permeability ε_1 and μ_1, respectively, while the half-space $x>0$ is filled with a medium 2, with relative permittivity and permeability ε_2 and μ_2, respectively. Let suppose that both media are non-ferromagnetic and dissipative, i.e., $\varepsilon_n = \varepsilon_n' + j\varepsilon_n''$, for n=1,2 and let consider an inhomogeneous plane wave from medium 1, that impinges on the interface between the two media. The incident wave would be in *E* or *H* polarization, i.e., with the electric or magnetic field purely parallel to the interface, respectively. Being an inhomogeneous wave, it is characterized by having a phase and an attenuation vector which are non-parallel (see Table 4-2). The phase vector $\underline{\beta}_1$ forms an angle ξ_1 with the *x- axis*, while the attenuation vector $\underline{\alpha}_1$ forms an angle ζ_1 with the same axis, see Figure 4-1. The inhomogeneity angle η_1 is equal to $\zeta_1 - \xi_1$. The incident wave is therefore inhomogeneous if $\alpha_1 \neq 0$ and $\xi_1 \neq \zeta_1$. If the medium 1 is lossy, then α_1 and β_1 are connected to the medium characteristics by the relations expressed in (4.21).

On the other side, if the medium 1 is lossless, η_1 is simply equal to $\pi / 2$.
Inhomogeneous waves propagating in a lossless media are also termed as leaky waves. In fact, their generation is generally made possible by introducing some leakage effect in the travelling-wave path of the guiding structure, the so-called leaky-wave antennas.

After this considerations, we can write the following expression for the two component of the incident propagation vector:

$$\begin{aligned} \underline{\beta}_i &= \beta_1(\underline{x}_0 \cos\xi_1 + \underline{y}_0 \sin\xi_1) \\ \underline{\alpha}_i &= \alpha_1(\underline{x}_0 \cos\zeta_1 + \underline{y}_0 \sin\zeta_1) \end{aligned} \tag{4.22}$$

and similarly for the reflected and the transmitted wave vector:

$$\begin{aligned} \underline{\beta}_r &= \beta_1(-\underline{x}_0 \cos\xi_1 + \underline{y}_0 \sin\xi_1) \\ \underline{\alpha}_r &= \alpha_1(\underline{-x}_0 \cos\zeta_1 + \underline{y}_0 \sin\zeta_1) \end{aligned} \tag{4.23}$$

$$\begin{aligned} \underline{\beta}_t &= \beta_2(\underline{x}_0 \cos\xi_2 + \underline{y}_0 \sin\xi_2) \\ \underline{\alpha}_t &= \alpha_2(\underline{x}_0 \cos\zeta_2 + \underline{y}_0 \sin\zeta_2) \end{aligned} \tag{4.24}$$

The amplitude of the transmitted vectors and the angles that they form with the perpendicular to the interface can be obtained with some algebra from the (4.21) and the generalized Snell condition:

$$\begin{aligned} \beta_1 \sin\xi_i &= \beta_2 \sin\xi_t \\ \alpha_1 \cos\zeta_i &= \alpha_2 \sin\zeta_t \end{aligned} \tag{4.25}$$

One obtains:

$$\beta_2 = \sqrt{\frac{\left|k_{1y}\right|^2 + k_0{}^2\varepsilon'_2 + \left|k_{1y}{}^2 - k_2{}^2\right|}{2}}$$
$$\alpha_2 = \sqrt{\frac{\left|k_{1y}\right|^2 - k_0{}^2\varepsilon'_2 + \left|k_{1y}{}^2 - k_2{}^2\right|}{2}} \tag{4.26}$$

The transmitted angles will be:

$$\xi_2 = \begin{cases} \arcsin(\frac{\beta_1}{\beta_2}\sin\xi_1) & \text{with } \xi_1 < \xi_1^{\xi} \\ \pi - \arcsin(\frac{\beta_1}{\beta_2}\sin\xi_1) & \text{with } \xi_1 > \xi_1^{\xi} \end{cases} \tag{4.27}$$

$$\zeta_2 = \begin{cases} \arcsin(\frac{\alpha_1}{\alpha_2}\sin\zeta_1) & \text{with } \xi_1 < \xi_1^{\zeta} \\ \pi - \arcsin(\frac{\alpha_1}{\alpha_2}\sin\zeta_1) & \text{with } \xi_1 > \xi_1^{\zeta} \end{cases} \tag{4.28}$$

where ξ_1^{ξ} and ξ_1^{ζ} are the two critical angles for which ξ_2 and ζ_2 are found to match $\pi/2$, respectively. For ξ_1^{ξ}, the transmitted wave is similar to a surface wave ($\xi_2 = \pi/2$), having the constant phase plane orthogonal to the interface. For ξ_1^{ζ}, the transmitted wave is not attenuated towards the second medium. In fact the transmitted wave has the constant amplitude plane orthogonal to the interface ($\zeta_2 = \pi/2$). We call this wave a deep penetrating wave (DPW).

Considering then $\zeta_2 = \zeta_t = \pi/2$ (DPW), we easily obtain from the generalized Snell equations and the dispersion condition:

$$\beta_1\alpha_1\sin(2\xi_i) = k_0^2\varepsilon_2'' \tag{4.29}$$

Inverting this equation, we obtain the following critical incident angle:

$$\xi_c = \frac{1}{2}\arcsin\left[\frac{\mathrm{Im}(k_2^2)}{\beta_1\alpha_1}\right] \tag{4.30}$$

This equation makes sense when the argument of the inverse sine is less than 1. From this constraint and the relations previously introduced, we can calculate the minimum value of β_1, which allows the deep penetration effect. With some algebra we find the following condition:

$$\beta_1 \geq \frac{k_1}{\sqrt{2}}\sqrt{1+\sqrt{1+\left[\frac{2\,\mathrm{Im}(\mathrm{k}_2^2)}{k_1^2}\right]^2}} \tag{4.31}$$

The separability condition ensures that if the relation (4.31) is valid, both α_1 and β_1 are such to allow the DPW condition.

The ability of inhomogeneous waves of attaining the deep penetration condition has been therefore demonstrated.

4.4 Generating inhomogeneous waves

As introduced, inhomogeneous waves can be generated in lossless media by means of appropriate radiative structures, in which the field shows a complex wave number. These field solutions are also known as leaky waves. In recent studies, it has been pointed out that an inhomogeneous wave can also be obtained by illuminating with a homogeneous wave a dissipative dielectric [4-5]. In the present dissertation the generation of inhomogeneous waves in a lossless medium from a homogeneous wave is demonstrated. Let us consider a lossy two-dimensional triangular prism immersed in the free space as a dissipative dielectric with two non-parallel interfaces, forming an angle χ, as shown in Figure 4-2. We consider a quasi-plane wave incident at an angle ξ_{1i} on the left side (vertical side) of the prism. We suppose that, using a geometrical-optics approximation, given the characteristics of a quasi-plane wave, the wave does not interact with the prism's wedges. In other words, a finite beam is considered impinging on the prism.

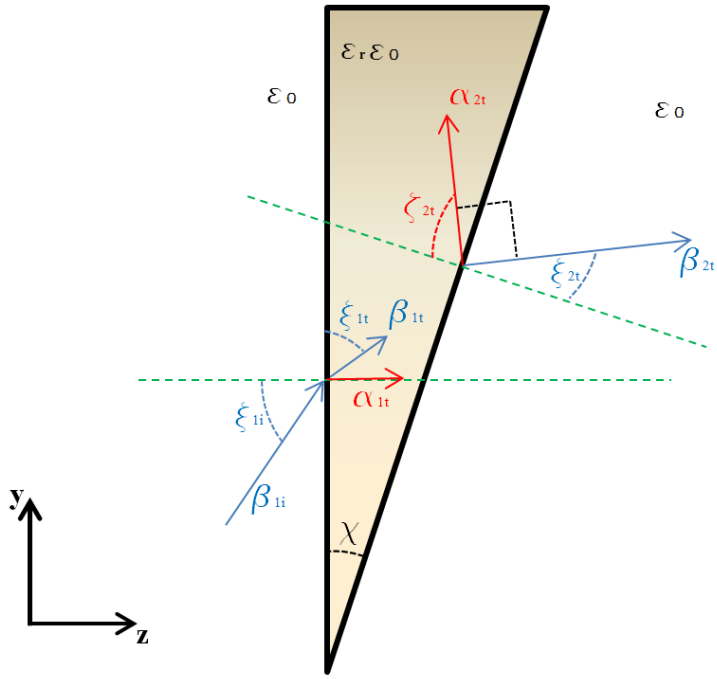

Figure 4-2: Geometry of the proposed configuration with the dielectric prism

The reflected and transmitted waves in the system of Figure 4-2 can be easily computed at both interfaces with well-known relations [4-6]. While the incident vector has a null attenuation vector (lossless medium), the wave transmitted after each interface has both non-null attenuation and phase vectors. At the first interface (vertical side) of the prism, the phase vector forms an angle ξ_{1i} with respect to the z-axis, while the attenuation vector must be perpendicular to the interface. The wave impinges then on the second interface (oblique side) of the prism with an angle of the phase vector equal to (ξ_{1t} + χ) with respect to the normal direction to the interface. The attenuation vector impinges on the second interface with an angle χ with respect to the normal direction to the interface. The reflected and transmitted waves at the second interface can be computed using the results presented in [4-7]–[4-9]. In particular, the transmitted wave results as an inhomogeneous wave. In fact, in a lossless medium (e.g. the free space), the attenuation vector and the phase vector computed after the second interface result orthogonal, as shown hereafter, meaning that the equi-phase planes and the equi-amplitude planes are perpendicular to each other.

Considering that $\alpha_{1i} = 0$ (homogenous wave in a lossless medium), the propagation constants after the first interface, inside the prism, are easily derived from (4.26):

$$\beta_{1t} = \sqrt{\frac{\left|\beta_{1iy}\right|^2 + k_0{}^2\varepsilon'_p + \left|\beta_{1iy}{}^2 - k_p{}^2\right|}{2}}$$
$$\alpha_{1t} = \sqrt{\frac{\left|\beta_{1iy}\right|^2 - k_0{}^2\varepsilon'_p + \left|\beta_{1iy}{}^2 - k_p{}^2\right|}{2}} \tag{4.32}$$

where $\varepsilon_p = \varepsilon_0\varepsilon_r$ is the complex permittivity of the dielectric prism and $k_p = \omega\sqrt{\varepsilon_p\mu_0}$ is its propagation constant, assuming that the prism is non-ferromagnetic. Similarly:

$$\xi_{1t} = \arcsin(\frac{\beta_{1i}}{\beta_{1t}}\sin\xi_{1i}) \tag{4.33}$$

and $\zeta_{1t} = 0$ because $\alpha_{1i} = 0$.

Considering the second interface (prism-free space), the same relations give the propagation constants and angles related to the wave emerging from the inclined face of the prism:

$$\beta_{2t} = \sqrt{\frac{\left|\beta_{2iy}\right|^2 + k_0{}^2\varepsilon_0 + \left|\beta_{2iy}{}^2 - k_0{}^2\right|}{2}}$$
$$\alpha_{2t} = \sqrt{\frac{\left|\beta_{2iy}\right|^2 - k_0{}^2\varepsilon_0 + \left|\beta_{2iy}{}^2 - k_0{}^2\right|}{2}} \tag{4.34}$$

Since, at the second interface, a new reference frame is set, resulting in :

$$\xi_{2i} = \xi_{1t} + \chi$$
$$\zeta_{2i} = \chi \tag{4.35}$$

the relations of the angles can be written as:

$$\xi_{2t} = \arcsin(\frac{\beta_{2i}}{\beta_{2t}}\sin(\xi_{2i} + \chi)) \tag{4.36}$$

$$\zeta_{2t} = \arcsin(\frac{\alpha_{2i}}{\alpha_{2t}}\sin\chi) \tag{4.37}$$

It is possible to demonstrate, using a some algebraic procedure that, for any ξ_{1i}, χ and any material of the dielectric prism:

$$\eta_{2t} = \zeta_{2t} - \xi_{2t} = \pm\frac{\pi}{2} \tag{4.38}$$

The relation (4.38) shows that the propagation vectors are orthogonal, hence the wave generated after the two interfaces of dielectric prism is an inhomogeneous wave, while the impinging wave was a homogenous wave.

For the sake of brevity, such demonstration is not reported in the present dissertation. It has been deemed more beneficial to show tables, which summarise this relevant result for two important study cases, referring to VHF and X- bands respectively.

Table 4-3: Computed theoretical values for the propagation vectors for a FR4 prism, with ξ_{1i} =10°, χ =5°, β_{1i} = k_0 at 300 MHz.

Parameter	Value	Unit
ξ_{1i}	10	deg
χ	5	deg
frequency	300	MHz
material of the prism	FR4 ($\varepsilon'_r = 4.3$; $tg\delta = 0.025$)	
β_{1t} / k_0	2.07380	m^{-1}
α_{1t} / k_0	0.02600	m^{-1}
ξ_{1t}	4.8032	deg
ζ_{1t}	0	deg
η_{1t}	-4.8032	deg
β_{2t} / k_0	1.0000027	m^{-1}
α_{2t} / k_0	0.000242	m^{-1}
ξ_{2t}	20.6768	deg
ζ_{2t}	69.3232	deg
η_{2t}	90	deg

Table 4-4: Computed theoretical values for the propagation vectors for a FR4 prism, with ξ_{1i} =10°, χ =5°, β_{1i} = k_0 at 10600 MHz.

Parameter	Value	Unit
ξ_{1i}	10	deg
χ	5	deg
frequency	10600	MHz
material of the prism	FR4 ($\varepsilon'_r = 4.3$; $tg\delta = 0.025$)	
β_{1t} / k_0	2.07380	m^{-1}
α_{1t} / k_0	0.02600	m^{-1}
ξ_{1t}	4.8032	deg
ζ_{1t}	0	deg
η_{1t}	-4.8032	deg
β_{2t} / k_0	1.0000027	m^{-1}
α_{2t} / k_0	0.000242	m^{-1}
ξ_{2t}	20.6768	deg
ζ_{2t}	69.3232	deg
η_{2t}	90	deg

4.5 Electromagnetic analysis with the theoretical model

In order to undertake more extensive electromagnetic simulations, the system described in Figure 4-2 was finally considered to work at X-band (10.6 GHz) aiming at reducing the dimensions for the prism and, ultimately, at investigating the viability of generating an inhomogeneous wave for the deep penetration through lossy media at such frequencies, as never done before in the literature.

If we consider the case of a prism with the real part of the relative permittivity ε'_r = 4.3 and the loss tangent $tg\delta$ = 0.025 (FR4 dielectric material), we can obtain the theoretical calculation of the properties of the transmitted wave after the double transmission through the prism's interfaces: both magnitude and direction (i.e. angles) of the phase and attenuation vectors are calculated by a MALTAB routine. Since the prism is dissipative, we can suppose that the wave is strongly attenuated as far as reflections are concerned. Therefore, the contribution to the transmitted wave (after the second interface) is only given by the direct wave and any reflection is neglected.

Varying the four characteristic parameters of the system (χ, ξ_{1i}, ε'_r and $tg\delta$), relevant numerical results can be obtained. In Figures 4-3 and 4-4 the magnitudes of the attenuation and phase vectors are shown, respectively, as functions of the angle of incidence and of the angle of the prism considering a FR4 dielectric. A step-behaviour of the magnitudes can be noted. The vectors are approximately constant

and equal to zero and k_0, respectively, for a wide spectrum of the incident angles but the magnitude of both starts to increase for values larger than a specific angle. This behaviour is of extreme interest: in fact, as it has been pointed out in the literature [4-8] and demonstrated in the present dissertation (see relation (4.31)), inhomogeneous waves with attenuation and phase components higher than a defined threshold are able to deeply penetrate in lossy materials and they can be of interest in several applications. Figure 4-4 pins some critical angles corresponding to each defined case of χ. We have to emphasize that the magnitude of the attenuation vector is never zero before the critical angle, but it is considerably smaller than one, as typical for inhomogeneous waves generated by leaky-wave antennas. In this regard, the plot of the ratio β_{2t}/α_{2t} (see Figure 4-5) is very handy. Furthermore, such quantity gives a comprehensive indication of the step behaviour individuated by the present analysis, with respect to the characteristic parameters. Figure 4-5 shows a strong dependence of the ratio β_{2t}/α_{2t} and of the critical angle on the angle of the prism. In particular, increasing the angle of the triangular prism, reduces the possibility of having a large β_{2t} (necessary for the deep penetration of the so generated inhomogeneous wave) and the range of incident angles for which the transmitted wave is a usable wave according to Figures 4-6 and 4-7. In these figures, the transmitted angles of the attenuation and phase vectors are, respectively, shown as functions of the incident angle and the prism angle. An analogous step behaviour is noted. The attenuation vector's angle grows with the initial incident angle and reaches a direction almost perpendicular to the oblique interface starting from the critical angle. Similarly, the phase vector becomes quasi-parallel to the oblique interface starting from a critical initial angle of incidence. In other words, after a critical angle the transmitted wave behaves like a *quasi-surface* wave (see Figure 4-8).

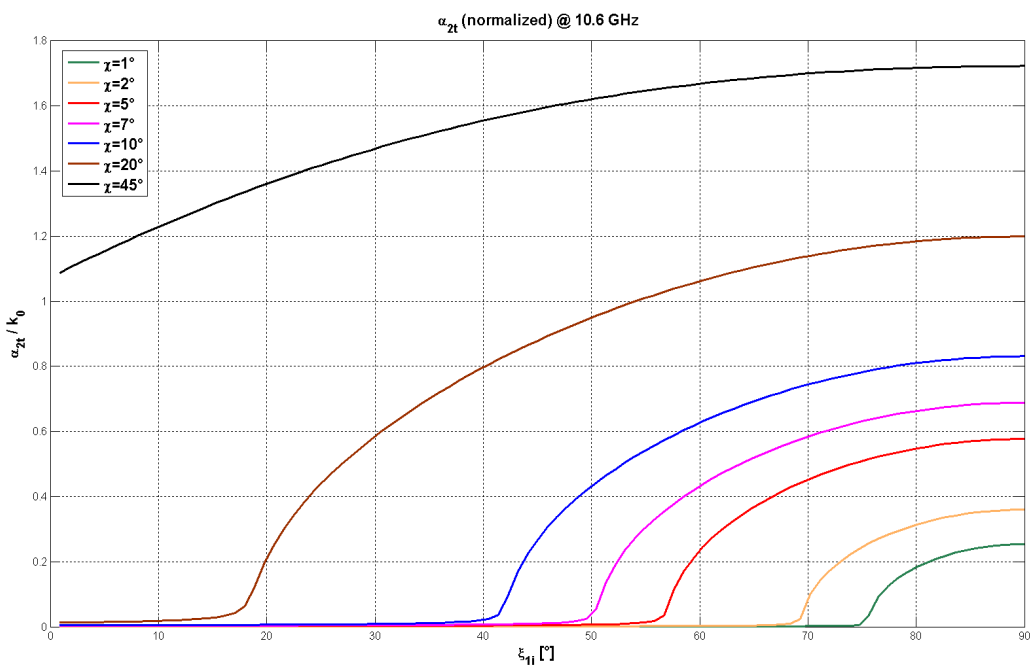

Figure 4-3: α_{2t} **as a function of** ξ_{1i} **for some cases of** χ **for a FR4 prism**

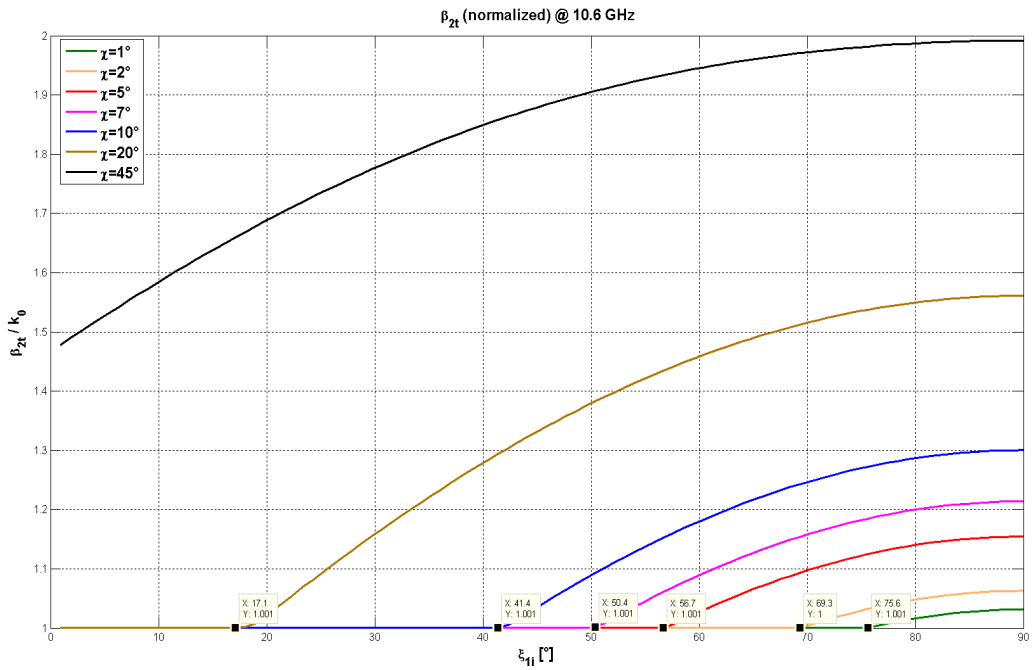

Figure 4-4: β_{2t} **as a function of** ξ_{1i} **for some cases of** χ **for a FR4 prism**

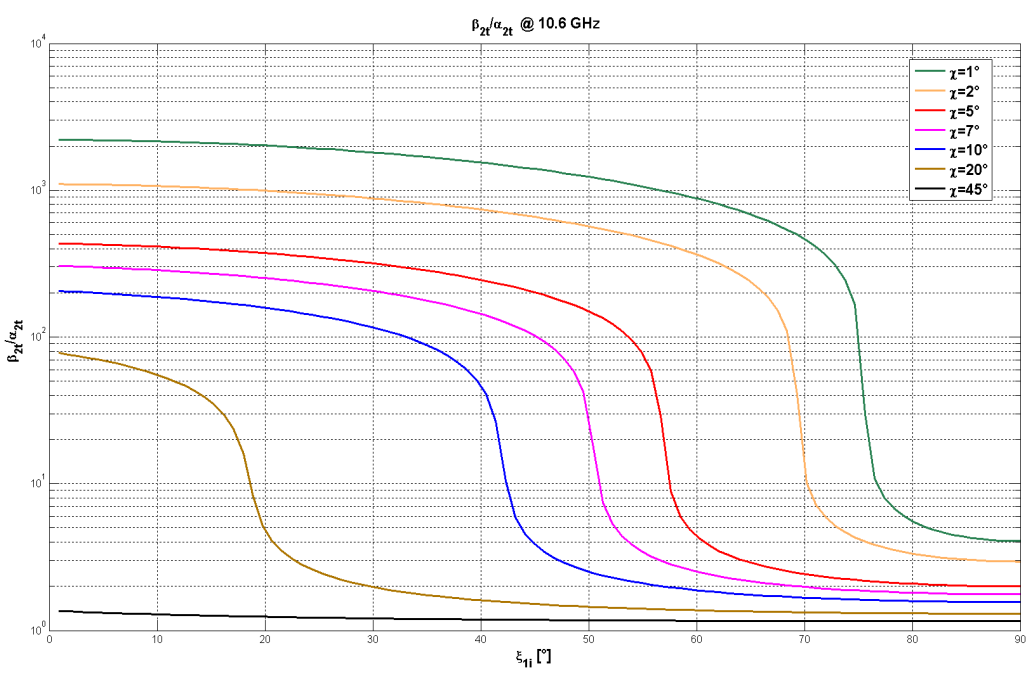

Figure 4-5: β_{2t}/α_{2t} **as a function of** ξ_{1i} **for some cases of** χ **for a FR4 prism**

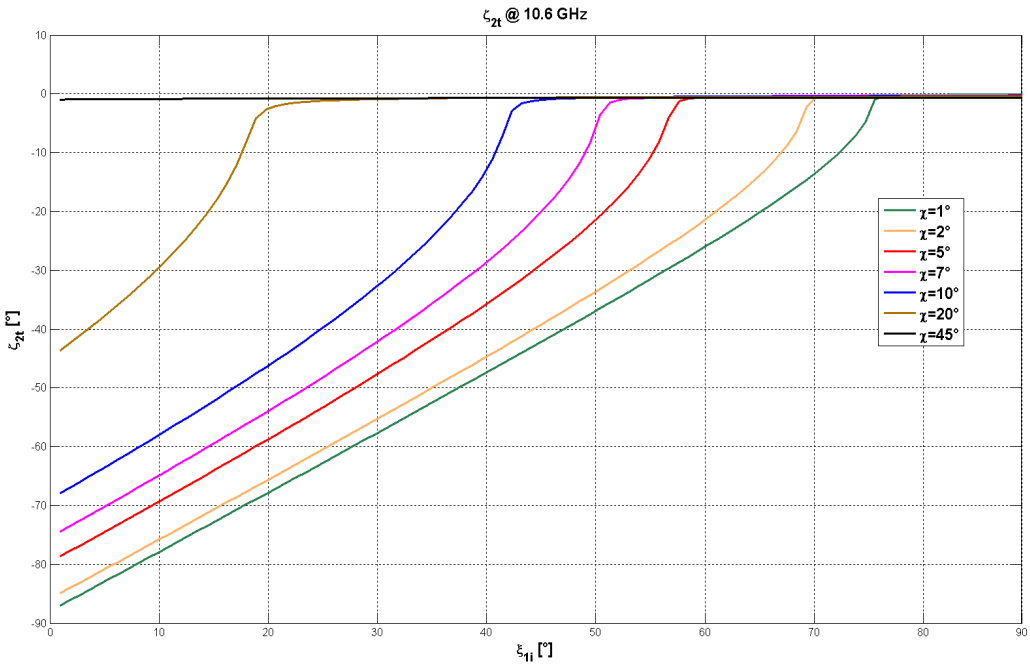

Figure 4-6: ζ_{2t} **as a function of** ξ_{1i} **for some cases of** χ **for a FR4 prism**

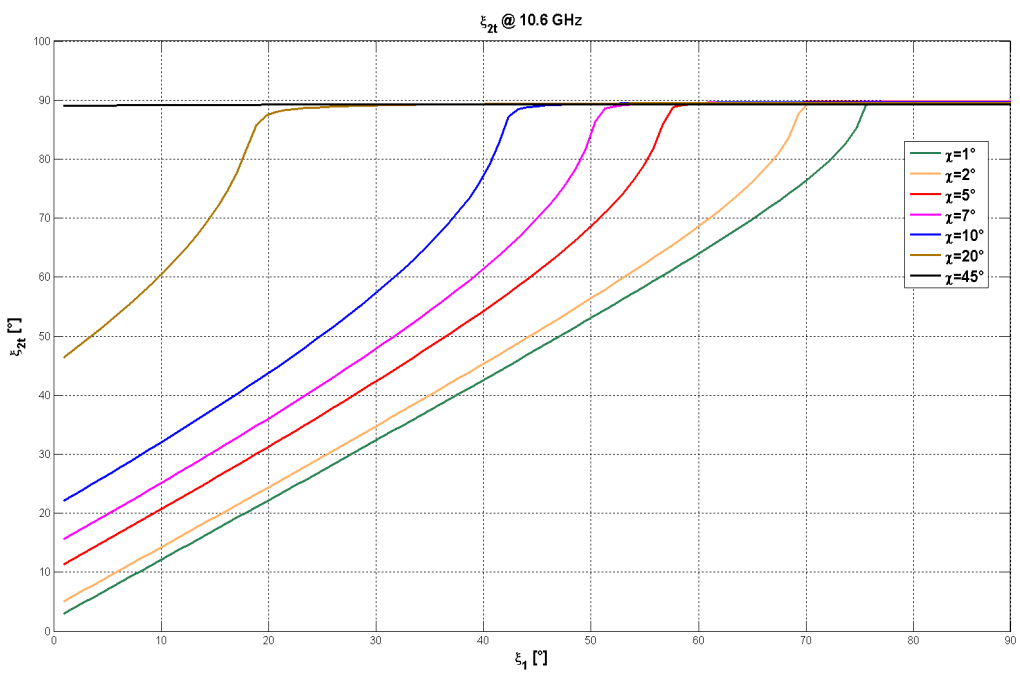

Figure 4-7: ξ_{2t} **as a function of** ξ_{1i} **for some cases of** χ **for a FR4 prism**

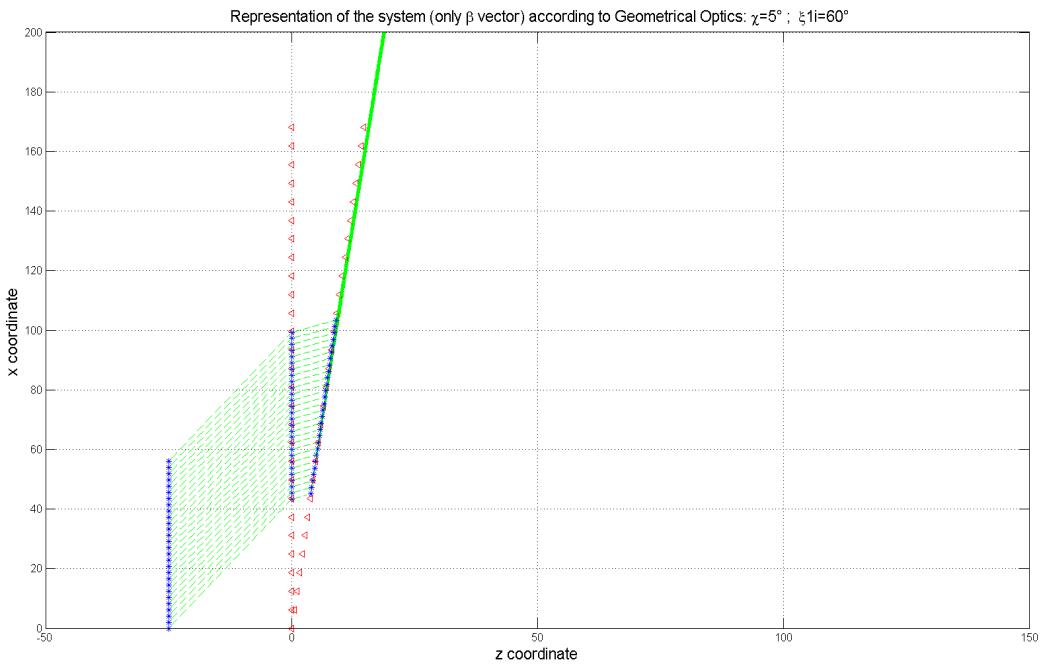

Figure 4-8: Ray tracing representation (β direction) of the *quasi-surface* wave generation condition

Figure 4-8 depicts the quasi surface wave condition assuming a pure geometrical-optics approximation of the system and confirms that the wave is not exactly parallel to the prism side, then it is not a bounded wave, but it is able to propagate in the free space.

Willing to choose the best working conditions, in order to penetrate a lossy material with the inhomogeneous wave generated by the dielectric prism, one may refer to the figures just presented. Figures 4-3 and 4-4 allow, first of all, to locate the region for the needed β_{2t}, which has to respect the condition (4.31), given the lossy material to penetrate. Secondarily, it has to be considered that the attenuation constant, although should respect the (4.31), shall be maintained as low as possible. In other words, the ideal condition would be to have the highest β_{2t} as possible maintaining α_{2t} as low as possible. Figure 4-5 aids in this regard giving the ratio β_{2t}/α_{2t}. Furthermore, the phase vector shall be as much as possible perpendicular to the prism oblique face (i.e. the attenuation vector shall be parallel to the face). Figures 4-6 and 4-7 indicate that this is possible for low ξ_{1i}. But, at the same time, low ξ_{1i} do not give high α_{2t} and β_{2t} (see again Figure 4-3 and 4-4), thus not ensuring for the fulfilment of the deep penetration condition for most of the lossy materials. This being true especially for small inclination angles of the triangular prism. In conclusion, the theoretical analysis, indicates that the optimal working settings which allow a general fulfilment of the deep penetration condition, retaining at the same time a compact system (i.e. small inclination angles of the triangular prism), correspond probably to lower part of the critical angle region (corresponding in general to by middle values of ξ_{1i}). For low values of ξ_{1i} the deep penetration condition in seldom achievable for lossy materials, while for large ξ_{1i} the generation of a *quasi-surface* waves occurs.

A good dimensioning for the system presented using a FR4 prism would be, for instance, with ξ_{1i}=53° and χ =5° (see Figure 4-9).

The MATLAB routine implemented is very handy in giving an immediate visual geometrical optics representation of the system. Please note that the hypothesis of a plane wave impinging the prism is here assumed.

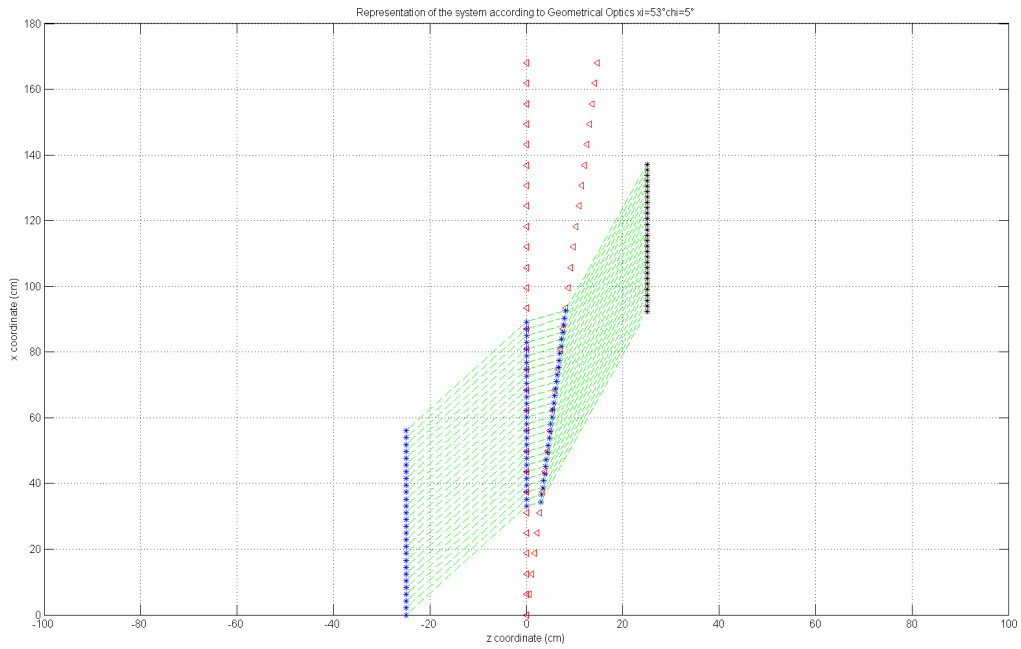

Figure 4-9: Ray tracing representation (β direction) for a 53° incidence with χ =5°

Ultimately, also the material of the prism is varied. Figures 4-10 to 4-15 complete the analysis showing the variation of the ratio β_{2t}/α_{2t} and the variation of the angle of the propagation vector after the prism (ξ_{2t}) depending on the relative permittivity and on the loss tangent of the prism, respectively, with a χ = 5°. It can be noted an increase and saturation of the ratio β_{2t}/α_{2t} when increasing ε'_r. A marked dependence of the critical angle on the ε'_r is highlighted. On the contrary, the increase of $tg\delta$ causes a decrease of the ratio β_{2t}/α_{2t} , while the critical-angle results in general not affected. At the same time, it is noted that the variation of the angle of propagation vector generated after the prism is strongly dependent on the ε'_r (Figure 4-14), while it is not for the $tg\delta$ up to the critical incident angle (defined by the prism material), which results also independent by the $tg\delta$. Beyond such angle, the ξ_{2t} saturates, to values close to 90°. Nevertheless, Figure 4-15 shows that higher values of $tg\delta$, thus of $\sigma = 18$, allow to avoid the generation of a *quasi-surface* wave. This property is of high remark and will be exploited later in the application to real materials to be penetrated.

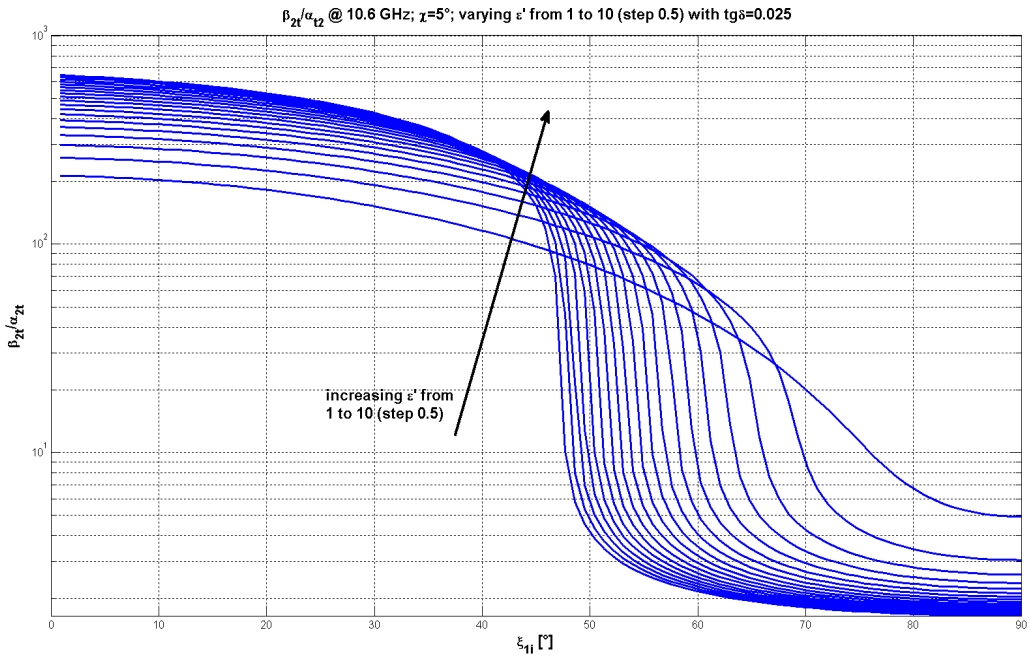

Figure 4-10: β_{2t}/α_{2t} **as a function of** ξ_{1i} **and** ε'_r

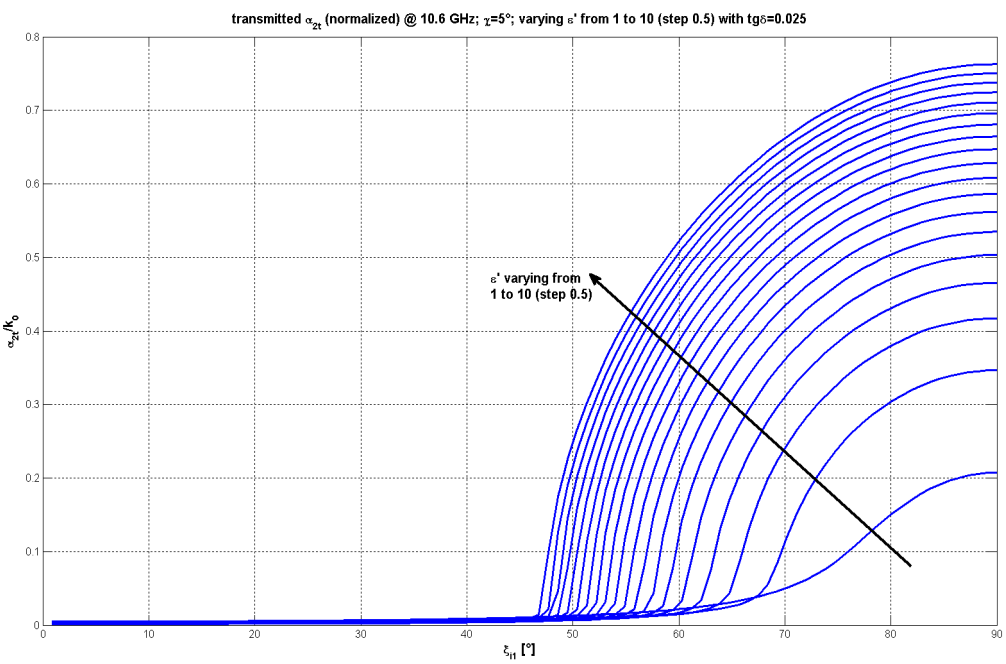

Figure 4-11: α_{2t} **as a function of** ξ_{1i} **and** ε'_r

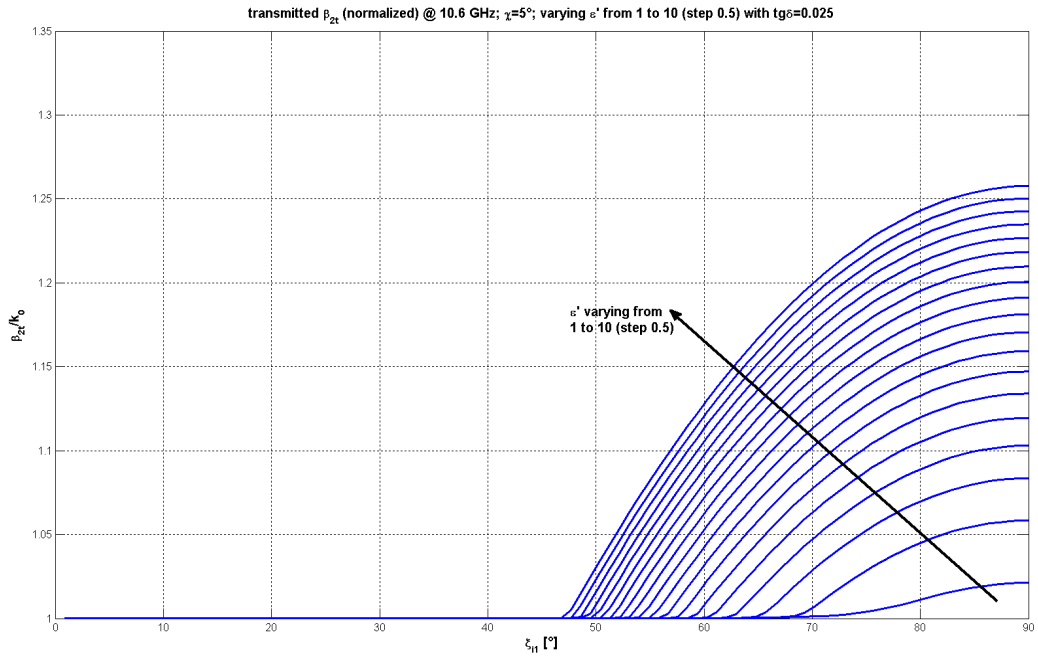

Figure 4-12: β_{2t} **as a function of** ξ_{1i} **and** ε'_r

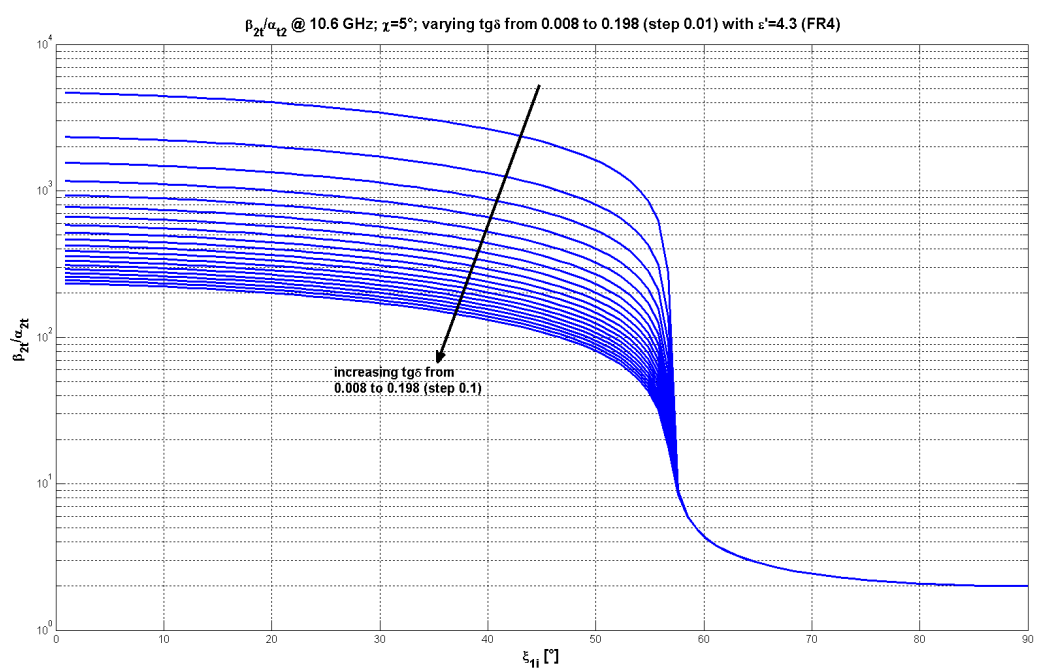

Figure 4-13: β_{2t}/α_{2t} **as a function of** ξ_{1i} **and** $tg\delta$

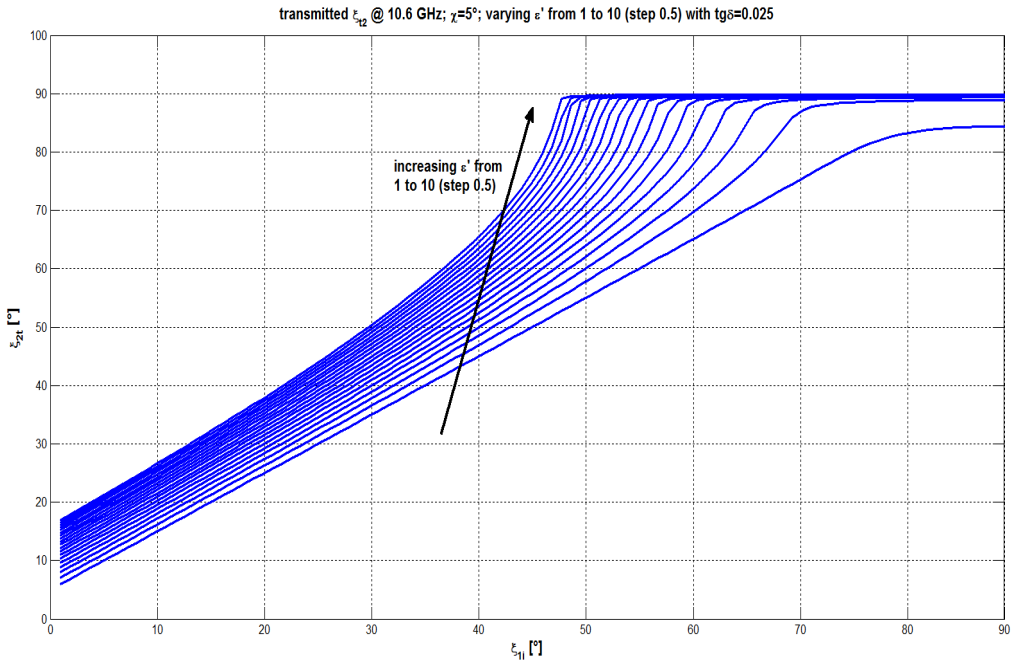

Figure 4-14: ξ_{2t} **as a function of** ξ_{1i} **and** ε'_r

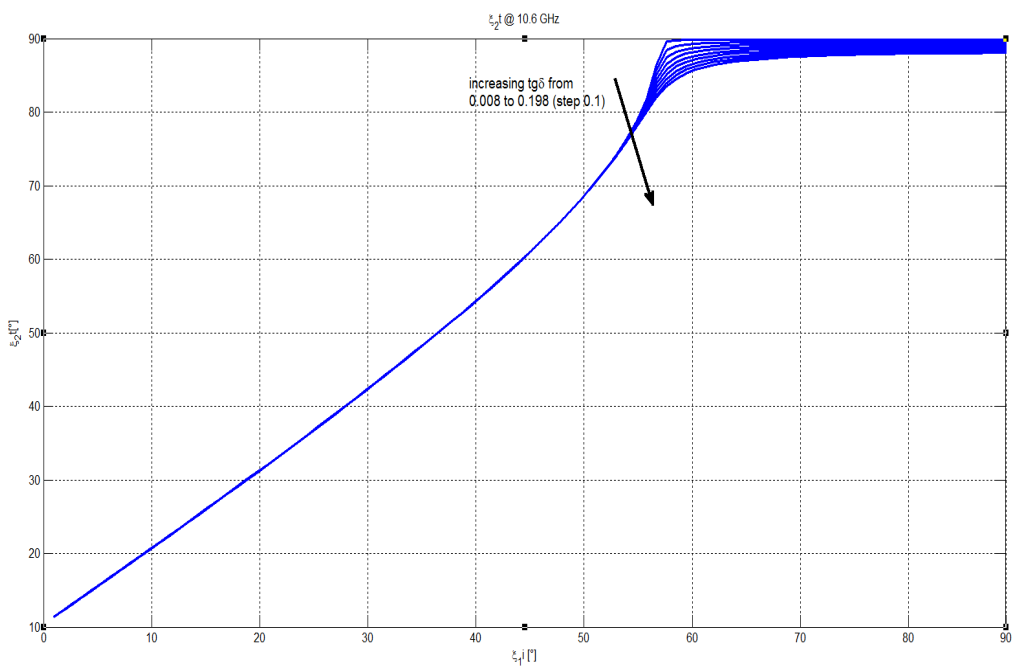

Figure 4-15: ξ_{2t} **as a function of** ξ_{1i} **and** $tg\delta$

4.6 The electromagnetic model

A rectangular tapered (WR90) horn antenna working at 10.6 GHz was considered using the commercial electromagnetic software Microwave Studio from CST. The horn is placed at a distance from the prism, Lm, which allows to consider the radiated beam as a finite-section quasi-plane wave at the prism interface. A prism with squared transverse section, $\chi = 5°$ and made of FR4 material is considered. The vertical side is 556.9 mm long, computed as the horn HPBW footprint at a distance Lm plus a margin evaluated as FFd/2, being FFd the far field distance of the horn antenna, equal to 1013 mm at the working frequency.

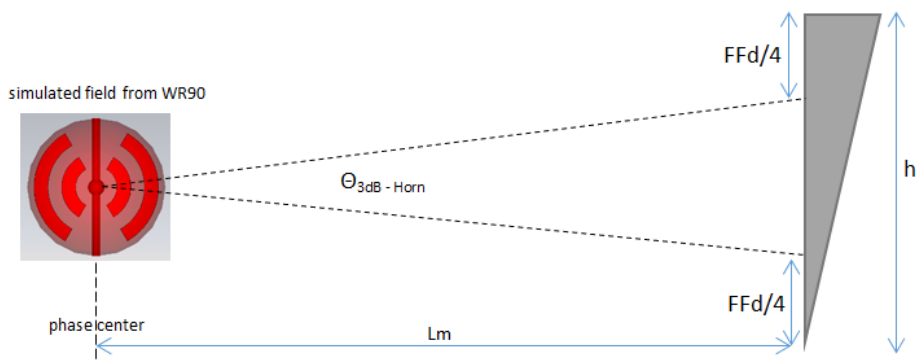

Figure 4-16: A sketch of the radiated field illuminating the prism. The figure is not in scale for the dimensions used in the CST model used (Lm = 152 mm, h = 556.9 mm, ϑ _3dB = 14.3 deg, FFd = 101.2 mm)

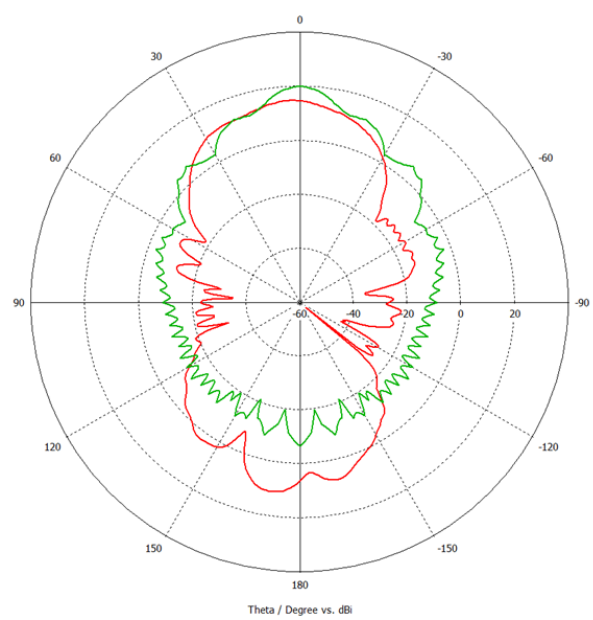

Figure 4-17: CST pattern single tapered horn (green) and system horn+prism (red)

The radiation patterns depicted in Figure 4-17, green-lined for the single horn, red-lined for the system, show the impact of the dielectric prism on the radiating characteristics of the source used for the boresight case. As expected, the dielectric prism substantially impacts on the radiating performances. In Table 4-5, the cases of interest, where the impinging angle ξ_{1i} is non-null, are added. Figures 4-16 and 4-17 show the electric field propagating in the y-z plane for the single horn and the system with ξ_{1i} = 5°, respectively.

Table 4-5: Radiation characteristics of the single horn compared to the system horn+prism for various cases of incidence

Target	**Single Horn**	**Horn+prism (ξ_{1i} 0°)**	**Horn+prism (ξ_{1i} 5°)**	**Horn+prism (ξ_{1i} 45°)**	**Horn+prism (ξ_{1i} 65°)**
Main lobe magnitude	20.1 dB	14.8 dB	14.4 dB	15.2 dB	17.3 dB
Main lobe direction (with respect to the perpendicular to the second prism interface)	0.0° (with respect to boresight)	3°	6°	57°	88°
HPBW	14.3°	29.2°	37.8°	31.1°	5.6°

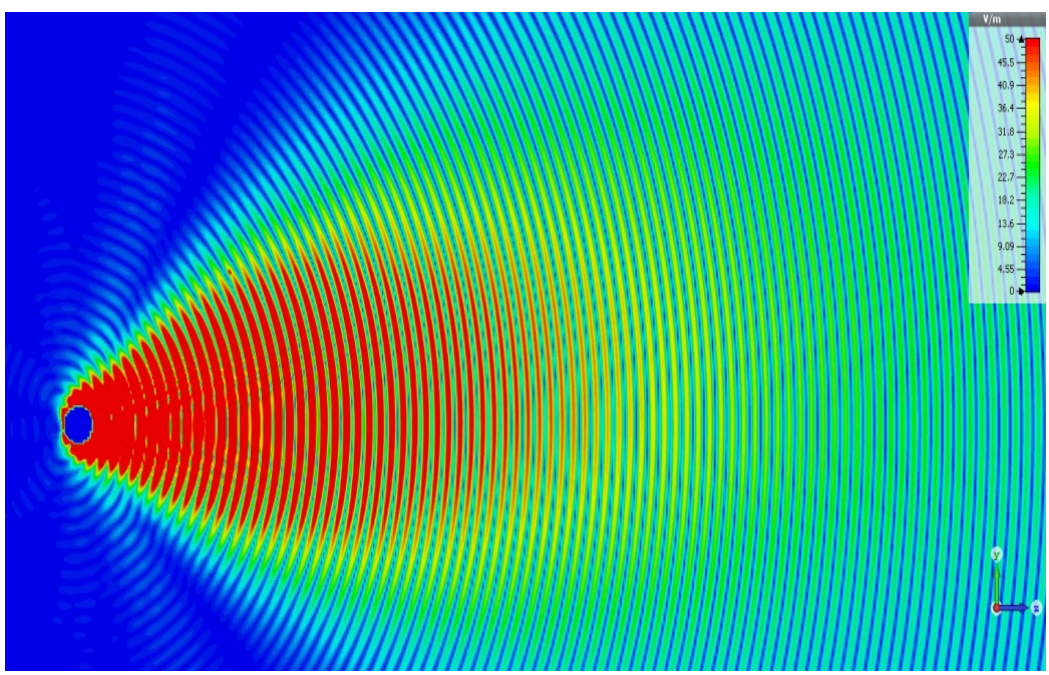

Figure 4-18: Full wave simulated electric field (including phase) along the propagation y-z plane of the single tapered horn modeled for angle ξ_{1i} = 5° with respect to the z-axis

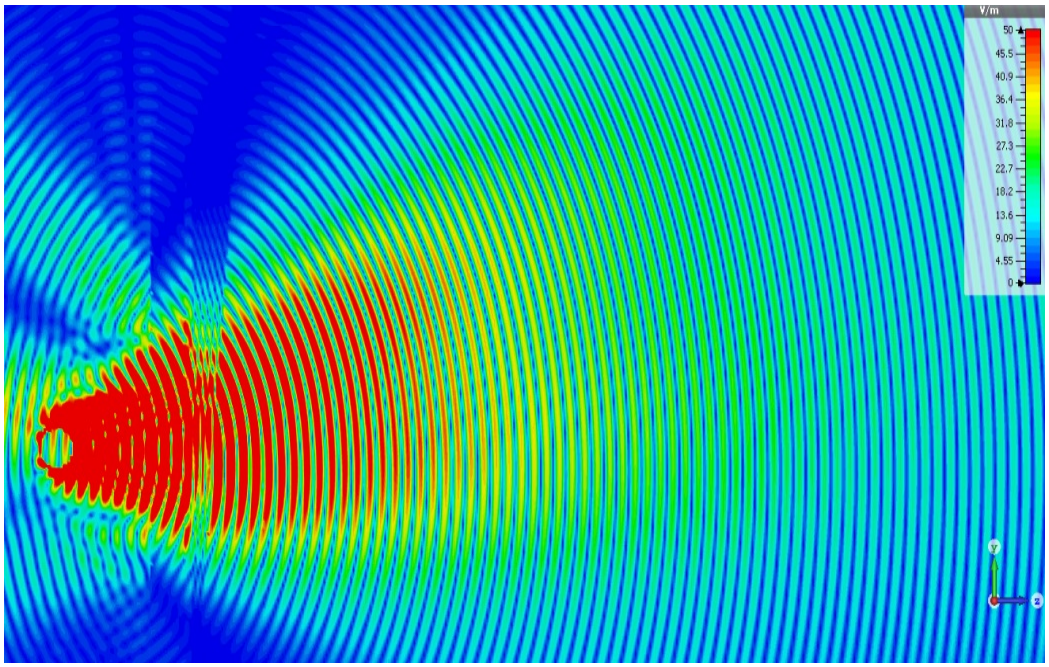

Figure 4-19: Full wave simulated electric field (including phase) along the propagation y-z plane with dielectric FR4 prism and incidence ξ_{1i} = 5° with respect to the z-axis

The directions of the main beam simulated with the CST software are substantially in accordance with the direction of the β_{2t} derived by the theoretical model with the MATLAB, although one may spot some difference which can be justified if multiple reflections are considered within the prism.

It can be also noted that the case reported in the last column of Table 4-5 corresponds to the *quasi-surface* wave condition already discussed and shown in Figure 4-8 as a result of the theoretical computation of the directions of the β.

Using the CST full wave simulations, a validation of the MATLAB theoretical model has been performed. Several cases were computed and the directions of the phase vector were evaluated and compared to the ones obtained theoretically in Figure 4-7. Figure 4-20 presents a very good agreement between the MATLAB model and the CST simulations.

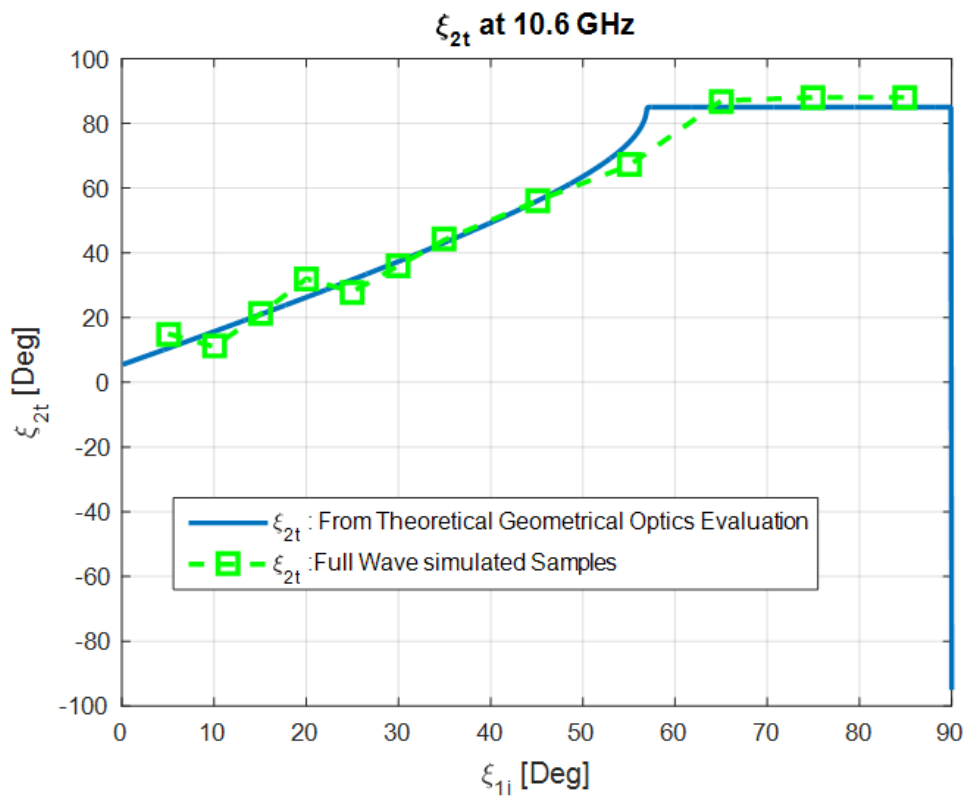

Figure 4-20: Validation of the full wave electromagnetic model with the MATLAB theoretical model. Comparison of the phase vector directions at the prism's output.

4.7 Numerical practical cases for the deep penetration

Having generated an inhomogeneous wave, which characteristics can be controlled according to the analyses presented in the previous paragraphs, the application of such wave to a lossy material can be studied in order to seek for the deep penetration condition, afore introduced and demonstrated. This process has to start from the consideration of the lossy material to penetrate.

Considering an impinging inhomogeneous wave travelling in the air, the $\beta_{\min}$ allowing the existence of a critical angle for the deep penetration through the chosen material, can be derived from (4.31). In (4.31) the subscript 1 refers in this case to the air and the subscript 2 refers to the lossy material to penetrate.

Let us refer to the water in three forms: polar ice cap, fresh water and sea water.

Considering the parameters which can be controlled for the prism's system (χ, ξ_{1i}, ε'_r and σ), an optimization algorithm was built with the goal (in order of relevance) to:

1) have a β_{t2} generated after the prism larger than the $\beta_{\min}$ required for the DPW for the selected material to penetrate

2) be far enough from the quasi superficial wave condition: the direction of the propagation vector after the prism shall not be very close to the prism inclined face. A minimum angle of separation of 15° was considered

3) have an angle of DPW with respect to the material to penetrate which allows to place the material in an affordable position with respect to the prism (even slightly rotated), considering the DPW angle obtained with the material chosen and as a result of points 1) and 2)

4) have small inclination angle for the prism so to minimise any loss introduced by the prism itself on the transmitted power

5) have a large ratio β_{2t}/α_{2t} for the amplitudes of the vectors of the wave generated by the prism.

4.7.1 The polar ice cap

The numerical routine obtained has been first applied to the case of the polar ice. In particular, the polar ice cap presents, at 10.6 GHz, ε'_r=1 and σ=0.0001 S/m. Since the value of the conductivity is very low, a further simplification can be added, consisting in retaining a FR4 prism and optimizing only for the incidence angle and the prism inclination angle. The algorithm shows that low values for the incidence angle and the inclination angle can be chosen as they are sufficient to achieve easily the DPW condition (condition 1), being $\beta_{\min}$ very small since the conductivity is very small too. Condition 2 and 3 are verified quite easily and therefore the maximisation of the ratio β_{2t}/α_{2t} can be pursued, retaining a small inclination angle for the prism available (condition 4). According to what shown in Figure 4-5, such maximization takes place indeed for small angles of incidence and small inclination angles of the prism.

Table 4-6 summarizes the output optimized parameters for the penetration of the polar ice cap at 10.6 GHz considering a FR4 prism, as done so far.

Table 4-6: Optimised input parameters for the DPW of the polar ice cap considering a FR4 prism

Parameter	Value	Unit
ξ_{1i}	5	deg
χ	5	deg
material of the prism	FR4	

Considering the parameters in Table 4-6, the system is characterised as follows:

Table 4-7: The DPW system output parameters for the polar ice cap considering the inputs of Table 4-6

β_{2t} / k_0	1.001	m^{-1}
$\beta_{\min}$ DWP$/ k_0$	1	m^{-1}
β_{2t} / α_{2t}	251	m^{-1}
$\xi_{2t_to_boresight_direction}$	10.5	deg
$\xi_{DWP_to_boresight_direction}$	1.22	deg

As indicated by Table 4-7, the direction of the propagation vector of the prism has to be 1.22° with respect to the material to penetrate (which interface is assumed perpendicular to the boresight direction) so to fulfill the condition (4.30). The results indicate that the propagation vector is inclined 10.5° for the present study case with respect to the boresight direction; it means that the relative inclination of the prism with respect to the material to penetrate has to be 9.28°, as shown in the schematic of Figure 4-21.

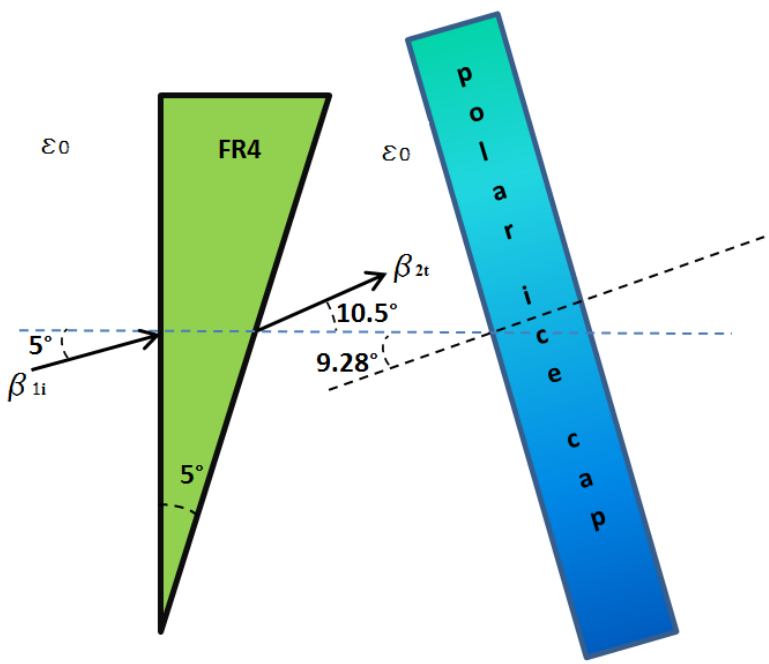

Figure 4-21: Schematic of the DPW system for the polar ice cap using a FR4 prism.

4.7.2 The fresh water

If one now considers the fresh water at 10.6 GHz and at 20°C, the ε'_r is found to be 80 and the conductivity σ equals 0.01 S/m. Table 4-8 shows the optimised input parameters obtained accordingly to the algorithm.

Table 4-8: Optimised input parameters for the DPW of the fresh water considering a FR4 prism

Parameter	Value	Unit
ξ_{1i}	46	deg
χ	7	deg
material of the prism	FR4	

Again, a FR4 prism could be retained, with the price of having higher ξ_{1i} and χ. It is noted, in fact, that the threshold for the DPW starts to increase because of a higher σ ($\beta_{\min}$ is only dependent on the imaginary part of the k of the material to be penetrated; see again 4.31). Consequently, the algorithm raises the ξ_{1i} until condition 2 is respected (see Figure 4-7 for reference) and then it raises the χ as soon as the ξ_{1i} cannot be increased further to avoid the quasi-surface wave condition. In this particular case, the final optimized configuration allows the system to work at the beginning of the transition region individuated in Figure 4-5.

Considering the parameters in Table 4-8, the system described results as follows:

Table 4-9: The DPW system output parameters for the fresh water considering the inputs of Table 4-8

β_{2t}/k_0	1.0002	m^{-1}
$\beta_{\min}$ DWP$/k_0$	1.0001	m^{-1}
β_{2t}/α_{2t}	54.2109	m^{-1}
$\xi_{2t_\text{to}_boresight_direction}$	64	deg
$\xi_{DWP_to_boresight_direction}$	33.3884	deg

4.7.3 The sea water

The case of the sea water, which presents, at 20°C and 10.6 GHz, ε'_r=48 and σ=4 S/m is of great interest in the context of this argument and, in general, of the subject presented in the present chapter for two reasons. Primarily, the sea water can be fairly considered one of the best examples of imperfect dielectric, having a non-negligible value for its conductivity. Secondarily, such value of conductivity sets a threshold for the $\beta_{\min}$ which allows the DPW to a value almost three times greater than for very small conductivities, as the ones analysed before.

Bearing in mind that this part of the study has the purpose to analyse the problem only on a theoretical level, the algorithm implemented according to the rules numbered above, shows that there is no possibility of employing the FR4 as a material for the prism as it cannot allow to respect all the conditions imposed. Therefore, the characteristics of the prism have to be varied and included in the optimisation algorithm. The outcome of the algorithm leads to the input parameters listed in Table 4-10.

Table 4-10: Optimised input parameters for of the sea water which allows the DPW condition

Parameter	Value	Unit
ξ_{1i}	51	deg
χ	15	deg
material of the prism	$(\varepsilon'_r = 50\ ;\ \sigma = 18)$	

Such dimensioning determines the characteristics listed below in Table 4-11.

Table 4-11: The DPW system output parameters for the sea water considering the inputs of Table 4-10

β_{2t} / k_0	2.7106	m^{-1}
$\beta_{\min}\ \mathrm{DWP} / k_0$	2.7021	m^{-1}
β_{2t} / α_{2t}	1.0759	m^{-1}
$\xi_{2t_\mathrm{to}_boresight_direction}$	62.64	Deg
$\xi_{DWP_to_boresight_direction}$	41.6767	Deg

It is evident that the thick prism obtained (15° of inclination angle), presenting such relevant conductivity of $\sigma = 18$ is clearly a result which is not acceptable. In fact, the prism itself would be not electromagnetic penetrable at all.

Unfortunately, the higher is the σ of the material to penetrate, the more the values of the input parameters have to be increase to fulfil the conditions imposed. A workaround would be to remove condition 2. In other words, to accept that the generated wave after the prism is a *quasi-surface* wave. This helps, primarily, in lowering the affordable conductivity of the prism. Secondarily, having removed condition 2, the inclination angle can be substantially reduced if one raises the value of the real part of the permittivity of the prism. A numerical example is given in Table 4-12 and Table 4-13.

Table 4-12: Optimised input parameters for the sea water removing condition 2

Parameter	Value	Unit
ξ_{1i}	49	Deg
χ	7	Deg
material of the prism	$(\varepsilon'_r = 280\ ;\ \sigma = 0.1)$	

Table 4-13: The DPW system output parameters for the sea water considering the inputs of Table 4-12

β_{2t} / k_0	2.7044	m^{-1}
$\beta_{\min}$ DWP$/ k_0$	2.7021	m^{-1}
β_{2t} / α_{2t}	1.0763	m^{-1}
$\xi_{2t_\text{to}_boresight_direction}$	**82.98 (*quasi-surface* wave)**	Deg
$\xi_{DWP_to_boresight_direction}$	43.2597	Deg

This last numerical case represents a proof of the general conclusion given by the present study that for materials which are substantially imperfect dielectrics (i.e. with a conductivity equal or higher than circa 0.5 S/m) the DPW condition of the inhomogeneous wave generated can be achieved only if the wave becomes a *quasi-surface* wave.

4.8 Conclusion

The ability of inhomogeneous wave of acting as deep penetrating waves is demonstrated at first in this chapter and the related conditions to be fulfilled are presented.

A novel approach for inhomogeneous waves generation in lossless media based on the illumination of a dissipative triangular prism by a homogeneous wave is then presented. It is demonstrated that the system designed is able to generated an inhomogeneous wave from a homogenous wave under general conditions.

The behaviour of the transmitted attenuation and phase vectors is fully characterised. The analyses shows a dual behaviour defined by a so defined critical incident angle, which is determined by the prism properties. In particular, it is primarily dependant on the angle of inclination of the prism and secondarily on its relative permittivity, while independent on the loss tangent of the material. Below such incident angle, the inhomogeneous wave which emerges from the prism is not a surface wave, while beyond it behaves as a *quasi-surface* wave. The magnitudes and the angles of this inhomogeneous wave can be tuned by the choice of the prism's geometry (angle of inclination) and material. The direction of the propagation vector of the so generated inhomogeneous wave is characterised as well, finding a stronger dependence with the real part of the relative permittivity rather than with the conductivity of the prism.

Electromagnetic simulations with a rectangular tapered horn antenna illuminating a lossy prism of FR4 material were considered too and demonstrated a full correspondence with the theory as far as the propagation vectors are concerned.

Finally, numerical cases were considered with the purpose of attaining the deep penetration through the water in three different forms, respectively the polar ice cap, the fresh water and the sea water. All analyses presented in this chapter referred mainly to a frequency of operation of 10.6 GHz, aiming at reducing the dimensions for the prism and, ultimately, at investigating the viability of generating an inhomogeneous wave for the deep penetration through lossy media at such frequencies, as never done before in the literature. In this context, an optimisation algorithm was built with the goal of having a system capable of achieving the deep penetrating wave condition for a system including a prism which is not introducing substantial losses to the transmitted wave. It is found that this requirement is achievable considering imperfect dielectrics with a conductivity less or equal than circa 0.5 S/m. For higher values, the exploitation of *quasi-surface* inhomogeneous wave has to be considered.

The numerical cases presented indicate a way forward to prove the deep penetration concept analysed in this work through experimental tests. In this sense the use of a FR4 prism in the previous analyses permits an easy set up for carrying out such tests for a material to penetrate which presents low conductivity, as the ice cap or the fresh water. The FR4 is in fact a common cheap material, suitable for laboratory empirical tests.

More accurate considerations have to be drawn when referring to materials to penetrate which present a conductivity equal or greater than values close to 0.5 S/m. The present work demonstrated that in this condition, the generation of a *quasi-surface* inhomogeneous wave is required to achieve the deep penetration. The exploitation of such wave into a real applicative system is a matter of evaluation for future developments of the current research. First of all, if the losses in directivity introduced by

squeezing the radiation generated by an aperture into a *quasi-surface* wave a can be considered in any case acceptable.

References

[4-1] Constantine A. Balanis, Advanced Engineering Electromagnetics , Wiley, solution manual edition, May 1989.

[4-2] E. O. Schulz-DuBois, Energy transport velocity of electromagnetic propagation in dispersive media, Proceedings of the IEEE, Vol. 57, Issue 10, 1748 – 1757, Oct. 1969.

[4-3] Li Gao, Computing the plane electromagnetic wave transient propagation in lossy medium based on COMSOL Estimation, Detection and Information Fusion (ICEDIF), 2015 International Conference on 367 – 371 10-11, Jan. 2015.

[4-4] L. L. Li., Deeper-penetrating wave applicator in non-invasive hyperthermia, 549 - 552 vol.18-10 Microwave Symposium Digest, 1990., IEEE MTT-S International, May 1990.

[4-5] N. Tedeschi and F. Frezza, An analysis of the inhomogeneous wave interaction with plane interfaces, in *Proc. URSI GASS'14*, paper BP1.25, p. 109, 2014.

[4-6] J.A. Stratton, *Electromagnetic Theory*, McGraw-Hill, New York, 1941.

[4-7] J.E. Roy, "New results for the effective propagation constants of nonuniform plane waves at the planar interface of two lossy media," *IEEE Trans. Antennas Propag.*, vol. 51, pp. 1206-1215, 2003.

[4-8] F. Frezza and N. Tedeschi, "Deeply penetrating waves in lossy media" *Opt. Lett.* vol. 37, pp. 2616-2618, 2012.

[4-9] F. Frezza and N. Tedeschi, "On the electromagnetic power transmission between two lossy media: discussion," *J. Opt. Soc. Am. A*, vol. 29, pp. 2281-2288, 2012.

Chapter 5

CONCLUSIONS

This thesis has presented a virtual tour of technological and design solutions for antenna systems. Several theoretical and empirical approaches have been used, aided by simulations models to render the introduced antennas respectively light, small, simple, powerful (in terms of available gain), versatile, sustainable and deep penetrating, as needed by the proposed application. Spaceborne antennas, ground based antennas and deep penetrating antenna actuators have been introduced and characterized.

The present paragraph is intended to summarise the main conclusions and considerations drawn in the various analyses presented in this dissertation. Furthermore, it gives a glimpse on the future perspective for a further development of the concepts and techniques matured in the present work.

After the general introduction in Chapter 1 on antenna basics, parameters and fields of application, it has been shown in Chapter 2 how the complexity, weight and encumbrance of antenna satellite payloads may be reduced by employing advanced imaging hybrid solutions. In particular, the scanning properties of dual reflector antenna systems constituted by two confocal paraboloidal reflectors fed by a planar array have been investigated. Heuristic equations, representing an extension of the linear equations available in the literature, have been derived which permit predicting the system's pointing direction as a function of the pointing direction of the feeding array in a significant field of view. The relations obtained allow to adopt array excitations techniques to compensate the distortions, i.e. the aberrations, produced by the imaging hybrid system and to have a *quasi-aberration* free system, which is equivalent to a larger, heavier and definitely more complex arrangement. The resolution of the aberrations impact may lead to further developments for such configuration, as for example the employment of interferometric feeding arrays. Interferometric aperture synthesis was suggested in the 1980s as an alternative to real aperture radiometry for Earth observation. An interferometric approach is currently being developed for telecommunications too. The concept of array aperture synthesis relying on interferometry consists on single signals measured by each receiving elements of the antenna array get mixed (or cross-correlated) to produce a narrower pencil beam (finer coverage) with respect to what possible considering a single array aperture.

In Chapter 3, an extensive panoramic on ground based antenna has been shown. Aspects connected to the antenna mounting and satellite tracking were introduced, focusing afterwards on the optimization of the elements related to the antenna efficiency, with the purpose of achieving the maximum available gain, essential for the support of deep space missions. The case of the upgrade of a large radio telescope into a TT&C deep space antenna was studied in detail, addressing to design techniques involving an electromagnetic representation through Gaussian

beams. The versatility of the design proposed for the Sardinia Radio Telescope (SRT) allowed to allocate different operational bands and to cope with the beam squint problem, which may become a source of non-negligible losses for the support of very far deep space probes having a considerable transverse velocity component. The high gain which characterises SRT, with its 64-m of diameter and foreseen transmitted power up to 5 kW, together with its versatility, provided to operate both for radio astronomy and TT&C, raised important sustainability issues. EMC, EMI and biological hazards analyses were therefore performed in order to assess and prevent any potential issue with respect to the station equipment and to the surrounding environment, including overflying aircrafts. When necessary, engineering countermeasures were proposed.

SRT belongs to the class of TT&C antenna with largest aperture, comparable to the JPL 70-m terminals. In recent years, however, we are experiencing an inversion in the tendency to increase the size of ground station antennas, towards solutions considering arrays of ground terminals. This would produce many benefits in terms of costs and link performance. As an example smaller dishes are less sensitive to mechanical deformations and therefore may operate at lower wavelengths; single-point failures are avoided, thus dramatically improving the reliability of the system; and sub-arrays may allow for multiple concurrent links. Deep Space arraying is the direction towards which the main international space agencies are looking forward, together with space communications in the optical domain.

In chapter 4, recent results are present for the generation of inhomogeneous waves in lossless media based on the illumination of a dissipative triangular prism by a homogeneous wave. It is demonstrated that the system designed is able to generated an inhomogeneous wave from a homogenous wave under general conditions and to achieve the deep penetration of lossy media.
Some example cases were considered for the penetration of the polar ice cap, the fresh water and the sea water, respectively. It is found that imperfect dielectrics with a significant conductivity as the sea water require the generation of a *quasi-surface* inhomogeneous wave in order to allow for the deep penetration. The exploitation of such wave into a real applicative system is a matter of evaluation for future developments of the current research. Some solutions like modifying the shape of the prism may aid but they are still under investigation.

The use of the FR4 as a material for the prism, indicated, on the other side, the viability for carrying out empirical tests for studying the penetration in imperfect dielectrics with much smaller conductivity, as the ice cap or the fresh water.

Eventually, since the present study pointed to the importance of the selection of the prism material in order to modify the characteristics of the inhomogeneous wave and its capability of penetrating lossy materials, the employment of *metamaterials* for the prism has to be taken in high consideration. *Metamaterials* would allow to produce a prism with specific properties so to give exactly the desired permittivity and conductivity.

PERSONAL BIBLIOGRAPHY

International Journals and Volumes

[J-1] F.Pelorossi, G.Toso, P. Angeletti, On the scanning properties of imaging antennas based on dual confocal paraboloidal reflectors, *Progress In Electromagnetics Research M,* Vol. 37, pp. 95-107, 2014.

[J-2] A.Giannini, F.Pelorossi, M.Pasian, M.Bozzi, L.Perregrini, P.Besso and L.Garramone, The Sardinia Radio Telescope Upgrade to Telemetry, Tracking and Command: Beam Squint and Electromagnetic Compatibility Design, *IEEE Antennas and Propagation Magazine,* Vol. 57, No. 1, pp. 177-191, February 2015.

International Conferences

[C-1] F.Pelorossi, B.Tsonevska, G.Toso, P.Angeletti and F.Frezza, On the Scanning Properties of a Confocal Dual Reflector Antenna System, IEEE International Symposium on Antennas and Propagation and USNC-URSI National Radio Science Meeting, Chicago, 08/07/2012.

[C-2] G.Billig, R.Launer, F.Pelorossi, Launcher Tracking Support from ESTRACK, Ground-based Space Facilities Symposium, Paris, 12/06/2013.

[C-3] F. Pelorossi, A. Giannini, M. Pasian, M. Bozzi, L. Perregrini, L. Garramone and P. Besso, TT&C Upgrade of Sardinia Radio Telescope - BWG Optical Design Solutions and EMC with the Radio-Astronomy Receivers, TT&C 2013 Workshop, ESA ESOC, Darmstadt, 09/09/2013.

[C-4] F.Pelorossi, P.Besso and L.Garramone, Electromagnetic compatibility and interference practical analyses for beam waveguide ground antennas, IEEE International Symposium on Electromagnetic Compatibility, Ottawa, 25/07/2016.

[C-5] N. Tedeschi, V. Pascale, F. Pelorossi and F. Frezza, Generation of inhomogeneous electromagnetic waves by a lossy prism, International Symposium on Electromagnetic Theory (EMTS 2016), Espoo (Finland), 14/08/2016.

[C-6] V. Pascale, F. Pelorossi, N. Tedeschi and F. Frezza, Inhomogeneous waves generation for the electromagnetic deep penetration into lossy media, XXI Riunione Nazionale di Elettromagnetismo (RINEM), Parma (Italy), 12/09/2016.